이학박사 학위논문

SERS study of highly efficient vibrational pumping of adsorbate molecules induced by gap−plasmons

표면증강라만분광법을 사용한 간극 플라스몬 내
흡착분자의 고효율 진동모드 펌핑 연구

지도교수 : 김지환

2020 년 8 월

서울대학교 대학원
화학부 물리화학전공

신현항

Abstract

Highly efficient vibrational pumping mechanisms of adsorbate molecule are studied using surface-enhanced Raman scattering (SERS). The irradiation of light induces collective oscillation of conductive electrons in nanostructure which is called localized surface plasmon (LSP) and it enhances EM field near the metal nanoparticles. The field enhancement which is maximized at gap junction not only boost Raman scattering (SERS) but also pump vibrational mode of molecules in proximity. In this thesis, two vibrational pumping mechanisms are focused. One is the super strong field enhancement generated near the sub-structures of metallic surfaces which is called "picocavities" and the other is resonant inelastic scattering of energetic electrons induced by LSP. These efficient pumping processes generate vibrationally excited population in steady state overcoming fast vibrational relaxation on metallic surfaces.

Even though the origin of picocavity is unclear, it is suspected that gap-plasmon stochastically excite fine structure on metallic surfaces such as atomic protrusions. Highly localized EM fields near the picocavities generates (1) super strong field-gradient altering Raman selection rule of nearby molecules and (2) additional boost of SERS. The additional boost of SERS pumps picocavity SERS active

vibrational modes and it result in emergence of intense peaks on both Stokes and anti-Stokes side. In this thesis, the existence of picocavity are proved by analyzing the shape of SERS spectra. Anti-Stokes and Stokes SERS of 4,4-biphenyldithiol (BPDT) molecules sandwiched between silver nanoparticle (AgNP, diameter of 80 nm) and gold thin film (AuTF, thickness of 10 nm) are simultaneously obtained. Many spectra exhibit the features of picocavity SERS spectra. Unlike to prior report, furthermore, many of the spectra exhibit only one prominent peaks on both anti-Stokes and Stokes side. To reproduce experimentally obtained SERS spectra, Raman-activities of vibrational modes of BPDT are re-evaluated by picocavity model calculation. In this model, the EM field set to stretch out from the center of picocavity and decay with gaussian function. By the model calculation, the specific positions of picocavities which reproduce specific spectra can be decided and many experimentally obtained picocavity spectra are successfully reproduced. The calculation also reveals that the lower boundary of picocavity size (diameter) should be 3.5 Å to reproduce single SERS peak spectra and the size may be large as 1 nm to reproduce the multiple peak picocavity SERS spectra. All of these results strongly support the possibility of the existence of picocavity. Moreover, many single peak picocavity SERS spectra strongly suggest the possibility of mode

selective vibrational pumping which may control surface chemical reactions. For conventional plasmonic gap structures (i. e. nano particle dimers or nanoparticle-thin film junctions), however, the formation and the position of picocavity cannot be controlled yet.

Similar to resonant Raman scattering, molecules receive the energy from electrons whose energy is accessible to empty orbitals through inelastic scattering. The received energies are accumulated to specific vibrational modes whose Franck-Condon factors are favorable. In this thesis, electron mediated vibrational pumping on metallic surface is shown. Stokes and anti-Stokes SERS of 4-nitrobenzenethiol (NBT) sandwiched between AgNP and AuTF are simultaneously observed. NBT undergoes photo-reduction at the gap-plasmonic junction under light illumination. At the beginning of the photo-reduction, intense anti-Stokes peak of ν_S(NO) which is localized to functional group emerges. Meanwhile, the other peaks do not show such feature. Similar to picocavity SERS, the anti-Stokes of ν_S(NO) show quadratic power dependence which implies that the ν_S(NO) is nonthermally pumped. Unlike to picocavity SERS, however, the activation of ν_S(NO) does not show (1) randomly blinking feature and (2) Raman selection rule alteration. Above all, (3) anti-Stokes of NBT shows high mode selectivity and reproducibility. To account for this pumping process, resonant inelastic electron scattering model

which is governed by Franck–Condon integral of each vibrational mode is modelled. The model calculation successfully reproduced ν_S(NO) selective scattering efficiency. To confirm ν_S(NO) pumping is related to plasmon, anti–Stokes of ν_S(NO) is obtained with 488, 532, 633, 808 nm illumination and the wavelength dependence was compared with dark–field spectrum. The wavelength dependence follows dark–field spectrum well. Furthermore, some intense peaks of reduction product dimercaptoazobenzene (DMAB) are observed on anti–Stokes side. The mode selectivity of DMAB is coincide with calculated one. Meanwhile, 4–mercaptobenzonitrile (MBN) whose geometry is similar to NBT does not show any intense anti–Stokes and model calculation does not show mode selectivity of localized vibrational mode. These data strongly suggest that electrons activated by LSP transfers its energy to vibrational mode of specific chemicals.

Keywords : gap–plasmon, surface–enhanced Raman spectroscopy (SERS), vibrational pumping, metal–molecule energy transfer, picocavity, plasmon–induced electrons

Student Number : 2014–21228

Table of Contents

Chapter 1. Introduction

Part of this chapter (chapter 1.6. and 1.7.) is published at "*Appl. Mater. Today* 2019, 16, 112-119"

1.1. Importance of vibrational pumping on metallic surface

There have been many reports that the excitation of specific vibrational mode of reactant molecule may manipulate the pathway of gap phase chemical reaction.[1-2] Under infrared (IR) laser illumination, therefore, vibrationally excited gas phase molecules are easily prepared and the lifetime of vibration relaxation (τ_{VR}) of ~ 10 μs makes it possible to control the chemical reactions.[3]

For surface chemical reaction, however, vibrational control of the reaction is hard to be achieved because τ_{VR} on metallic surface is around a picosecond.[4] Because τ_{VR} of adsorbate molecules cannot be manipulated, it is expected that adsorbate reactants should be pumped efficiently for reaction control. However, there has been no noticeable report regarding such efficient vibrational pumping on metallic surface. In this thesis, I show highly efficient vibrational pumping of adsorbate molecules which can be interpreted as a result of (1) highly efficient SERS mechanism by atomic-scaled SERS

hotspot (picocavity SERS) and (2) resonant inelastic scattering of plasmon induced electrons. These pumping mechanisms induce considerable populations of vibrationally excited molecules in steady state and these are measured by SERS. Prior to show the evidences, in this chapter, I present some background needed to understand my works.

1.2. Localized surface plasmon (LSP)

LSP is the coupled oscillation of electrons in a nanoparticle (NP) and the electromagnetic field surrounding NP (Fig. 1).[5] Under illumination, LSPs are excited around the NP whose size is smaller than that of excitation wavelength. LSPs induce significant electromagnetic (EM) field enhancement around the NP and the state that LSP resonates with the incident light is called localized surface plasmon resonance (LSPR).[6] The resonant frequency of LSP is strongly correlated to the dielectric constant of metal, shape, size and the dielectric constant of surrounding medium of NPs[5] and EM field enhancement is maximized under this condition. Also, the field enhancement is stronger at sharp vertex or corner than that at smooth face.[7] To optimize the EM enhancement, excitation source or plasmonic platform should be chosen carefully.

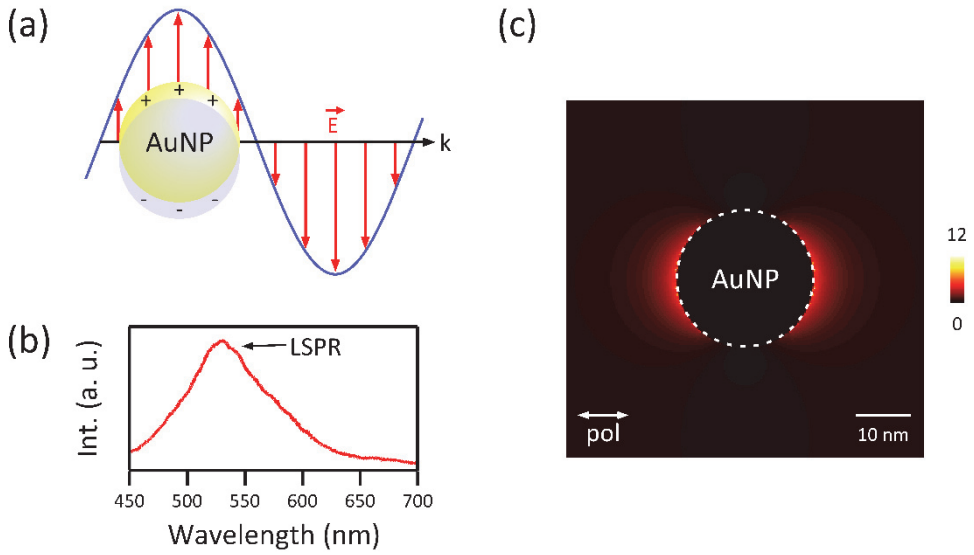

Fig 1. (a) Localized surface plasmon (LSP). Incident light oscillates the conductive electron cloud in NP. (b) Dark-field spectrum of AuNP (diameter of 50 nm) which represents the optical response of LSP. The colored arrow indicate the resonant frequency of LSP (c) Spatial distribution of LSP ($|E_{loc}|^2$) near the AuNP whose diameter of 50 nm under 690 nm excitation. The light is linearly polarized and the intense field is distributed parallel to polarization.

1.3. Gap-plasmon

The coupled LSP of adjacent two or more NP system is gap-plasmon. Unlike to LSP of monomer which disperses EM field to entire NP, this coupled LSP tightly confine the EM –field to narrow gap junctions (Fig. 2a).[7] As a result, more field enhancement of EM is expected to gap-plasmon than that of monomer.

For linear NP oligomer chain, there are longitudinal modes whose number is coincide with the number of NPs and one transversal mode.[8] Among the longitudinal gap-plasmon modes, the modes with even number of nodes are optically active (bright mode) and the others are inactive (dark mode). The dark modes are activated under specific condition only such as small molecular emitter located at narrow gap junction.[9] The gap plasmon modes of representative NP chain structure, NP dimer, are shown in Fig. 2b. Because the dimer is composed of two NPs, there are two gap-plasmon modes. One is bright mode which is called bonding dipole mode (BDP) and the other is optically dark mode which is called bonding quadrupole mode (BQP).[10]

In this thesis, experiments are conducted with NP on metallic thin film junctions (nanoparticle on mirror, NPOM) which are composed of AgNP (diameter of 80 nm) and AuTF (thickness of 10 nm). Under the light illumination, (1) LSP of NP is induced, (2) the mirror

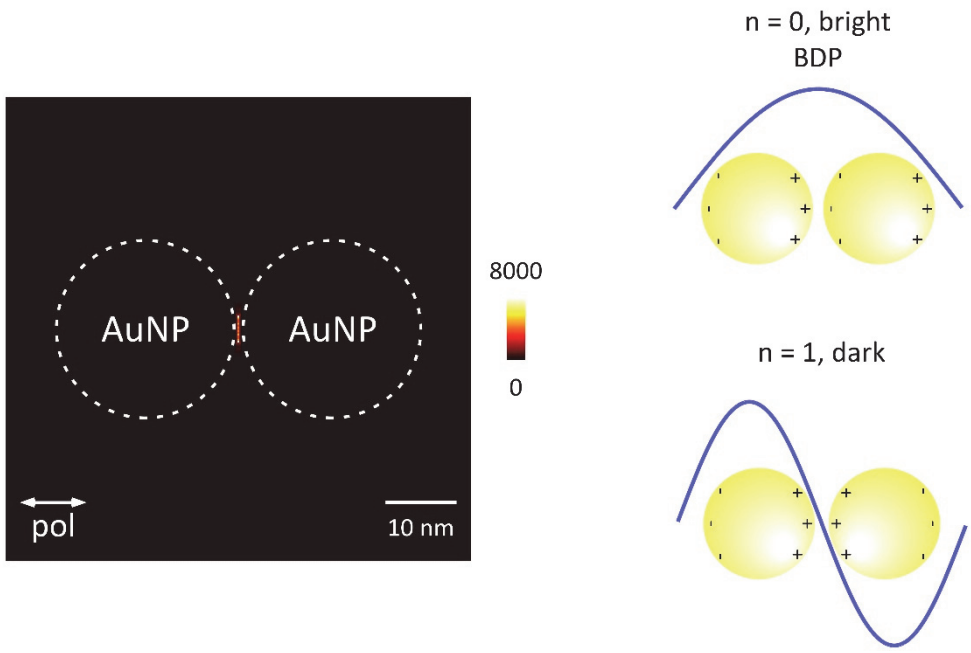

Fig 2. (a) Spatial LSP distribution ($|E_{loc}|^2$) around AuNP dimer (diameter of 50 nm, λ_{ex} = 633 nm). Incident light is polarized parallel to dimer axis. The enhanced field is tightly confined at gap−junction. (b) Gap−plasmon modes of NP dimer. Only BDP mode which has no node is bright.

image of it is generated on TF, (3) and coupled each other. Because the gap-plasmon of my SERS platform is coupling of LSP of the NP and its mirror image, the modes are similar to those of NP dimer.[5] For this NPOM system, only BDP whose LSPR is around 600 nm is optically active.[11] The BDP mode guarantees highly effective excitation of surface enhanced Raman scattering (SERS) with He-Ne light source I used (λ_{ex} of 632.8 nm).

1.4. Raman spectroscopy

Raman spectroscopy is one of the vibrational spectroscopy which take use of scattering process unlike to infrared (IR) spectroscopy.[12] There are three types of scattering process. One is Rayleigh scattering, another is Stokes Raman scattering and the other is anti-Stokes Raman scattering. Among these three processes, Raman spectroscopy collects Stokes and anti-Stokes scattering which exchanges their energy with scatterer.

Under light illumination, the electric dipole in a molecule oscillates with frequency of incident light and radiate photon with wavelength of incident one. This process is called Rayleigh scattering (Fig. 3a). In some cases, however, the frequency of the oscillating dipole is slightly modulated by vibrational motions of molecules. In these cases, radiated light energy is deviated from incident one as much as

vibrational energy of target molecule. This process is called Raman scattering. However, all vibrational modes of molecule do not induce Raman scattering. The motion of vibrational modes, to be Raman-active, should modulate the polarizablity of molecule ($d\alpha/dQ_i \neq 0$).[12] This condition is called Raman selection rule. If incident photon transfer to Raman-active vibrational mode of molecule, this process is called Stokes Raman scattering (Fig 3a). On the other hand, incident photon receive vibrational energy from the molecule, this process is called anti-Stokes Raman scattering (Fig. 3a). Raman spectroscopy collects scattered photon and represent the intensity of scattered photons in frequency domain.

Following Boltzmann statistics, generally, almost vibrational modes of organic molecules are in ground state and the population ratio between vibraionally excited state and ground state exponentially decays with the frequency of the vibrational modes. Even though Stokes scattering is exciting process, Stoke Raman is too inefficient to make vibraionally excited populations meaningfully. The excitation rate by Raman process is only (k_{exc}) ~ 10^{-6} s^{-1} for a molecule whose cross section of 10^{-30} cm^{-2} under illumination of 1 MW/cm^2 633 nm laser. Compared with relaxation rate (k_{rel}) ~ 10^6 s^{-1} for gas phase molecule, k_{exc} is too small to overcome k_{rel}.[3] In the same way, anti-Stokes scattering cannot reduce the vibrationally excited population.

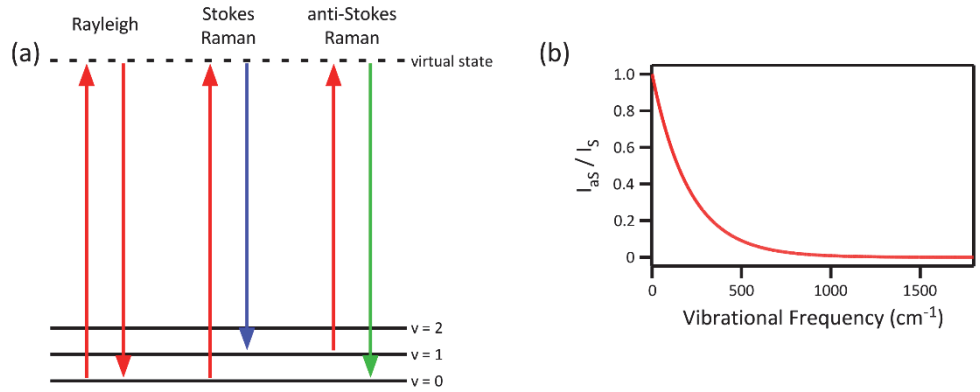

Fig 3. (a) Scheme of Rayleigh and Raman scattering. Molecules and photons do not exchanges their energy during Rayleigh scattering. On the other hand, molecules receive (transfer) their energy from (to) molecule during (anti−) Stokes scattering (b) Boltzmann curves represented in frequency domain of vibrational mode. The population of excited molecules in equilibrium exponentially decays with vibrational frequency.

As a result, only thermally equilibrated populations are observable by Raman spectroscopy and most of Raman scattering is Stokes because almost molecules are in vibrational ground state. Consequently, anti-Stokes intensity is only a portion of Stokes intensity and the ratio between anti-Stokes and Stokes intensity follows Boltzmann distribution (Fig. 3b). In short, the temperature of the sample can be estimated by intensity ratio between anti-Stokes and Stokes intensity. If Raman scattering process become super efficient supported by other process such as super efficient hot-spot, however, it may be possible that the Raman process itself alters the population from thermally equilibrium system.

1.5. Surface enhanced Raman spectroscopy (SERS)

Even though Raman process itself is inefficient process, Raman signal is greatly enhanced for scatterer in the proximity of the surface of metallic nanostructure. The spectroscopy which measures this enhanced Raman scattering is called surface enhanced Raman spectroscopy (SERS).[6] SERS means spectroscopy itself as well as the enhanced scattering.

The enhancement of SERS is achieved by two processes. One is EM enhancement mechanism and the other is chemical enhancement mechanism.[6] EM enhancement which is accepted as a main factor of

SERS enhancement mechanism is the LSP supported phenomenon.[6] LSP enhances not only incident field (the number of Raman excitation photon) but also that of scattered field (scattered photons) (Fig. 4a).[6] As a result, EM enhancement is proportional to fourth power of local field amplitude. The EM enhancement factor and SERS activity under the field enhancement are described below.

$$I_{SERS} \propto |E_0(\omega_0) \cdot \alpha_i \cdot E(\omega_0 \pm \omega_v)|^2$$

$$EF \propto |E_0(\omega_0)|^2 |E(\omega_0 \pm \omega_v)|^2 \approx |E_0|^4$$

,where I_{SERS} is SERS intensity, E_0 is incident EM field whose frequency is ω_0, α_i is Raman polarizability tensor and E is EM filed whose frequency is $\omega_0 \pm \omega_v$. With gap-plasmon assisted SERS platform, this mechanism enhances the signal with factor of 10^9 or more and this even makes it possible to observe Raman scattering of single molecule.[13] The EM enhancement is not uniform for incident photon energy and the energy of Raman scattered photons which depends on a vibrational mode participate to scattering. As a result, intensity ratio of each vibrational peaks may be severely distorted by the uneven optical response of gap-plasmon and the temperature cannot be estimated accurately by SERS.[14]

Also, this enhancement mechanism should be considered in depth from the view of that the number of vibration exciting photons is

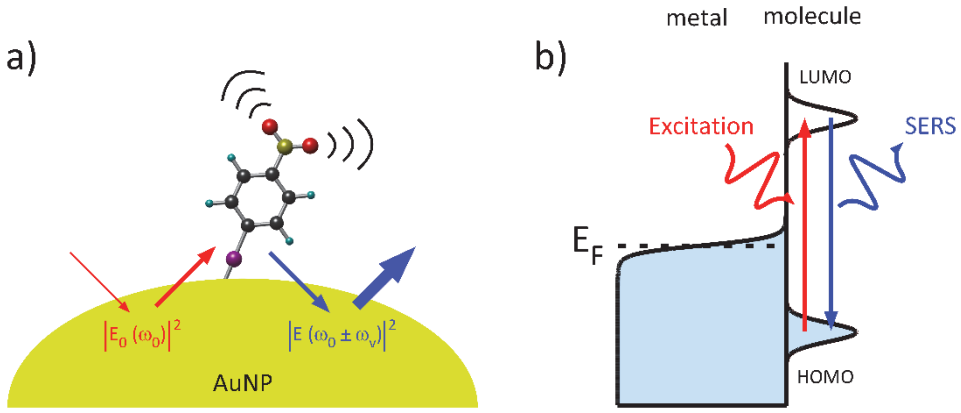

Fig 4. The scheme of SERS enhancement mechanisms (a) EM SERS enhancement. Firstly, the irradiated field is enhanced by LSP of NP. Subsequently, scattered SERS is enhanced by LSP. (b) Representative CE mechanism, resonant SERS mechanism. LUMO of molecule may be hybridized with metallic band and the energy of LUMO may be re-aligned.

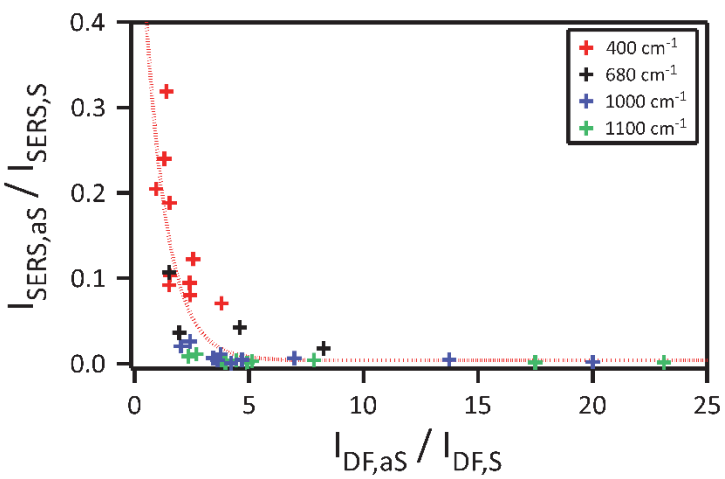

Fig 5. Intensity ratio between anti-Stokes and Stokes SERS ($I_{SERS,aS} / I_{SERS,S}$) plotted as a function of plasmonic asymmetry obtained from dark-field spectrum ($I_{DF,aS} / I_{DF,S}$). $I_{SERS,aS} / I_{SERS,S}$ decays with $I_{DFaS} / I_{DF,S}$ and converges to specific temperature.

greatly enhanced. If the EM enhancement factor is large enough that the rate of SERS excitation is comparable to vibrational relaxation (VR) whose rate of ~10^{12} s^{-1}, the substantial population of vibrationally excited molecules may be prepared in steady state. In reality, even though the k_{exc} does not seem to reach to k_{VR}, I collected data which may support this concept. The anti-Stokes to Stokes SERS intensity ratios ($I_{SERS,aS}$ / $I_{SERS,S}$) normalized by plasmonic asymmetry obtained from dark-field spectrum ($I_{DF,aS}$ / $I_{DF,S}$) (Fig. 5) decays with $I_{DF,aS}$ / $I_{DF,S}$ and converged to the $I_{SERS,aS}$ / $I_{SERS,S}$ corresponding to 260 K. For the junctions whose $I_{aS,DF}$ / $I_{S,DF}$ are small, compared to those whose $I_{aS,DF}$ / $I_{S,DF}$ are large, Stokes process receives stronger support by gap-plasmon. This may result in efficient vibrational pumping generating substantial population of vibrationally excited molecules. However, this hypothesis has not been confirmed and further studies such as effect of dark mode contribution to SERS signal or the effect of thermal heating are needed at present time. Then, clear evidence of meaningfully effective SERS process to pump vibrational modes exists? I also observed super effective SERS process under specific condition which is called picocavity SERS. The details are discussed in chapter 3.

All enhancement mechanisms except for EM enhancement are called

chemical enhancement (CE). Unlike to EM enhancement, metallic surface alters the polarizability of molecules.[6] Also, the adsorbate molecules on metallic surface may cause resonant Raman scattering (Fig. 4b).[6] In this thesis, the detail of CE mechanism is not discussed because this effect is not a key factor of my work.

1.6. Damping mechanisms of LSP

The excited LSP is rapidly damped via radiative damping and non-radiative damping pathways.[15-16] In the radiative damping pathway, energy is dissipated through the elastic scattering of incident photons, and is a preferred pathway for large NPs (> 20 nm). The far-field scattering efficiency as a function of wavelength corresponds to the familiar dark-field scattering spectra of NPs.[17] In the non-radiative decay path (Fig. 6b, c, and d), NP directly absorbs photon energy, generating highly energetic electron-hole pairs (Fig. 6b) through dephasing (Landau damping) process[18-19], which is the favored path for small NPs. The intrinsic dephasing timescale for Au and Ag is ~10 fs.[20] Such charge carriers have a transient, nonthermal energy distribution with approximately flat shape up to the excitation photon energy (Fig. 2b).[21-23] This highly energetic, nonthermal electron-hole pair scatters with the other carriers to form high-temperature Fermi-Dirac thermal distribution within ~100 fs (Fig. 6c).[22, 24-25] In

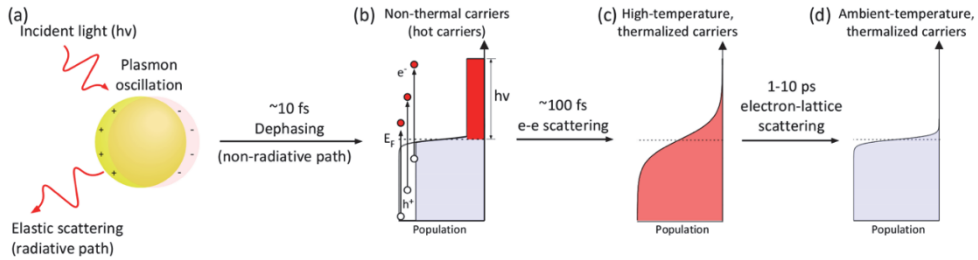

Fig. 6. Mechanism of LSP decay. (a) Light illumination (**hν**) induces plasmon excitation of a metallic nanoparticle, leading to elastic scattering (radiative path) and light absorption (non-radiative path). (b) Absorbed photons generate highly energetic, nonthermal charge carriers (hot carriers). (c) Nonthermal carriers are thermalized by inelastic electron-electron scattering. (d) Further thermalization to ambient temperature by electron-lattice scattering.

the plasmonics-related literatures, both of the two distributions are interchangeably called the hot carriers. Based on the chemical reaction outcome alone, it is not straightforward to tell which types of electronic distributions dominantly contribute to a given chemical reaction. In this thesis, I refer to hot carriers as the ones with nonthermal energy distributions. The excess electronic energy of hot thermal electrons is finally transferred to the lattice vibration of NP and to surroundings in 1-10 ps timescale (Fig. 6d).[22, 24-25] It is important to note that decay dynamics of all of the three processes are strongly influenced by multiple factors, including the geometry of NPs, surface states, and metal-adsorbate interactions.

1.7. Charge transfer mechanisms

In the standard indirect charge-transfer mechanism (Fig. 7a), hot carriers are created and subsequently transferred to the lowest unoccupied molecular orbitals (LUMO) of adsorbates.[15] Typical relaxation timescale for hot carriers is τ_{rel} ~100 fs, whereas typical metal-molecule CT transfer timescale is τ_{tr} ~ 10 ps or more.[26] Based on these timescales, charge transfer efficiency should be unmeasurably small (~10^{-6}), which, in many cases, contradicts what is observed. In fact, there exist theoretical and experimental evidences suggesting that carrier lifetimes of metallic NPs are

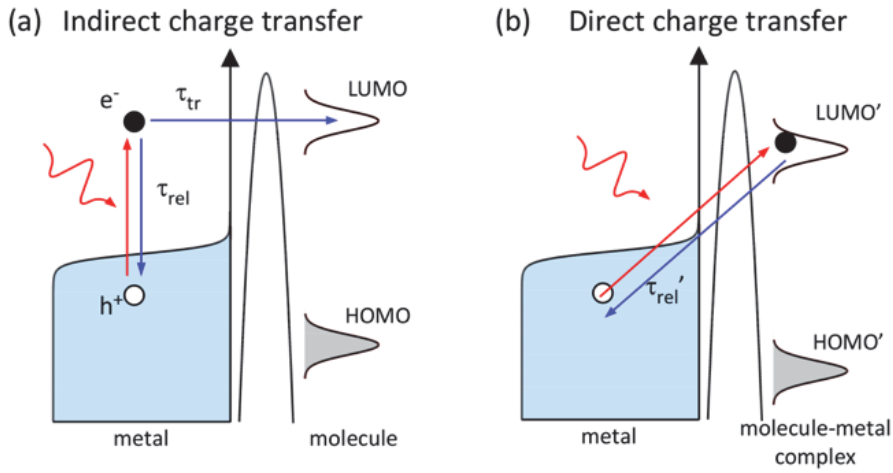

Fig. 7. Mechanisms of metal to molecule hot carrier transfer. (a) In indirect charge transfer, energetic electron is generated in metal and subsequently transferred to adsorbate. (b) In direct charge transfer, hot electron is generated directly onto the LUMO of molecule–metal complex in one–step.

significantly elongated as compared with those of bare, extended metals, allowing efficient metal–molecule charge transfer.

For small NPs, spatial confinement of carriers, discretized density of states, reduced electron–electron interactions, and reduced electron–phonon coupling can lead to delayed relaxation of carriers.[16, 27–28] In addition, presence of adsorbates on NP surfaces can elongate carrier lifetime. Specifically, Girault and co–workers[29–30] have measured hot carrier lifetime of ~ 1 ps for AuNPs capped with sulfates, which has been attributed to the multiple cycling of hot carriers between NP and adsorbate (called the chemical interface scattering). If the orbital hybridization between adsorbates and NP surfaces[26, 29, 31] is extensive such that metal–molecule complexes are formed, and also if the anionic state of the complex has a long lifetime, carrier–lifetime can be significantly elongated. In this case, charge carriers can be formed directly at metal–molecule complex (see Fig. 7b; called the direct charge transfer[15–16]) in one–step process. Rapid carrier relaxation in metal is replaced by slow reverse CT from the complex to NP, elongating the carrier lifetime ($\tau_{rel}' \gg \tau_{rel}$). Such direct charge transfer mechanism has been experimentally supported by the action spectra of demethylation of methylene blue (MB)[32] on Ag–NPs and LSP line–width broadening of CuO reduction.[33]

Chapter 2. Experimental Setup

2.1. Epi-confocal SERS spectrometer

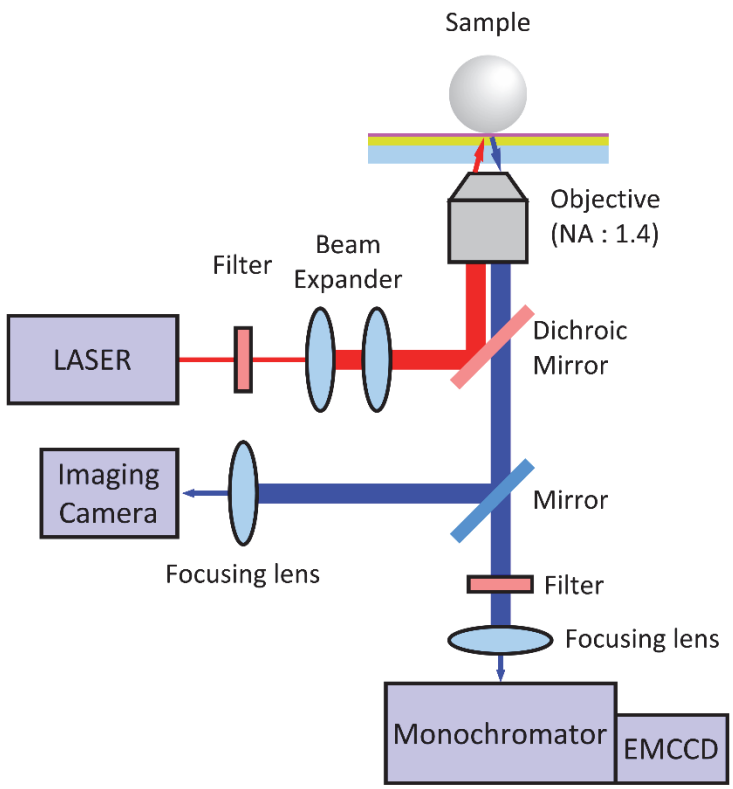

I used home-built epi-confocal SERS spectrometer equipped with inverted microscope (Olympus IX71). Excitation beam whose wavelength of 633 nm is irradiated from He-Ne laser (25-LHP-991-230, Melles Griot co). Firstly, the beam is filtered by colored line-filter (LL01-633-12.5, Semrock co.). After the filtering, the beam is expanded to diameter of 5 mm which is coincide with that of objective aperture. The expanded beam is reflected on dichroic

mirror (633 nm notch, Semrock NFD01-633-25x36) and focused on the sample by high NA oil-immersion objective lens (Olympus , NA of 1.4). The scattered light is collected by same objective lens. The scattered light is filtered by notch filter (Semrock 633 nm notch, NF03-633E-25) once again and focused on monochromator (Shamrock 500i). The light is separated by wavelength and the intensity of light is recorded by electron multiflying charged coupled device (EMCCD, Andor iXON 897). Additionally, imaging camera is equipped to the SERS spectrometer to find the position of nanoparticles.

2.2. Epi-confocal dark-field spectrometer

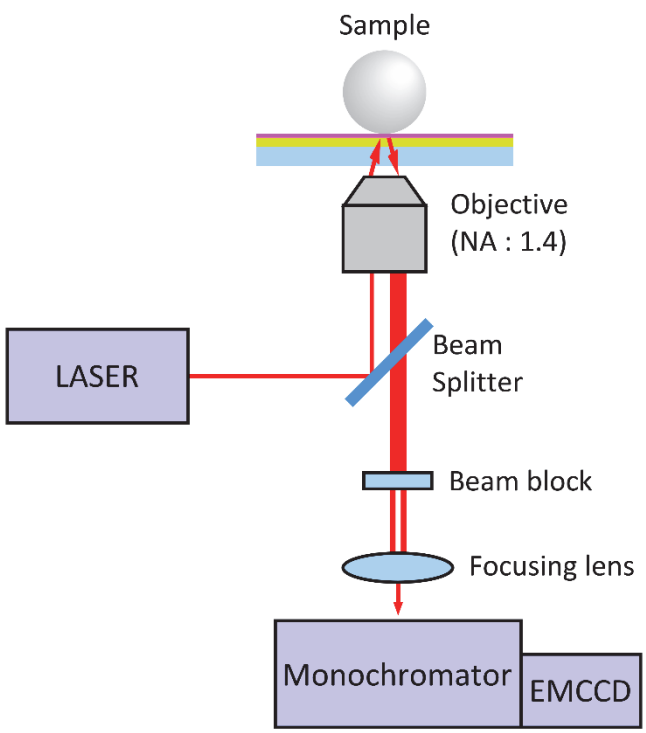

I used home-built dark-field spectrometer equipped with inverted microscope (Olypus IX71). The white laser beam is irradiated from super-continuum laser (FS024-020-021, NKT photonics co.). The narrow beam is reflected on beam splitter and focused on the sample by high NA oil-immersion objective lens (1.4 NA, oil-immersion type, U Plan S-Apo, Olympus co.) without expansion. The scattered light is collected by same objective lens subsequently. If the beam passes the center of objective lens, reflected beam proceed to the center of aperture and scattered light passes outside of aperture as well as the center of it. The scattered light is isolated from reflected light by beam block and subsequently focused on the monochromator (Shamrock 500i). The light is separated by wavelength and the intensity of light is recorded by EMCCD (Andor iXON 897).

Chapter 3. Frequency domain-prof of the existence of picocavity inducing super-efficient Raman pumping

3.1. Background

It is generally believed that the geometry of nanostructures (i.e., diameters, curvatures, and gap−sizes) governs the resonance wavelength and field confinement, and that the fine details of the surface structures (such as sub−nanometer (sub−nm) protrusions and surface defects) have insignificant effect. Such a view of plasmonics naturally leads to the limit of field confinement to a scale of ~10 nm. Indeed, signal enhancements in typical surface−enhanced Raman scattering (SERS)[6, 11, 34−50] can be satisfactorily explained by the action of gap−fields spanning lateral dimensions of ~10 nm at the junctions between near−touching nanoparticles.[5]

This limit of field confinement, however, is by no means a fundamental barrier. Recent classical[51], semiclassical[52], and full atomistic quantum[53−54] calculations on small metal clusters (~1 nm in diameter) and nanoparticles consistently suggest that sub−nm−sized or even single−atom−sized hot−spots could be formed on

atomically sharp protrusions. Whether or not the conclusions derived from small cluster models can be directly extrapolated to nanoparticles with sizes >50 nm still awaits confirmation. There exist a few notable experimental observations, which, among several possibilities, could be attributed to the action of sub-nm hot-spots. For example, several groups[55-58] observed sub-nm image features in tip enhanced Raman scattering (TERS) measurements, which could arise from sub-nm hot-spots at the apexes of scanning probes. In cryogenic SERS measurements[59], blinking spectra with abnormally large anti-Stokes versus Stokes intensity ratios were observed. In addition, they observed subtle site-specific variations in the spectral features. These observations were attributed to the interaction of the field with an effective mode volume of <1 nm^3 and a single molecule. Recently, it was proposed that TERS of a single-molecule with a sub-nm hotspot probe could reveal patterns that directly reflect atomic displacements of vibrational normal modes.[52, 60] In the frequency-domain, this corresponds to the prediction that sub-nm hot-spots which is called picocavity[59] would lead to molecular site-specific selection rules in the SERS spectra.

Here I present a new spectroscopic proof of the existence of picocavity on the surfaces of plasmon-excited nanostructures. The SERS spectra of 4,4′ -biphenyl dithiols (BPDTs) measured at room

temperature show blinking Stokes and anti-Stokes components that only exhibit one prominent vibrational peak. The activated vibrational peaks were found to vary between different junctions in the same sample. Such site specific, single-peak spectra could be explained by the single molecule SERS signal driven by a picocavity no larger than 3.5 Å, located at the specific molecular sites.

3.2. Experimental method

I observed SERS of 4,4' -biphenyldithiol (BPDT) sandwiched at gap junction which is composed of AgNP and AuTF. The AuTF is formed on the top of Ti adhesive layer whose thickness is 2 nm on cover glass substrate. A fully saturated self-assembled monolayer of 4,4′ - BPDT (Sigma-Aldrich; used without further purification) was formed on top of an AuTF. The Ag nanoparticles (AgNPs, diameters of 80 nm, BBI Co., Ltd.) were dispersed on top of the BPDT/AuTF surface to form AgNP-BPDT-AuTF junctions.

3.3. Calculation method

The FDTD calculation is carried out for AgNP-BPDT-AuTF junction with a commercial software (FDTD Solutions, Lumerical Solutions, Inc.). In this model, the BPDT monolayer is modeled as a thin film (with a refracted index of 1.45) of thickness of 1.1 nm placed

on top of a AuTF. The dielectric constants of Ag and Au used is from Palik.[61-62] A linearly polarized light is focused onto the junction with a numerical aperture (NA) of 1.45.

The density functional theory (DFT) calculations are carried out using Gaussian09 package[63] and employed the multilayer ONIOM (Our own N-layered Integrated molecular Orbital and molecular Mechanics)[64-65] method, in which different basis sets are used for metallic atoms (Ag and Au;in this case, I used the basis of LanL2DZ) and atoms comprising organic molecules (6-311G++ (d, p)).

3.4. Experimental result

Fig. 8a shows the structure of a self-assembled AgNP-BPDT-AuTF plasmonic junction and the experimental setup. The BPDT forms covalent bridges with the surfaces of AgNP (average diameter of 80 nm) and AuTF (thickness of 10 nm) and provides an average gap-distance of 1.1 ± 0.1 nm.[66] A focused laser beam (power density of ~ 1 MW/cm^2) with a wavelength λ_{ex} = 633 nm was impinged on individual junction sites, and the anti-Stokes and Stokes spectra were simultaneously recorded by a Raman spectrometer. Assuming that a spherically shaped AgNP and a flat AuTF create a gap of 1.1 nm, I was able to estimate the enhancement factor (EF), the area of SERS hot spot and the number of molecules at gap-

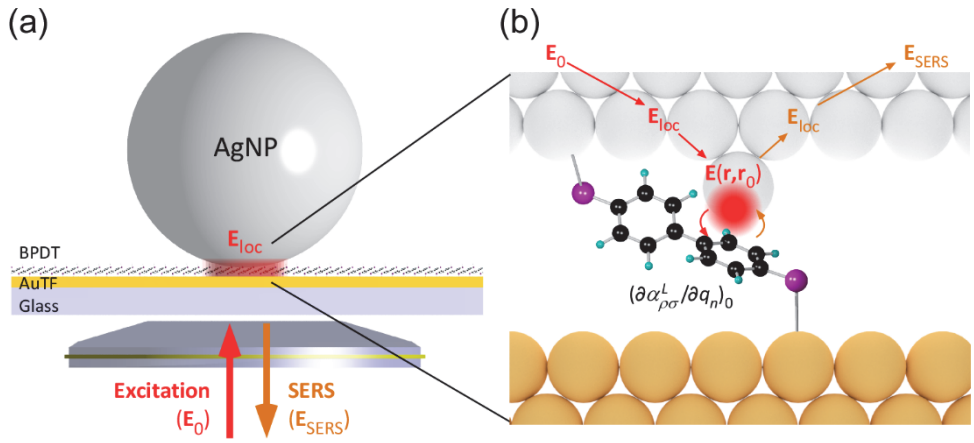

Fig. 8. Structure of the AgNP−BPDT−AuTF junction and the modeling of single−molecule SERS signals induced by a picocavity. (a) AgNP−BPDT−AuTF junction and SERS measurement. (b) Coupling scheme for the SERS induced by picocavity: far−field excitation field (E_0) induces a gap−field (E_{loc}), which excites a picocavity $E(r,r_0)$ at the end of sub−nm protrusion (r_0) on AgNP or AuTF surfaces. Picocavity locally excites Raman radiation of a BPDT molecule, and the Raman radiation is out−coupled to the picocavity $E(r,r_0)$, then to the gap mode E_{loc} and finally scattered to the far−field (E_{SERS})

junction. These are estimated based on field distribution calculated by finite-difference time-domain (FDTD) calculation (see method). To model the field enhancement, I have separately calculated the in-coupling of the excitation light with the plasmon mode at the excitation frequency (ω_0), $|E_{loc}(\omega_0)/E_0|^2$, and the out-coupling of the near-field Stokes-shifted Raman field radiation at ω_{v1} with the far-field radiation, $|E_{loc}(\omega_{v1})/E_0|^2$, and multiply the two to obtain the position-dependent Raman enhancement factor of ω_{v1} (BPDT) = 1576 cm^{-1}:

$$F_{v1}(x,y) = |E_{loc}(\omega_0,x,y)/E_0|^2|E_{loc}(\omega_{v1},x,y)/E_0|^2$$

, where the x and y are the Cartesian coordinate of a BPDT molecule on AuTF surface with respect to the junction center (0,0). The distribution of field enhancement $F(x,y)$ is displayed in Fig. 9. The enhancement factor listed in Table 1 shows both the $F_{v1,max}$, the maximum EF for a given hotspot (EF_{max}), and the enhancement factor averaged over the hotspot area (EF_{avg}). Also shown in Table 1 are the area of hotspot (A), and the number of BPDT molecules (N) experiencing substantial field enhancement. The experimental Raman enhancement factor (EF) of the AgNP-BPDT-AuTF junction is estimated by comparing the 1576 cm^{-1} peak of the normal Raman scattering spectra (I_{Raman}) of solid BPDT powder, and the

Physical dimensions of hotspot[b]		Model EF		Experimental EF (ν_1)[a]
A (nm^2)	N	EF_{max}	EF_{avg}	
17	58	2.1 x 10^6	1.5 x 10^6	2.0 x 10^5

Table. 1. Plasmonic field enhancement of AgNP–BPDT–AuTF junction. (a) For details of calculation, see Park et al[67], (b) The theoretically estimated values. The A is the field-enhanced area on Au surface that experiences F_{v1} larger than 0.5 $F_{v1,max}$, where $F_{v1,max}$ is maximum field enhancement. The N is the number of BPDTs within A

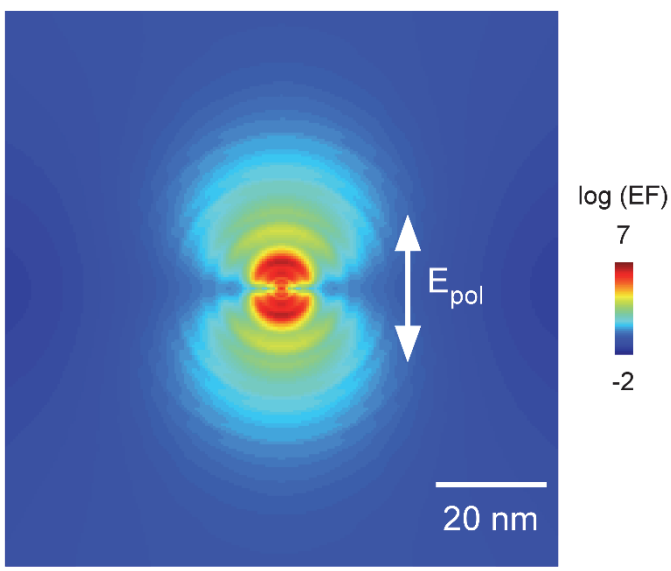

Fig. 9. FDTD-calculated $|E(\omega_0)|^2 \cdot |E(\omega_{v1})|^2$ distribution on the surface which is normal to the direction of light progression. The white arrow is the direction of polarization of light which is parallel to the surface. The color scale of the image is logarithmic.

corresponding SERS signals (I_{SERS}) from a AgNP–BPDT–AuTF junction, obtained under the same experimental conditions. For the estimate, surface density of BPDTs on AuTF of ρ_S = 3.4 molecules / nm^2, (estimated from that of biphenyl thiol[68]) and volume density of ρ_v = 4.06 molecules / nm^3 (estimated from biphenyl[69]) are used. These parameters yield an experimental enhancement factor of EF = 2.0 × 10^5 for the ν_1 peak of BPDT (see Park et al[67] for more details of estimation procedure).

Fig. 10a–f displays two SERS trajectories recorded from two different junction sites (the low–frequency peaks with < 500 cm^{-1} were blocked out by a Raman notch filter). The spectra are composed of blinking and stationary components: the trajectories show three Raman–allowed peaks at 1576, 1275, and 1075 cm^{-1} (see Table 2 for peak assignment), which are stationary in intensity and frequency. In addition to such stationary components, I observe Stokes and anti–Stokes peaks (a peak at 998 cm^{-1} in Fig. 10a and a peak at 1576 cm^{-1} in Fig. 10d; see red and green arrows in the figures) exhibiting simultaneous on/off blinking. Fig. 10b,e shows the same trajectories as those depicted in Fig. 10a,d, respectively. In these spectra, however, the time–averaged SERS spectra sampled during the off–period were subtracted to selectively display the gap–field enhanced SERS signal of ~60 BPDTs at the gap, whereas the blinking

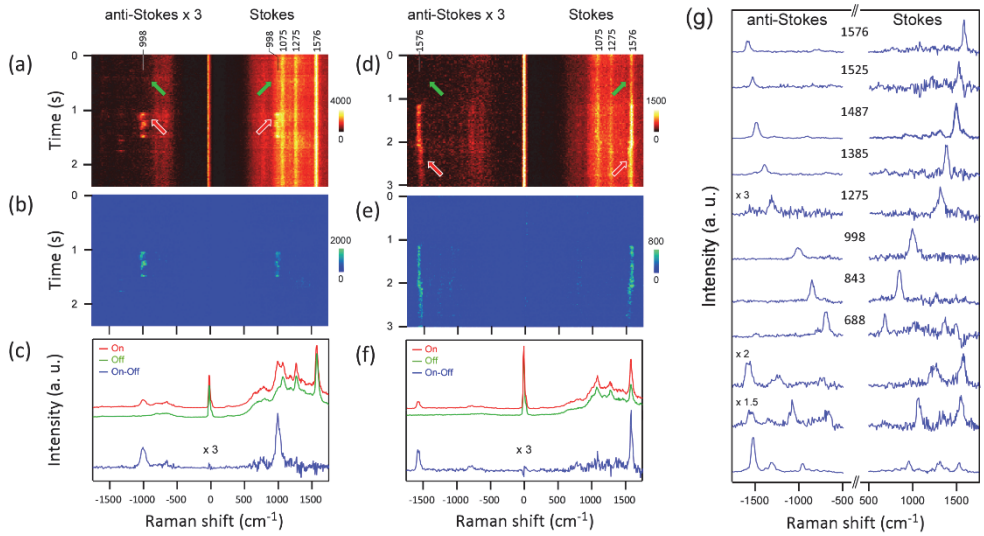

Fig. 10. SERS trajectories showing Stokes and anti-Stokes blinking. (a) Time-resolved Stokes and anti-Stokes SERS spectra obtained from a AgNP-BPDT-AuTF junction showing on (red arrow)/off (green arrow) blinking of a peak at 998 cm^{-1} (ring-deformation mode). The low frequency range (ν = −500 to +500 cm^{-1}) is blocked out by a Raman notch filter used in the measurement. (b) Blinking component of the trajectory in (a): spectrum at each time delay is subtracted from an average SERS spectrum sampled during the off-period. (c) SERS spectra sampled during on (red arrow in (a)) and off (green arrow in (a)) periods. The two are displaced along the y-axis to better show the spectral features. Also shown in blue is the difference between the on and off spectra for the blinking component. (d-f) Another set of SERS trajectory data with pronounced blinking peak at 1576 cm^{-1} (aromatic C-C stretching). (g) Collection of blinking components (on-off) showing single-peak SERS spectra (top eight spectra, frequencies of the peaks are shown in cm^{-1}) as well as multipeak spectra (bottom three spectra). In these spectra, relative intensities of the Stokes and anti-Stokes peaks are not rescaled unless specified. For the assignment of the peaks, see Table 2.

Frequency (cm^{-1})	D_2-group irreducible representation	Observation type	Assignment
1576	A	stationary / blinking	aromatic C-C stretching
1525	B	blinking	ring deformation
1478	A	blinking	H-C=C-H rocking coupled to ring deformation
1462	A	blinking	H-C=C-H rocking coupled to ring deformation
1385	B	blinking	HC-CH scissor
1275	A	stationary / blinking	C-C stretch combined to C-S-Ag/Au motion
1075	A	stationary	C-S in-plane stretching
998	A	blinking	ring deformation
843	A	blinking	C-H out-of-plane deformation
688	B	blinking	ring deformation

Table 2. Major vibrational modes of BPDT observed from the stationary and blinking components of SERS spectra

component corresponds to a SERS signal of a single BPDT molecule (or very few BPDT molecules) receiving an extra enhancement.

I found that, for a given trajectory, the Stokes and anti-Stokes blinking occurs for a subset of vibrational modes of BPDT, and such selectivity is found to be site-specific: Fig. 10g shows a collection of blinking spectra obtained from various junction sites, showing wide variation in spectral features. More strikingly, many of the blinking components (about 40%) show only one prominent vibrational peak (within the observation window of 500-1600 cm^{-1}), and some of the peaks were identified as Raman-forbidden modes (for example, the peak at 998 cm^{-1}). The shape of SERS spectrum may be governed by the orientation of molecule (surface-selection rule[48]). I investigated whether such single peak blinking is able to be explained by simple temporal orientation alteration of BPDT. Fig. 11. represents simulated SERS spectra of BPDTs with various orientations under uniform EM field. With the exception of the single-peak spectra with a peak at 1575 cm^{-1} (the strongest peak of BPDT in normal Raman scattering), none of the single-peak spectra could be explained by the surface-selection rule of differently oriented single-molecules. Simulated single peak spectrum of 1075 cm^{-1} is calculated at specific orientation of BPDT. However, the blinking of the peak is not observed by experiment. Except for

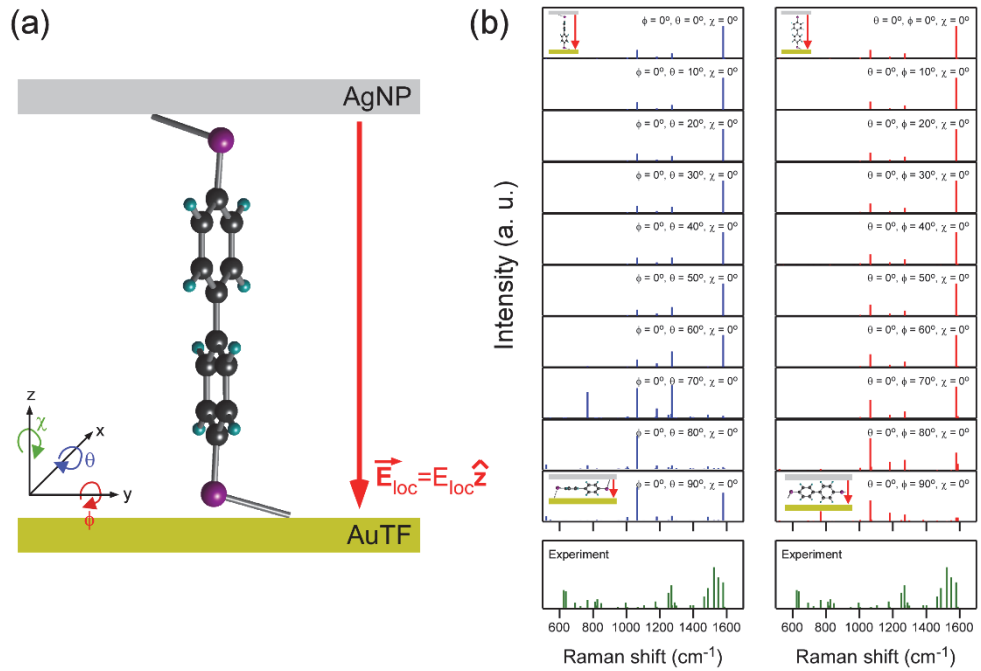

Fig. 11. Molecular orientation (θ,ϕ,χ) of BPDT at gap junction. Local field ($\vec{E}_{loc} = E_{loc}\hat{z}$) is parallel to z−axis. The orientation (θ,ϕ,χ) = (0,0,0) corresponds to the case where major axis of BPDT is aligned parallel to the local field vector. (b) Simulated SERS spectra of BPDT with various (θ,ϕ,χ). The inset cartoons show the orientations of BPDT. Also shown at the botton of the spectra are the experimental SERS peak distribution of blinking components.

molecular orientation issue, the Raman-forbidden peaks possibly arise from chemical enhancement or from field-gradient SERS (FG-SERS).[70-74] However, the spectra do not appear to follow the symmetry selection rules of the chemical enhancement.[75-76] Instead, the FG-SERS, in which Raman transitions are driven by the gradient of local electric field, may explain not only the appearance of Raman-forbidden transitions but also the site-specific spectral features.

The ratio of the anti-Stokes and Stokes intensities of the peaks ($\rho_k = I_{aS,k}/I_{S,k}$, where $I_{aS,k}$ and $I_{S,k}$ are the intensities of the anti-Stokes and Stokes peaks of the k-th vibrational mode, respectively) is abnormally large (spectra in Fig. 10c,f reveal ρ_k= 0.45 and 0.49 for the peaks at 998 and 1576 cm^{-1}, respectively), as compared with the ones expected for the room-temperature thermalized BPDT (ρ_k = 0.018 and 0.0026 for the two modes shown, calculated neglecting the plasmon resonance asymmetry; see below). The blinking anti-Stokes peaks are similar to those previously observed under ambient[77] and cryogenic conditions[59]. It is possible that these abnormal ρ_k's are induced by the (1) plasmon-resonance asymmetries of anti-Stokes and Stokes Components[14, 78] or (2) photo-thermal heating. Based on SERS and dark-field spectroscopy, I investigated the effects of such effects on these abnormal ρ_k. In the electromagnetic (EM) mechanism of SERS, the plasmon resonance

asymmetry in the anti-Stokes and Stokes signal, which is defined as $\gamma_i = |E_{loc}(\nu_0 + \nu_i)|^2 / |E_{loc}(\nu_0 - \nu_i)|^2$ (where $E_{loc}(\nu)$ is the plasmonic local field at frequency, ν. The ν_0 and ν_i are frequencies of excitation light and i'th normal mode vibration, respectively.), may influence the anti-Stokes to Stokes SERS intensity ratio (ρ_i) through:

$$\rho_i = \gamma_i \left(\frac{\nu_0 + \nu_i}{\nu_0 - \nu_i}\right)^4 \frac{n_{ex,i}}{n_{gr,i}} \cdots\cdots (1)$$

,where the $n_{ex,i}$ and $n_{gr,i}$ are the vibrational populations of molecules at the first excited and ground state of ν_i-mode, respectively. For the particular case of NP-TF junctions, excitation wavelength dependence on SERS signals closely follow the far-field scattering spectra.[79] As such, I approximate γ_i as the ratio of dark-field scattering intensities (see lower panel of Fig. 12a) at the wavelengths at which anti-Stokes and Stokes peaks of i'th vibrational peak appears ($\gamma_i = I_{FF,aS,i}/I_{FF,S,i}$). The ratio ρ_i (blinking and stationary components) of SERS signals obtained from the same junction site (see upper panel of Fig. 12a) is measured. Fig. 12b displays such $\rho_i - \gamma_i$ correlations for blinking (filled markers) and stationary (empty markers) SERS components with various vibrational frequencies. Also shown are the $\rho_i - \gamma_i$ curves expected for (see eqn. 1) peaks at the vibrational frequencies of 700 cm^{-1} and

1600 cm^{-1} for BPDTs with room−temperature equilibrium population distribution ($n_{ex,i}/n_{gr,j} = \exp(-h\nu_i/k_BT)$). On the average, the ρ_is for blinking and stationary components are separated by 1−2 orders of magnitudes. Most (> 90%) of γ_i stay within a range of γ_i = 1 − 3.5, with the most probable γ_i around 2. I was unable to observe any clear positive correlations ρ_i − γ_i for blinking or stationary components (see eqn 1), possibly due to the limited γ_i−variation. Nevertheless, I do find that $\rho_{i,stationary}$ − γ_i stay close to (within a factor of 10) the model curves for ambient temperate (T = 298 K), whereas the $\rho_{i,blinking}$ correlation far exceeds the model. In particular, (ρ_i, γ_i) of blinking and stationary components extracted from the same SERS trajectory (see filled and empty circles in blue, and a dashed arrow in Fig. 12b) also show the consistent difference. Finally, I have attempted to measure possible discrete spectral jumps in the dark−field spectra under the similar illumination fluence in Fig. 12d, and found no discrete spectral jumps in dark−field spectra. These show that both the blinking and stationary ρ_i may be affected by the static plasmon resonance asymmetry by a factor of γ_i = 1.0 − 3.5, but it cannot be the main cause of 1−2 orders of changes in ρ_i for stationary and blinking components. Rather, this anomaly reflects unusually hot vibrational distribution for blinking components. For multipeak spectra (see Fig. 10g), the spectral features of anti−

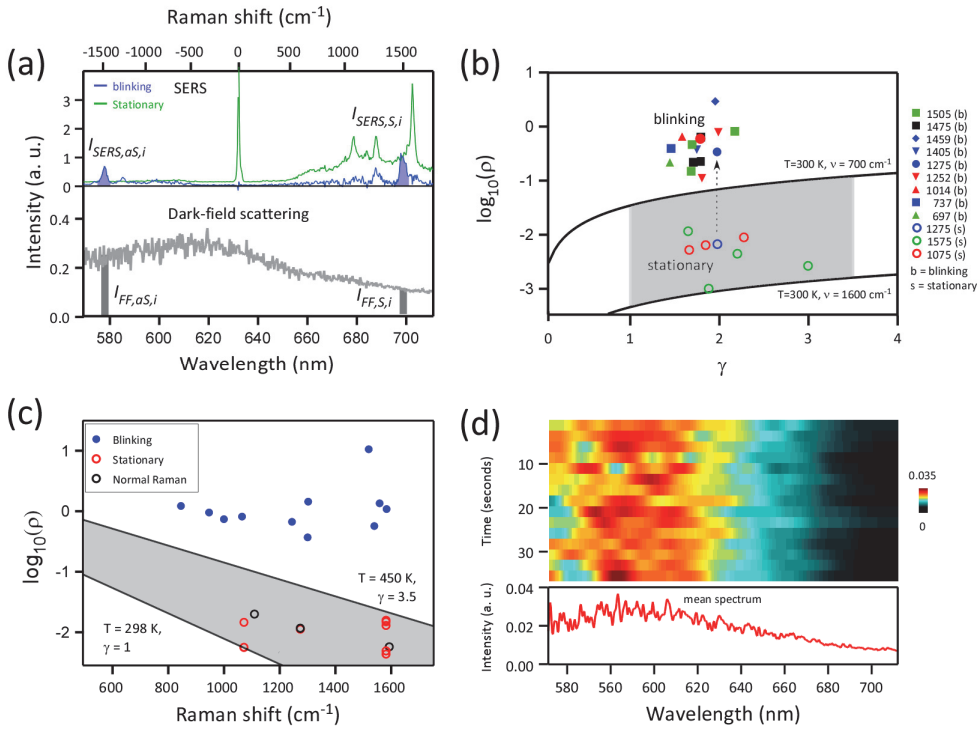

Fig. 12. Possible plasmon−resonance asymmetry contribution to anti−Stokes versus Stokes intensities and hyperthermal vibrational distribution. (a), upper panel: SERS spectra of stationary (green) and blinking components (blue) from a AgNP−BPDT−AuTF junction. Lower panel: dark−field spectrum (gray) obtained from the same junction. (b) Correlation plot of ρ_i and γ_i (resonance asymmetry, the ratio of intensities of dark−field spectra at the wavelengths corresponding to the anti−Stokes and Stokes branches of i' th peak $\gamma_i = I_{FF,aS,i}/I_{FF,S,i}$) obtained from the same AgNP−BPDT−AuTF junction. The plot shows correlations for stationary component (blank markers) and blinking components (filled markers) with various vibrational frequencies (vibrational frequencies for correlation points are show in legend on right). The dotted arrow point to the pair of ρ_i' s (filled and empty blue circles) of blinking and stationary components of the same peak at 1275 cm^{-1} measured from the same trajectory. Also shown in solid curves are $\rho_i-\gamma_i$ correlation expected for SERS signals at n = 700 cm^{-1} and 1600 cm^{-1} arising from thermally equilibrated BPDT molecules at temperature T = 298K. (c) $\rho_i-\nu_i$ correlation (where ν_i is the

vibrational frequency) for blinking SERS component (filled circles, blue), stationary SERS component (blank circle, red), and normal Raman spectrum of BPDT powder. Also shown in solid curves are the correlations expected for thermalized BPDT molecules at T=298K with resonance asymmetry γ = 1.0, and at T = 450 K with resonance asymmetry γ = 3.5. (d) upper panel: the time-resolved dark-field spectra from a AgNP-BPDT-AuTF junction. Lower panel: averaged dark-field spectrum of the junction sample from upper panel.

Stokes spectra and Stokes components (relative intensities among the activated peaks) are similar to each other. Again, this similarity is unusual because the anti−Stokes spectra of fully thermalized BPDTs should be heavily modified from Stokes spectra by the Boltzmann factors of vibrational energies of each peak $I_{aS,k} \approx I_{S,k} g_k exp(-h\nu_k/k_B T)$, where g_k, ν_k, k_B, and T are mode degeneracy, mode frequency, Boltzmann constant, and sample temperature, respectively). Fig. 12c displays $\rho_i - \nu_i$ correlation diagram for stationary SERS, blinking SERS, and normal Raman spectra of powder BPDT, all obtained with the same spectrometer. Also shown are the $\rho_i - \nu_i$ curves expected for Boltzmann population distribution of BPDT at T = 298 K and at T = 450 K, corrected by possible resonance asymmetries of γ_i = 1.0 and 3.5. The $\rho_i - \nu_i$ correlation for normal Raman spectra of solid−phase BPDT and stationary SERS components could be fitted to T = 298 K Boltzmann distribution with an average plasmon asymmetry correction of γ_i = 2. On the other hand, the ρ_i for blinking component far exceeds (by up to 2−3 orders of magnitude) the expectation for room−temperature Boltzmann distribution. Furthermore, the $\rho_i - \nu_i$ correlation show no resemblance to any single−temperature Boltzmann distribution, indicating that simple opto−thermal (statistical) heating of junctions cannot explain the observation. Overall, the correlation studies above

show that anomalously large anti-Stokes peaks in the SERS spectra is not caused by opto-thermal effect or by asymmetric resonance bias. Rather, it reflects hyperthermal (non-equilibrium) population distributions induced by the action of laser excitation and plasmonic gap structures.

Similar to photothermal heating, simple energy transfer from the surroundings (for example, through hot-electrons transfer from metallic surfaces) may enhance the anti-Stokes intensities and thus lead to ρ_i values far exceeding room temperature values. However, such energy transfer processes including heating cannot explain simultaneously blinking Stokes spectra. The mechanism that can enhance both the Stokes and anti-Stokes transitions is the enhanced Raman scattering rate itself.

3.5. How much of enhancement factor is needed to achieve this excitation ?

To achieve hyperthermal anti-Stokes signals, the Raman scattering rate per molecule ($\gamma_{Raman,i}$) should be non-negligible as compared with the rapid vibrational relaxation rate of the molecules (typically, $\gamma_{VR,i}$ = 10^{10}-10^{12} s^{-1} for organic molecules on metals[80]). I use phenomenological rate-equation approach to infer how much enhancement factor is required to achieve such high ρ_i. In this

inference, it is assumed that only fundamental vibrational transitions (v_i= 0 → 1 and 1 → 0) contribute to the observed SERS spectra. The Stokes (S) and anti-Stokes (aS) Raman scattering rates for i'th vibrational mode are given by:

$$\Gamma_{S,i}(0 \rightarrow 1) = \gamma_{Raman,i} \cdot n_{0,i} = \sigma_i J n_{0,j}$$

$$\Gamma_{aS,i}(0 \rightarrow 1) = \gamma_{Raman,i} \cdot n_{1,i} = \sigma_i J n_{1,j}$$

, where $\gamma_{Raman,i}$, σ_i, $n_{0/1,i}$, and J are the Raman scattering rate coefficient (Raman scattering rate per molecule), Raman scattering cross section, population in ground (v_i = 0) and the first excited (v_i = 1) vibrational states, and the laser photon flux, respectively. Raman scattering cross sections (σ_i) and Raman scattering rates per molecule (γ_i) for the Stokes and anti-Stokes transitions are assumed to be the same.

Two kinds of vibrational relaxations need to be considered. First, the relaxation ($\Gamma_{VR} = \gamma_{VR,i} \cdot n_{i,j}$) that brings vibrationally excited state (v_i = 1) population directly to its ground state (v_i = 0). Second, the relaxation ($\Gamma_{IVR,j} = \sum_j \gamma_{IVR,j \rightarrow i} \cdot n_{ex,i}$) that randomizes the specific vibrational excited state (v_i = 1) into other vibrational modes (v_j= 1) (intra-molecular vibrational relaxation, IVR), which is caused by non-zero anharmonicities of molecular vibrations. Both of the processes are known to occur in the time scale of picoseconds to a

few tens of femtoseconds. The IVR tend to randomize the excited-state population. The rate equation for the excited-state population is then given by:

$$\dot{n}_{1,j} = +\sigma_i(n_{0,i} - n_{1,i})J - \left(\gamma_{VR,i} + \sum_j \gamma_{IVR,i\to j}\right)\cdot n_{1,i} + \sum_j \gamma_{IVR,j\to i}\cdot n_{1,j}$$

Depending on the relative magnitudes of rates of Raman scattering, VR, and IVR, the resulting anti-Stokes spectral features assume different forms.

Assuming that the rate of IVR is negligible, I only consider the specific case that rate of SERS is comparable to VR rate. In this case, the ρ_i under steady state illumination is given by:

$$\rho_i = \frac{\gamma_{Raman,i}}{\gamma_{Raman,i} + \gamma_{VR,i}} = \frac{\sigma_i J}{\sigma_i J + \gamma_{VR,i}} \cdots\cdots (2)$$

Typically, I observe ρ_i = 0.2, which, according to the eqn. 2, reveals that Raman scattering rate is one quarter of the VR-rate.

In experiment, I was unable to carry out quantitative measurements on the enhanced Raman scattering rates and the efficiencies of vibrational pumping (for example, by laser power-dependent ρ_k measurement[78, 81]) because of the short duration time (typically a few seconds) of the blinking components. Nevertheless, it is clear that

such Raman scattering rate cannot be achieved with our SERS platform with an maximum enhancement factor (EF_{max}) ~ 10^6. For example, with a laser illumination of λ_{ex} = 633 nm and power density of ~1 MW/cm^2, the SERS rate is estimated to be only ~10^2 s^{-1} for a molecule with a typical Raman cross-section of ~10^{-28} cm^2/sr placed in our plasmonic gap. To achieve pumping rate of one quarter of the VR rate, at least, EF of 10^{13} is required assuming the $\gamma_{VR,i}$ = 10^{10} / s.

3.6. Model calculation of picocavity SERS

I claim that the picocavity in the metallic-gap led to the site-specific vibrational selections rules[52, 60] activation of the Raman-forbidden modes, and hyperthermal anti-Stokes signals. Such hot-spots can generate FG-SERS, activating some of the Raman-forbidden modes. Specific locations of the picocavity with respect to atomic coordinates of a molecule can lead to site-specific vibrational selection rules. With sufficiently small and bright hot-spots, SERS could be efficient enough to compete with rapid vibrational relaxations, which may lead to hyperthermal anti-Stokes signals. Below, I specifically focus on modeling the single-peak SERS spectra in the blinking components since they constitute the most extreme cases of site-specific vibrational selection and thus could provide the

most clear-cut insight into the interaction between a picocavity and a single molecule.

To search for the configurations of picocavity that give rise to the observed single-peak spectra, the coupling model (see Fig. 8b) developed by the group of Aizpurua[55, 59, 82] was employed. A laser illumination ($\vec{E}_0(\nu_0)$, where ν_0 is the excitation laser frequency) of a plasmonic junction generates a gap-field ($\vec{E}_{loc}(\nu_0) = E_{loc}(\nu_0)\vec{\varepsilon}_{loc} = E_{loc}(\nu_0)\hat{z}$, with a gap-axis $\hat{z}$ aligned along the z-direction), which is locally uniform on The gap-field, in turn, generates an Angstrom-sized field distribution $\vec{E}(\nu_0, \vec{r}, \vec{r}_0)$ (where $\vec{r}$ and $\vec{r}_0$ are the field-point and the center of the picocavity, respectively) around a sub-nm protrusion (at $\vec{r}_0$) on the metallic surface. A recent atomistic quantum calculation[53] on metal clusters indicates that a single atomic protrusion could generate an Angstrom-sized field that is distributed approximately isotropically around an atom. Here such a field is modeled by an isotropic Gaussian distribution with a radially diverging field vector:

$$\vec{E}(\nu_0, \vec{r}, \vec{r}_0) = F \cdot \left|\vec{E}_{loc}(\nu_0)\right| \cdot \frac{\vec{r} - \vec{r}_0}{|\vec{r} - \vec{r}_0|} \cdot \exp\left(-\frac{|\vec{r} - \vec{r}_0|^2}{a^2}\right)$$

$$= E(\nu_0)\vec{\varepsilon}(\vec{r}, \vec{r}_0)$$

where $\vec{\varepsilon}(\vec{r}, \vec{r}_0) = \frac{\vec{r}-\vec{r}_0}{|\vec{r}-\vec{r}_0|} \cdot \exp\left(-\frac{|\vec{r}-\vec{r}_0|^2}{a^2}\right)$ and a represent the shape

(picocavity mode) and the size (fwhm = $2\sqrt{ln2}a$) of the field distribution centered at position $\vec{r}_0$, respectively. The $\vec{E}$ is independent of the vectorial direction and frequency of the driving $\vec{E}_{loc}$−field, and F, the relative field enhancement of $|\vec{E}|$ with respect to $|\vec{E}_{loc}|$, is sufficiently large so that a single molecule near the picocavity primarily experiences $\vec{E}$. This $\vec{E}$ excites the Raman transition of the molecule, and the resulting radiation at frequencies $\nu_0 \pm \nu_k$ (where the + and − signs correspond to anti−Stokes and Stokes components with vibrational frequency ν_k, respectively) is out−coupled to the same picocavity mode ($E(\nu_0 \pm \nu_k)\varepsilon(\vec{r},\vec{r}_0)$), then to the gap−mode ($\vec{E}_{loc}(\nu_0 \pm \nu_k)\vec{\varepsilon}_{loc}$), and finally to the far−field, where it is detected as Stokes and anti−Stokes SERS signals. The in− and out−coupling between $E(\nu_0 \pm \nu_k)\varepsilon(\vec{r},\vec{r}_0)$ and $\vec{E}_{loc}(\nu_0 \pm \nu_k)\vec{\varepsilon}_{loc}$ are assumed to be polarization− and frequency−independent. Thus, the SERS spectrum of a single molecule is completely determined by the spatial configuration ($\vec{r}_0$ and a) of $\varepsilon(\vec{r},\vec{r}_0)$ and molecular geometry and is not dependent on the molecular orientation with respect to the junction axis.

In general, the SERS signals induced by field distributions much smaller than molecular sizes cannot be described by the polarizability derivatives with respect to normal mode coordinates of the molecule. To rigorously describe the interaction of $\varepsilon(\vec{r},\vec{r}_0)$ and a single

molecule, matrix elements of a multipolar light−molecule interaction Hamiltonian[83−84] and their partial derivatives with respect to normal mode coordinates should be numerically evaluated. However, under the assumptions that the field gradient at the length scales of atomic displacements of molecular vibration (typically < 50 pm) is negligible; that small displacement of an atom does not alter other parts of the electronic wave functions (i.e., perturbation in polarizability caused by small atomic displacement is localized at the atomic site); and that vibronic coupling is negligible, the SERS signals induced by $\varepsilon(\vec{r},\vec{r}_0)$ can be compactly written as follows:[82]

$$\gamma_{SERS,k} = (\nu_k + \nu_0)^4 \left| \sum_{\rho=1}^{3} \sum_{\sigma=1}^{3} \sum_{n=1}^{3N} \varepsilon_\rho(q_n) \frac{\varphi_{n,k}^L}{\sqrt{\mu_k}} \left(\frac{\partial \alpha_{\rho\sigma}^L}{\partial q_n} \right)_0 \varepsilon_\sigma(q_n) \right|^2 \cdots\cdots (3)$$

where $q_n = x_1,\ y_1,\ z_1, \cdots,\ x_N,\ y_N,\ z_N$ are the generalized Cartesian coordinates of atoms in the lab−frame, $\varepsilon_{\rho(q_n)}$ is the ρ−vector component of $\varepsilon(\vec{r},\vec{r}_0)$ at the q_n−position, $\alpha_{\rho\sigma}^L$ is the (ρ, σ) element of the molecular polarizability tensor in the lab−frame, and μ_k is the reduced mass[12] of the molecule for the k−th normal mode. The $\varphi_{n,k}^L$ is the normalized displacement of the atom at q_n associated with k−th normal mode vibration[12], which is expressed in lab Cartesian coordinates. The factors $\varphi_{n,k}^L/\sqrt{\mu_k} = \partial q_n/\partial Q_k$, are the elements of the

Jacobian transformation matrix, $\tilde{J}_k^L$, which relates the mass-scaled normal mode coordinate (Q_k) and the Cartesian coordinate of atoms (q_n). The $\left(\partial\alpha_{\rho\sigma}^L/\partial q_n\right)_0$ is an element of the Cartesian polarizability derivative tensor, $\widetilde{\alpha'^L}$. The $\tilde{J}_k^L$ and $\widetilde{\alpha'^L}$ are dependent on the molecular orientation (θ, ϕ, χ) in the labframe. I first evaluated the two quantities in a molecule-fixed frame ($\tilde{J}_k^{mol}$ and $\widetilde{\alpha'^{mol}}$) and then transformed them into $\tilde{J}_k^L$ and $\widetilde{\alpha'^L}$ via rotational transformation ($\tilde{J}_k^L = \tilde{T}^{-1}\tilde{J}_k^{mol}\tilde{T}$ and $\widetilde{\alpha'^L} = \tilde{T}^{-1}\widetilde{\alpha'^{mol}}\tilde{T}$, where $\tilde{T} = \tilde{T}(\theta,\phi,\chi)$ is the Euler rotation matrix). Eqn. 3 shows that the SERS amplitude of a k-th vibrational mode is determined by the local-field-weighted ($\varepsilon_\sigma(q_n)\varepsilon_\rho(q_n)$) sum of changes in the polarizability that are induced by the atomic displacements of the vibrational mode, $\varphi_{n,k}^L/\sqrt{\mu_k}\left(\partial_{\rho\sigma}^L/\partial q_n\right)_0$. As such, with a submolecular sized hot-spot, the SERS intensity of a vibrational peak will be highly dependent on the location of the picocavity ($\vec{r}_0$) with respect to the positions of atoms in a molecule, q_n. For the simulation of SERS spectra, molecular geometries, vibrational frequencies, Raman tensors, and Jacobian matrices for the geometry-optimized Ag-BPDT-Au complex were calculated by the DFT with the B3LYP (Becke, three-parameter, Lee-Yang-Parr) exchange-correlation functional. The molecular parameters obtained from DFT calculations and various configuration of $\varepsilon(\vec{r},\vec{r}_0)$ were

combined to model the spectra.

Fig. 13 compares the blinking Stokes SERS spectra and model spectra calculated with various positions and sizes of picocavities. The staggered-BPDT conformation with a dihedral angle between two phenyl rings of 36° was used for all the calculations shown. Fig. 13a shows the simulated density plot (gray distribution in the logarithmic color scale) of the peak intensity of the 1275 cm^{-1} mode drawn as a function of the picocavity (a diameter of 3.5 Å) position. The spatial variation of intensity ratio for the 1275 cm^{-1} peak versus the second strongest peak in the spectrum is shown in the colored contours. For this particular mode, both the peak intensity and the peak ratio distributions are highly confined around two C atoms (the two black spheres in Fig. 13a) connecting two phenyl rings. With the picocavity located close to one of the C atoms (marked as a red-cross in Fig. 13a; the distance between C atom and picocavity center is 2 Å), the model (Fig. 13c, spectrum in red) successfully reproduces the experimental spectrum (Fig. 13b). As I move the picocavity away from the optimal position (see green and black crosses in Fig. 13a and the spectra in the corresponding color in Fig. 13c), both the SERS intensity and the peak ratio rapidly decrease, which results in spectra that significantly differ from the experiment. Fig. 13d-g displays the results of the calculations with picocavity

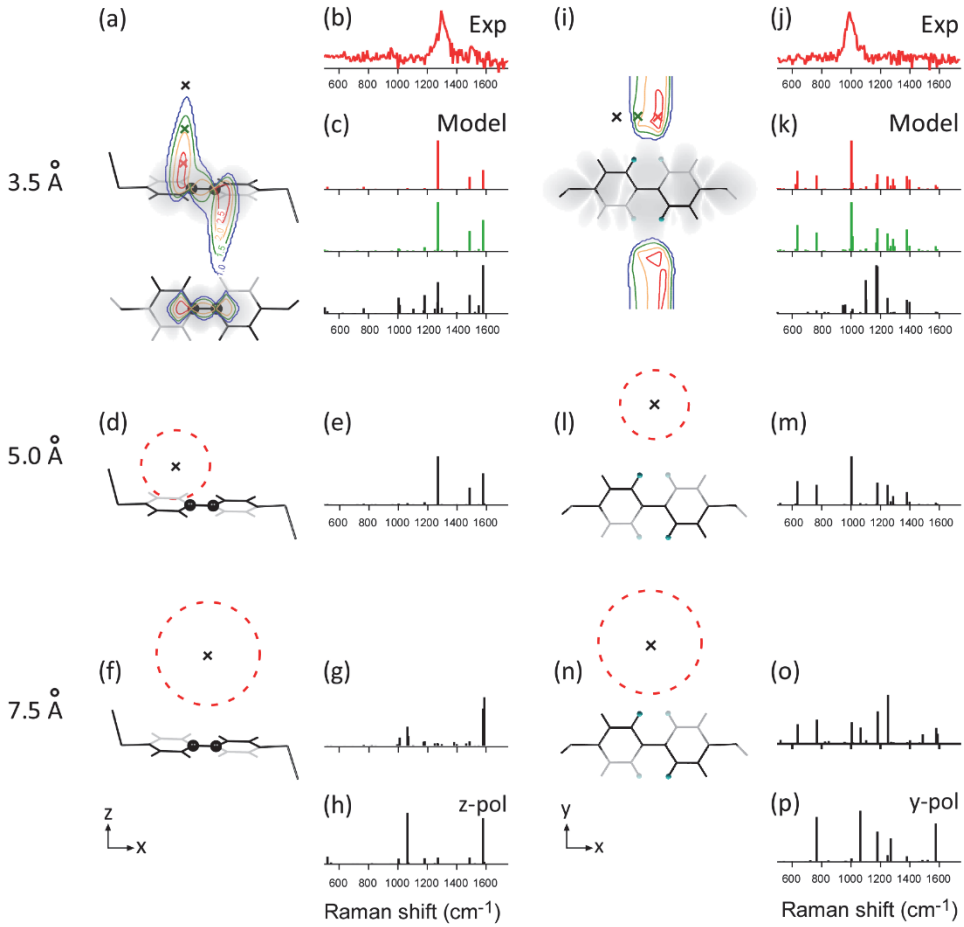

Fig. 13. Picocavity sizes and positions leading to single-peak SERS spectra. (a) Simulated peak intensity distribution (density map in gray; the shading is in logarithmic scale) and peak ratio distribution (contour plot) for the vibrational mode at 1275 cm^{-1} plotted as a function of picocavity center-position. The diameter of the picocavity used is 3.5 Å. The peak ratio is defined as the intensity of the 1275 cm^{-1} peak divided by the intensity of the second largest peak in the simulated spectrum for a given picocavity position. Distributions shown in the top and bottom panels are the xz- and xy-plane cuts of the same three-dimensional distribution, respectively. (b) Experimental blinking Stokes SERS spectrum with a prominent peak at 1275 cm^{-1}. (c) Simulated spectra with the picocavity located at cross-marked positions in (a), displayed in corresponding colors. (d,e) Single-peak optimized picocavity position and model SERS spectrum, calculated with a

picocavity radius of 5 Å. (f,g) Model SERS spectrum with a 7.5 Å picocavity positioned around BPDT. For this picocavity size, there is no picocavity position leading to spectra with peak ratio >1.0. The positions and diameters of picocavity in (d)–(g) are shown as black cross–markers and dashed circles. (h) Simulated SERS spectrum for a uniform field polarized along the z–axis. In the molecular models shown in (a), (d), and (f), the two C atoms in the phenyl groups are shown as black spheres to clarify the optimal positions of picocavity. (i–p) Corresponding results for the peak at 998 cm^{-1}.

diameters of 5 and 7.5 Å. The ratio-optimized spectrum with 5 Å picocavity (spectrum in Fig. 13e) shows only a marginal resemblance to the experiment, and the simulation with 7.5 Å picocavity results in the spectra (see, for example, Fig. 13g) that are qualitatively different from the experiment, irrespective of the picocavity positions. In fact, the latter spectrum is similar to the usual Raman spectrum induced by a uniform field (Fig. 13h). Fig. 13i-p displays the results of analogous simulations for the single-peak spectrum at 998 cm^{-1} (Fig. 13j), once again confirming that only the picocavity smaller than 5 Å can satisfactorily simulate the observation.

Fig. 14 compares the single-peak Stokes spectra and the optimized model spectra (comparison of anti-Stokes SERS and model spectra, which are essentially the same as those shown in Fig. 14, is displayed in Fig. 15a). As shown in Fig. 14b,c, a majority of the single- and multipeak blinking Stokes spectra could be successfully reproduced by the above procedure. As a comparison, I have shown in Fig. 14a a representative stationary spectrum and a model spectrum of a single molecule excited by a uniform gap-field (see inset and figure caption for the orientation of BPDT with respect to field vector direction). The same sets of molecular polarizability and vibrational frequencies are used for the simulation of stationary and blinking spectra. In Fig. 14b, all of the simulated spectra were calculated for a picocavity with

a diameter of 3.5 Å (corresponding to the covalent diameters of Ag and Au atoms), except for that with a 1487 cm^{-1} peak (see below). For the single-peak spectra (spectra i-v in Fig. 14b), the simulation yielded a unique three-dimensional position (besides a few structurally equivalent molecular sites) for the picocavity in each spectrum. The positions and diameters of the red spheres in Fig. 14c for spectra i-v represent the center positions and the upper bounds of the sizes of picocavity, respectively. The upper bounds of the picocavity sizes, defined as limits above which the spectra significantly deviate from their experimental counterparts, were found to vary slightly between different vibrational modes. However, the overall conservative upper bound for picocavity size was 5 Å. This upper bound closely approaches the result of the atomistic quantum simulation of small sodium clusters[53], and the van der Waals diameters of Au and Ag atoms (3.4 Å).[85] For multipeak SERS spectra (vi and vii in Fig 13b), the sizes and positions of picocavities were not as uniquely determined as in the case of the single-peak spectra. For example, in spectrum vii in Fig. 14b, the two peaks at 1275 and 1576 cm^{-1} could be reproduced equally well with picocavity sizes of 3.5 and 10.0 Å, at two different sites (see red and green spectra in Fig. 14b and the associated picocavity configurations drawn in the corresponding colors in Fig. 14c). This shows that single- and

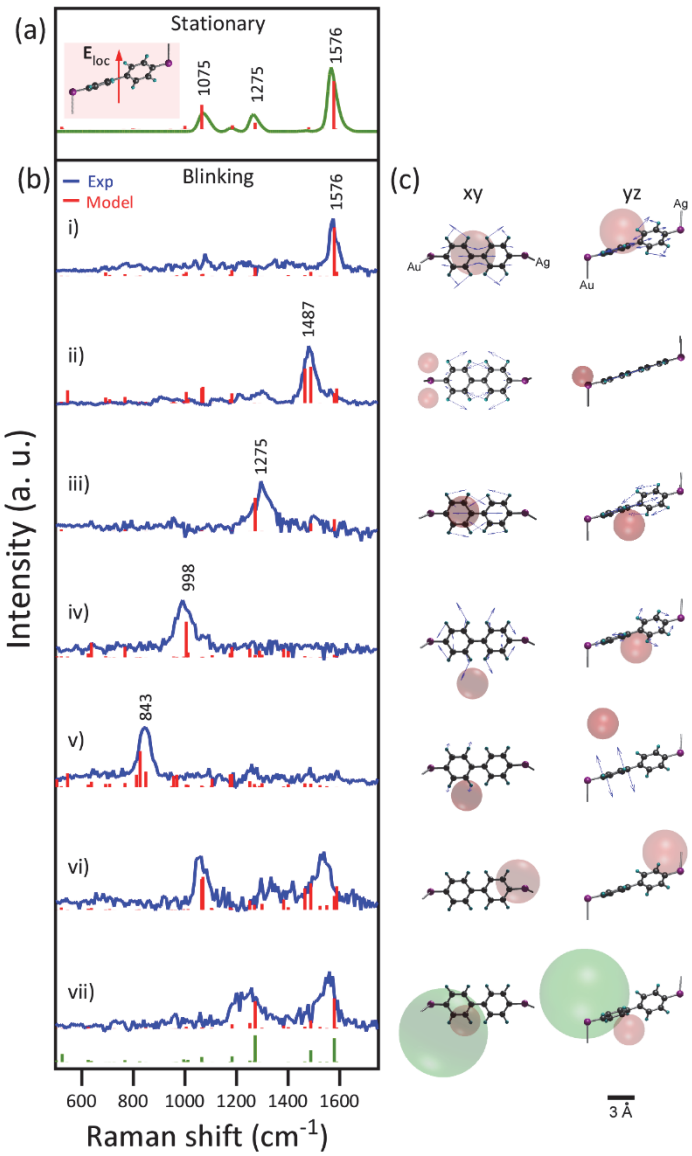

Fig. 14. Spectral fitting of blinking SERS spectra and determination of the picocavity locations. (a) Representative stationary Stokes SERS spectrum (green) and the model Raman spectrum (red) of BPDT induced by a uniform gap−field (Eloc) polarized along the z−direction. In the model, the major axis of a BPDT with a staggered conformation is tilted 72.5° from the z−axis, and one of the phenyl groups faces toward the Au surface (normal to z−axis). (b) Comparison of experimental blinking Stokes spectra (blue) and the simulation results (red). The numbers in spectra i–v show the frequencies of dominating peaks. The diameters of picocavity for the

simulations are 2.4 Å (for the spectrum with 1487 cm−1 peak (ii)) and 3.5 Å (for the rest of the spectra shown). (c) Top (xy) and side (yz) views of the locations and sizes of picocavity (red spheres) with respect to the atomic positions in a BPDT, giving rise to the corresponding simulation in (b). For i–vi, the sizes of red spheres represent the estimated upper-bounds of the picocavity size. For (vii), the spheres in red and green refer to the two possible configurations of picocavities (sizes and positions) providing a comparable fit to the experimental spectrum. Scale bar in the bottom of (c) refers to 3 Å

multipeak SERS spectra arise from the same origin, but the former can be fitted with a limited range of parameters, which results in an unambiguous determination of the picocavity dimensions and positions.

3.7. Further discussion

3.7.1. The origin of marginal difference between experiment and model

Despite showing good agreement with experimental data, the model underpredicts the single-peak character of some of the spectra. For example, the optimized model spectrum in Fig. 13k shows multiple minor peaks besides the major peak at 998 cm^{-1}, whereas the corresponding experiment (Fig. 13j) only exhibits one peak above the noise floor of the spectrum. Besides the trivial possibility that experimental noise may have masked these minor peaks, the deviation could also arise from the effects neglected in the model. Two of these possible effects are described next.

3.7.1.1. The contribution of hot-band transition

Under such highly efficient SERS condition, hot-band Stokes and anti-Stokes transitions (such as v_i = 1→2, 2→3 (Stokes), 2→1, 3→2, …(anti-Stokes)) can also contribute to the SERS signals (see Fig.

15). Thus, the experimental spectra could contain contributions of hot−band Stokes (ν_k = 1 → 2, 2 → 3,...) and anti−Stokes (ν_k = 2 → 1, 3 → 2,...) transitions, which would be spectrally unresolved from the peaks of fundamental transitions (ν_k = 0 → 1 and 1 → 0) population in vibrationally excited states. On the basis of a rate−law model, I show that hot−band−unresolved Stokes intensities follow the formula $\{\gamma_{SERS,k}(\gamma_{SERS,k}/\gamma_{VR,k}+1)\}$. The details are described below.

For the modeling, I neglect the IVR−process and also assume that the VR−rate is the same irrespective of vibrational quantum numbers. Under these assumptions, we setup the following steady state conditions for the rates of population−change in v_i−state:

$$\dot{n}_{\nu_i} = (\gamma_{Raman,i} + \gamma_{VR,i})n_{\nu_i+1} - (2\gamma_{Raman,i} + \gamma_{VR,i})n_{\nu_i} + \gamma_{Raman,i}n_{\nu_i-1} = 0$$

(for ν_i=1,2,3)

$$\dot{n}_{\nu_i} = (\gamma_{Raman,i} + \gamma_{VR,i})n_{\nu_i+1} - \gamma_{Raman,i}n_{\nu_i} = 0$$

(for ν_i=0)

The solution to these equations is : $n_{\nu_i} = \left(\frac{\gamma_{Raman,i}}{\gamma_{Raman,i}+\gamma_{VR,i}}\right)^{\nu_i} = \left(\frac{\sigma_i \cdot J}{\sigma_i \cdot J+\gamma_{VR,i}}\right)^{\nu_i}$

The Stokes and anti−Stokes SERS signals are then given by:

$$I_{S,i} = \Gamma_{s,i}(0 \to 1) + \Gamma_{S,i}(1 \to 2) + \Gamma_{S,i}(2 \to 3) + \cdots$$

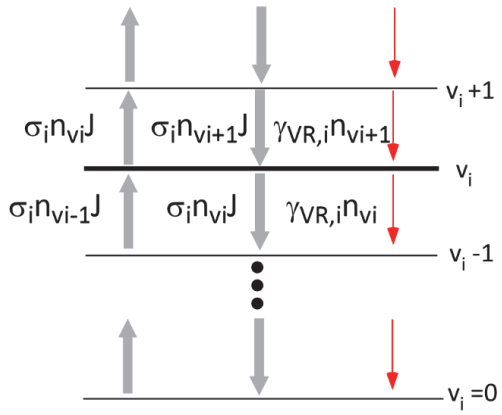

Fig. 15. Rate-process model of vibrational hot-band Stokes and anti-Stokes Raman transitions.

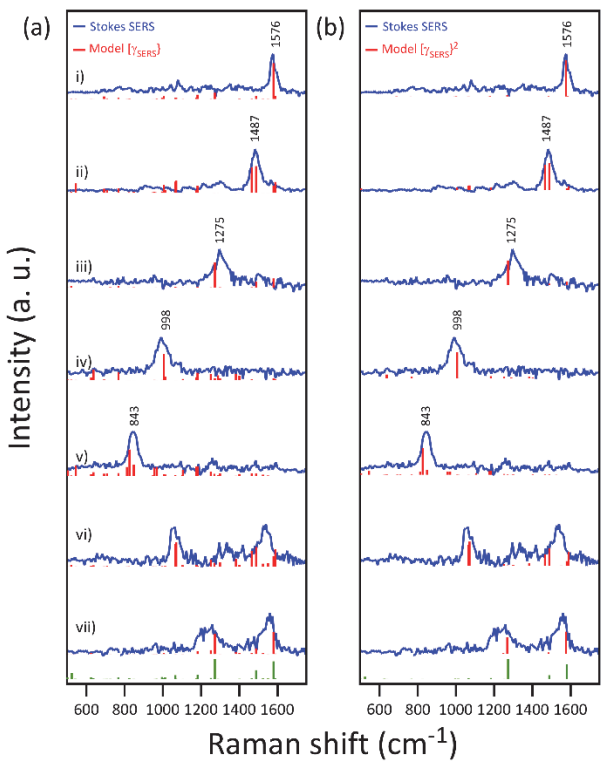

Fig. 16. Comparisons of experimental anti-Stokes SERS spectra with (a) model SERS spectra $\gamma_{SERS,i}$ and (b) with the square of the model SERS spectra $\gamma_{SERS,i}^2$. The experimental spectra shown are the anti-Stokes counterpart of the Stokes spectra shown in Fig. 14.

$$= \gamma_{Raman,i}\left(n_{i,0} + n_{i,1} + n_{i,2} + \cdots\right)$$

$$= \gamma_{Raman,i}\left(\gamma_{Raman,i}/\gamma_{VR,i} + 1\right)$$

$$= \sigma_i J\left(\sigma_i J/\gamma_{VR,i} + 1\right)$$

$$I_{aS,i} = \Gamma_{as,i}(1 \rightarrow 0) + \Gamma_{aS,i}(2 \rightarrow 1) + \Gamma_{S,i}(3 \rightarrow 2) + \cdots$$

$$= {\sigma_i}^2 J^2/\gamma_{VR,i}$$

$$= {\gamma_{Raman,i}}^2/\gamma_{VR,i}$$

The anti-Stokes versus Stokes peak intensity ratio in this case is given by:

$$\rho_i = I_{aS,i}/I_{S,i} = \gamma_{Raman,i}/\left(\gamma_{Raman,i} + \gamma_{VR,i}\right) = \sigma_i J/\left(\sigma_i J + \gamma_{VR,i}\right)$$

This is exactly the same as in the case when I consider only the fundamental Raman transition. If VR-rates do not have mode specificities ($\gamma_{VR,i} = \gamma_{VR}$), the Stokes spectral feature can vary from $\gamma_{raman,i}$ to ${\gamma_{raman,i}}^2$, depending on the ratio of $\gamma_{Raman,i}/\gamma_{VR} = \sigma_i J/\gamma_{VR}$. This ${\gamma_{SERS,k}}^2$-dependence of the SERS intensity could result in experimental spectra with more single-peak character than the model spectra (${\gamma_{SERS,k}}^2$) (see Fig. 16).

3.7.1.2. Multiple / asymmetric picocavity geometry

Second, sub-nm field distribution could have anisotropy, possibly

caused by multiple atomic protrusions or by anisotropic surface morphologies surrounding the single atom protrusion. The spectrum with a single-peak at 1487 cm^{-1} (spectrum ii in Fig. 14b) shows support for this possibility. The peak is assigned as two near-degenerate rocking deformation modes, which are Raman-forbidden; the normal mode displayed in Fig. 14c shows only one of the two modes. Intermittent activation of the peak in single-molecule SERS measurement has been previously observed and was attributed to the action of chiral local field.[48] Even with an extensive search for picocavity location and molecular conformation of BPDT, the particular spectrum could not be modeled by a single isotropic picocavity, although this is one of the most frequently observed events during the measurement. Instead, this could be modeled by placing two identical picocavities (diameters of 2.4 Å) close to an S atom of BPDT on the Au side (see the second-row graph of Fig. 14c). I have additional experimental evidence that two (or more) discrete picocavities are responsible for the single-peak at 1487 cm^{-1} : Fig. 17a,b display a SERS trajectory and two spectra showing transitions between single-peak (bottom panel of Fig. 17b) and multipeak spectra (upper panel of Fig. 17b). The transition could be reproduced by just turning one of the two picocavities on or off (see inset figures in Fig. 17b).

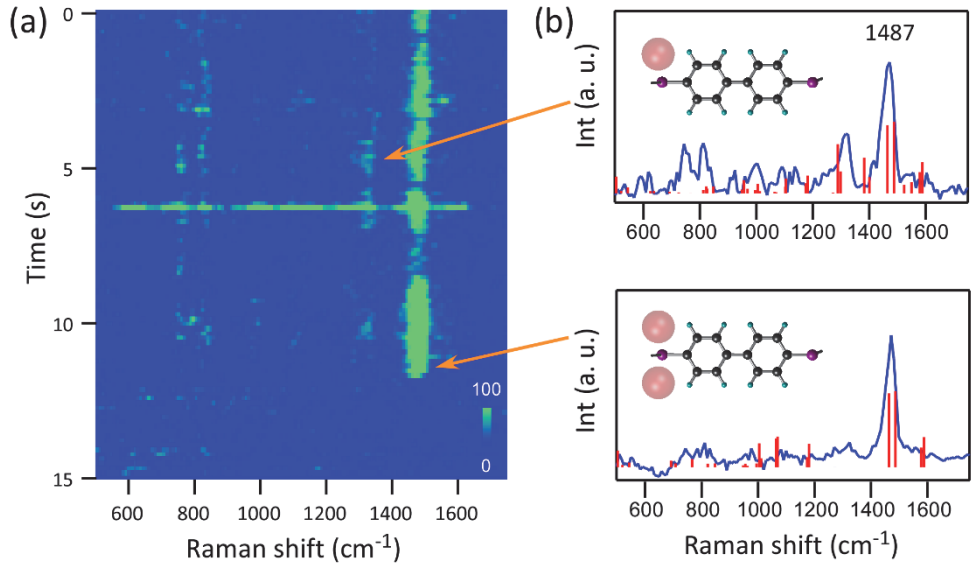

Fig. 17. Transition from single−peak to multipeak spectrum. (a) Blinking component of the anti−Stokes SERS trajectory with a prominent peak at 1487 cm^{-1}. For the particular trajectory, the anti−Stokes spectrum is displayed instead of the Stokes spectrum because the former has a better signal−to−background ratio. (b) Two SERS spectra (blue) sampled from panel (a), showing the transitions between multi−peak (top panel) and single−peak (bottom panel) spectra. Also shown are the simulated spectra (red sticks) with a single (top−panel) and double (bottom−panel) hot−spots placed close to a S atom on the Au side. For the simulation, we employed the eclipsed BPDT configuration because it offers a marginally superior spectral fitting than with staggered BPDT

3.7.2. Statistical analysis of picocavity SERS spectra

If the sources of picocavities are the structures on the surfaces of AgNP or AuTF, the positions of picocavities, on average, should stay close to the planes defined by the surfaces of Ag and Au. As such, even though the interaction of a molecule and a picocavity at a particular position does not explicitly depend on the geometry of the gap junction and the molecular orientation in the gap coordinate, a statistically averaged spectrum should reflect average molecular orientation with respect to the metallic surfaces. Here I examine if the statistically averaged blinking SERS spectrum, $\langle I_{SERS,k} \rangle$, agrees with such a scenario. The $\langle I_{SERS,k} \rangle$ is evaluated as follows: each blinking trajectory (showing single- and multipeak spectra) was normalized by the average stationary peak intensity of 1075 cm^{-1}, to remove the junction-to-junction variation in E_{loc}. The instantaneous intensity of the normalized ν_k-peak, $I_{SERS,k}(t)$, was integrated over time (t) during its on-state period ($I_{SERS,k} = \int i_{SERS,k}(t)\, dt$) and was accumulated through 25 sets of trajectories to form the $\langle I_{SERS,k} \rangle$. This averaged SERS spectrum reflects both the relative intensities of the peaks and its occurrence probability. The average anti-Stokes and Stokes spectra (Fig. 18b,c), which are nearly identical to each other, show that a significant portion of blinking events occur for the modes that are forbidden in Raman or infrared transitions (see Fig. 18a). Fig.

18d– f displays the corresponding model spectra. In the model, Ag and Au surface positions were defined at $z = z_{Ag}$ and $z = z_{Au}$, respectively. A staggered Ag–BPDT–Au complex was placed between the Ag and Au surfaces in such an orientation that the S–Au bond was aligned perpendicular to Ag and Au surfaces. The distribution in Fig. 18d was calculated from eqn. 3 for all picocavity (with a diameter of 3.5 Å) positions $\vec{r}_0 = (x_0, y_0, z_{Ag})$ in the Ag plane (z_{Ag} = constant) and was spatially averaged to give the spatially averaged peak distribution, $\langle \gamma_{SERS,k} \rangle$, for each k–th mode. Trends in the experimental average SERS spectra could be qualitatively reproduced with the model, which confirms that the picocavities were, on average, confined close to the metallic surfaces. An analogous simulation with a picocavity positioned on the Au surface (see Fig. 19) produces a qualitatively similar distribution, and thus, I cannot fully identify which of the Ag or Au surfaces generates the picocavities. The most pronounced deviation between the model (Fig. 18d) and the experiment (Fig. 18b,c) was found in the model peaks at 1075 and 1080 cm^{-1} (see the asterisk marker in Fig. 18d). I identify that these peaks primarily originate from the configurations where the picocavity is located close to the Ag–S bonding site: see Fig. 17e for the model spectrum with picocavity spatial averaging restricted to a 3 Å × 3 Å area around the Ag–S site. By excluding

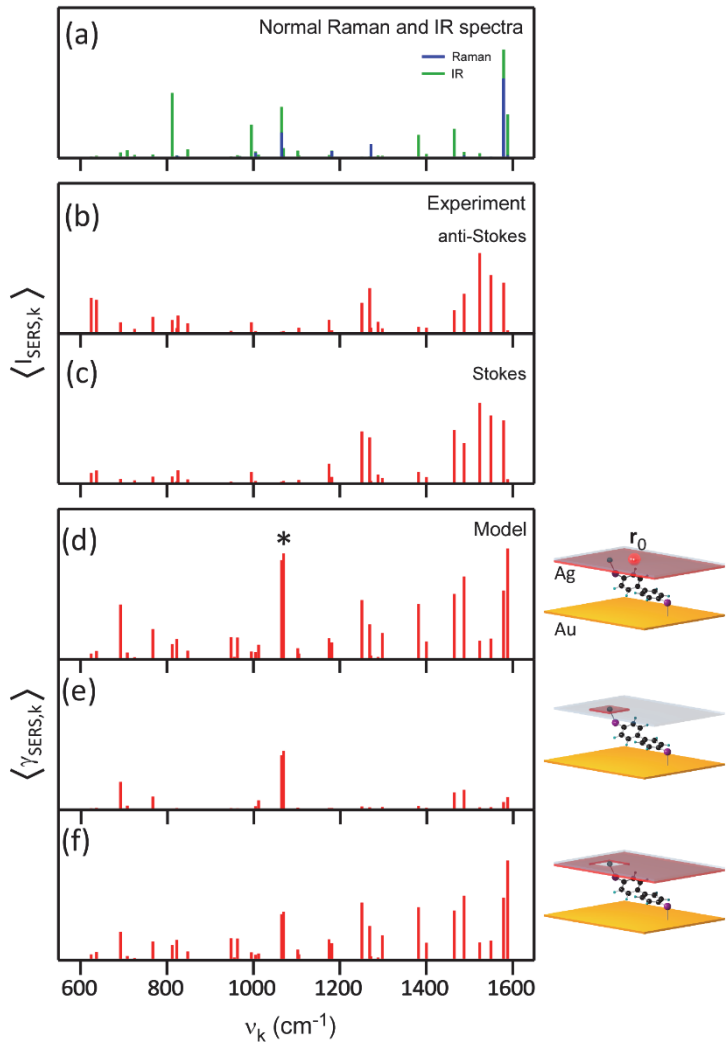

Fig. 18. Statistically averaged blinking SERS spectra. (a) Polarization-averaged infrared (IR, green) and normal Raman (blue) spectra of BPDT obtained by DFT calculation. (b,c) Statistically averaged experimental anti-Stokes and Stokes blinking SERS spectra. (d) Model SERS spectrum of BPDT that is spatially averaged over all (x_0,y_0) picocavity positions on Ag surface ($r_0 = (x_0, y_0, z_{Ag})$). The asterisk (*) points to features showing significant deviation from the experiment. (e) Model SERS spectrum averaged over picocavity positions confined in a 3 Å × 3 Å region (red-square in inset) around the S-Ag bonding site. (f) Model SERS spectrum averaged over all picocavity positions except the 3 Å × 3 Å region (void area in inset) around the S-Ag bonding site.

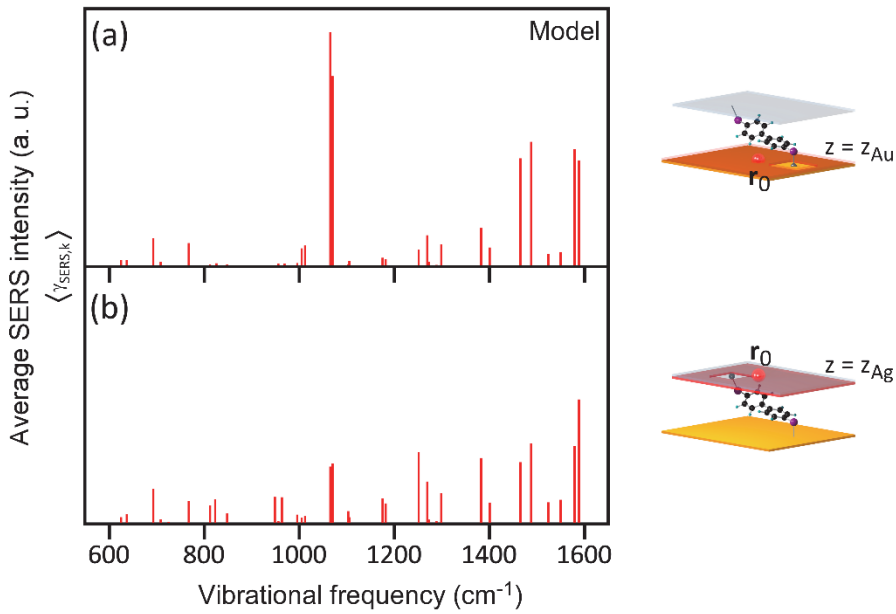

Fig. 19. Model SERS spectrum of BPDT spatially averaged over all picocavity positions. On Au−surface ($z = z_{Au}$ = constant, $r_0 = (x, y, z_{Au})$, except the 3 Å × 3 Å regions around S−Au bonding site (see inset figure). (b) Analogous spectrum with a picocavity placed on Ag−surface ($z = z_{Ag}$, $r_0 = (x, y, z_{Ag})$), except the 3 Å × 3 Å regions around S−Ag bonding site (see inset figure). In the simulation, geometry−optimized Ag−BPDT−Au complex is oriented such that Au−S bond is aligned along the z−axis (normal to the surface).

the region around the Ag–S bonding site in the spatial averaging, I obtained a spectrum (Fig. 18f) showing an improved match with the experiment. This suggests that the region around the bonding site (Ag–S) may be inactive for the creation of picocavities.

3.7.3. Possible other factors affect to picocavity

Overall agreement between our purely electromagnetic model and experiment does not completely preclude possible roles of metal–molecule vibronic interactions (via charge transfer[75] or tunneling current[86–87] driven SERS[48, 88–90]). Such vibronic effects may be manifested through the burst of continuum emission that are temporally anti–correlated to Stokes SERS peaks[48, 88–90] or through the dependency on the metal–molecule (covalent or noncovalent) contact. I do observe SERS continua in the Stokes and anti–Stokes sides of the spectra (see broad background in the on– and off–state spectra in Fig. 10c,f). However, I do not find any discernible temporal correlations of the continua to blinking or to stationary SERS peaks: for example, the on–off difference spectrum in Fig. 10c does not show any continuum background or negative Stokes peaks. Analogous SERS measurements on AgNP–biphenyl thiol (BPT)–AuTF, in which a BPT molecule forms only one S–Au bond, and on AgNP–bipyridine (BPY)–AuTF, in which a BPY molecule forms a

bridge structure through weak coordination bonding between the N atoms on the BPY and metal surfaces, also yielded anti-Stokes intensity anomalies and single-peak SERS spectra (Fig. 20) that were qualitatively similar to those obtained from the AgNP-BPDT-AuTF junctions. This indicates that the presence of S-Ag/Au links is unimportant in forming the single-peak spectra. Currently, I was unable to find any clear evidence supporting the roles of vibronic coupling.

3.8. Conclusion

To conclude, the results presented here constitute new spectroscopic evidence of the existence of picocavities on the surfaces of SERS substrates, complementing previous claims based on the resolutions of TERS imaging[55, 57-58] and vibrational pumping efficiencies.[59] Furthermore, our result provides structural details of picocavities in molecular frames, which were previously unavailable. The current results do not fully reveal the surface structures creating the picocavities, the physical origin of the blinking, and potential roles of metal-molecule vibronic interactions. Atomistic calculations[53, 91] performed on clusters suggest that principles in mesoscopic plasmonics (such as the lightning-rod effect) can be extrapolated down to a single-atom scale. On this basis, I envisage the surface

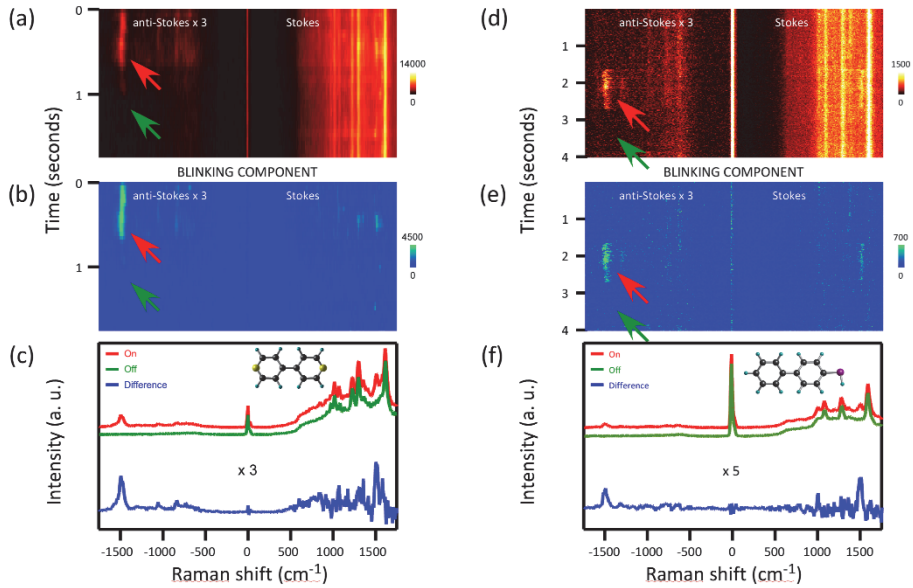

Fig. 20. Time-resolved Stokes and anti-Stokes SERS trajectories obtained from a AgNP-BPY-AuTF junction showing on (red arrow) / off (green arrow) blinking of a peak at 1500 cm^{-1} (b) Blinking component of the trajectory (a), (c) SERS spectra sampled during on and off period. Also shown in blue is the difference (on-off) spectrum of the two. (d)-(f) Another set of SERS trajectory data with AgNP-BPT-AuTF junction.

structures inducing picocavities as atomically sharp vertices or edges defined by the interfaces of crystalline facets. Their atomic-scale lateral diffusion may account for the blinking of SERS signals.

Picocavities can greatly benefit plasmon-enhanced spectroscopy, nanoscopy, and photochemistry, if I could precisely control their creation. The TERS version of the current experiment, in which picocavities precisely positioned at the tip-end, may generate peak intensity distributions containing real-space information on atomic displacements of vibrational modes. Such real-space map of vibrational modes of single-molecules could offer atomic-level pictures of intermolecular interactions between molecules. This exciting possibility has been theoretically proposed[52, 60] and the present result provides experimental feasibility. I believe that the selection rules of electronic transitions of atoms[92] and molecules, as well as those of vibrational transitions of molecules, could be drastically altered by the picocavities. Therefore, with picocavities, one may even drive unusual photochemical reactions of molecules that are otherwise forbidden by orbital symmetries of electronic excited states. With a deeper understanding of the picocavities and their interaction with molecules, such possibilities may be experimentally realized.

Chapter 4. Highly efficient and mode selective vibrational pumping by plasmon induced electrons

This chapter will be submitted

4.1. Background

Vibrational control of chemical reactions on metallic surfaces, manipulating reaction pathways by preparing the reactant in a specific vibrational state, may help understanding the reaction mechanism and also optimizing industrially important reactions such as heterogeneous catalysis. However, the vibrational energy of the newly prepared reactant is rapidly dissipated[93-95] to surfaces even before the reactions to occur (an exception is the ultrafast unimolecular reaction, in which reaction takes place in ps-fs timescale), making it hard to achieve any control. At the heart of the problem lies at the experimentally available vibrational excitation rate (k_{exc}) as compared with vibrational relaxation rate (k_{VR}). The k_{VR} of a typical organic molecule on metallic surface is 10^{12} ~10^{13} s^{-1} [80], although exceptionally slow relaxation of 10^{10} s^{-1} have been reported for weakly bound small molecules.[96]

To prepare substantial population of vibrationally excited molecules in steady state on metallic surface, one need extremely

intense light source. The power needed to prepare the population can be inferred by the eqn. 2 in chapter 3.4 and the equation is modified and re-written below.

$$J = \frac{\rho_i k_{VR}}{\sigma_i(1-\rho_i)}$$

, where J, ρ_i and σ_i are photon flux, population ratio between vibrationally excited state and ground state and excitation cross section respectively. For small organic molecule with infrared (IR) absorption cross section of 10^{-20} cm^2, one needs ~30 kW of IR laser focused by objective lens with NA of 0.33 to achieve 1 % of excited population. For molecule with Raman cross section of 10^{-30} cm^2, similarly, ~1 MW of He-Ne laser focused by objective lens with NA of 1.4 is needed by SERS pumping whose enhancement factor is 10^6. These conditions cannot be achieved in lab condition.

There have been a few claims and indirect evidences that localized plasmons, the collective oscillation of electrons of nanoparticles and the local field around it, may efficiently transfer vibrational energy to the molecule. For example, Christopher and co-workers proposed that attachment and subsequent detachment[97] of plasmon-induced hot electrons[16] (which is done generated by a few mWs of CW laser light) to weakly bound gas phase O_2 near the NP may lead to the

steady state vibrational excitation in O_2, leading an efficient epoxidation of ethylene.[98-99] Validity of this scenario, again, critically relies on the premise that the k_{exc} of electron collision is comparable to k_{VR}, which, to date, has not been directly confirmed. Apkarian and his co-workers recently observe population inverted vibrational distribution of molecules placed at the gap of plasmon excited dimeric nanoparticles, which strongly suggest the action of tunneling electrons of charge transfer plasmon (CTP) mode.[100] However, they still used picosecond laser whose pulse width is comparable to the lifetime of vibrationally excited state.

Here I show an unusual observation that molecules placed in a metallic gap, when resonantly excited with a few mWs of CW, visible light, generates a substantial vibrational pumping of a specific normal mode. The 4-nitrobenzenethiol (NBT) adsorbed at the narrow gap between Ag-nanoparticle (AgNP) and Au-thin film (AuTF), when illuminated with a visible light, undergoes plasmon-induced 6-electron reduction to form 4-aminobenzenethiol (ABT).[11] Time-resolved SERS spectra of the NBT shows an intense ν_s(NO) (symmetric NO stretching of NO_2 group) anti-Stokes (aS) peak, which persists during the entire course of the reaction. Not only does the effective vibrational temperature of ν_s(NO) peak is extremely high (> 500 K), but it is the only Raman-active mode of NBT

exhibiting such unusual excitation. These, together with temporal profile of aS peaks, laser power dependence, chemical specificities, and model calculation strongly suggest that the excitation arises from the resonant scattering of plasmon-induced electrons (either the hot electrons ejected from the metallic surfaces or the electrons tunneling through the gap) and NBT. The result constitutes the first example where vibrational excitation rate far exceeds its relaxation rate, generating non-equilibrium (unrelaxed) vibrational population at a few seconds of time scale. This also opens up new possibility for vibrationally controlling the chemistry on metallic surfaces.

.

4.2. Experimental method

A fully saturated self-assembled monolayer of 4-nitrobenzenethiol (NBT, Tokyo Chemical Industry) was formed on top of a Au thin-film (TF; Au thin film with a thickness of 10 nm formed on top of a Ti adhesion layer of 2 nm) formed on a glass substrate. The Ag nanoparticles (AgNPs, diameters of 80 nm, BBI co., Ltd and Nanocomposix) were dispersed on top of the NBT / AuTF surface to form AgNP-NBT-AuTF junctions.

The SERS signals were measured with a homebuilt epi-confocal microscope equipped with a high-NA objective lens (1.4 NA, oil-immersion type, U Plan S-Apo, Olympus co.), a Raman spectrometer

(Shamrock 500i, Andor Technology Ltd; EM-CCD, iXon3 897, Andor Tech), a piezo-scanner (P-517, Physik Instrumente), diode lasers (λ_{ex} = 473 nm, 532 nm and 808 nm) and a HeNe laser (λ_{ex} = 633 nm, Melles Griot) as the excitation light source. SERS trajectories were obtained by placing the laser focus onto a single AuNP-NBT-AuTF junction and recording the SERS spectra as a function of time (> 20 ms exposure time/spectrum). A Raman notch filter was placed in front of the spectrometer to filter out both the Rayleigh scattering and low frequency vibrational peaks (< 500 cm^{-1}) of NBT.

4.3. Calculation method

The optimized geometry and the information of vibrational modes such as frequencies, reduced mass, vibrational motion are obtained by *CASSCF* calculations using Molpro 2012 package (H.-J. Werner and P. J. Knowles). The calculation is conducted by Yeonsig Nam and Jin Yong Lee at SKKU.

4.4. Experimental result

The plasmonic gap structure (Fig. 21a), which defines reaction and detection zones, is composed of AgNPs (diameter of 80 nm) placed on a monolayer of NBTs that are self-assembled on a AuTF

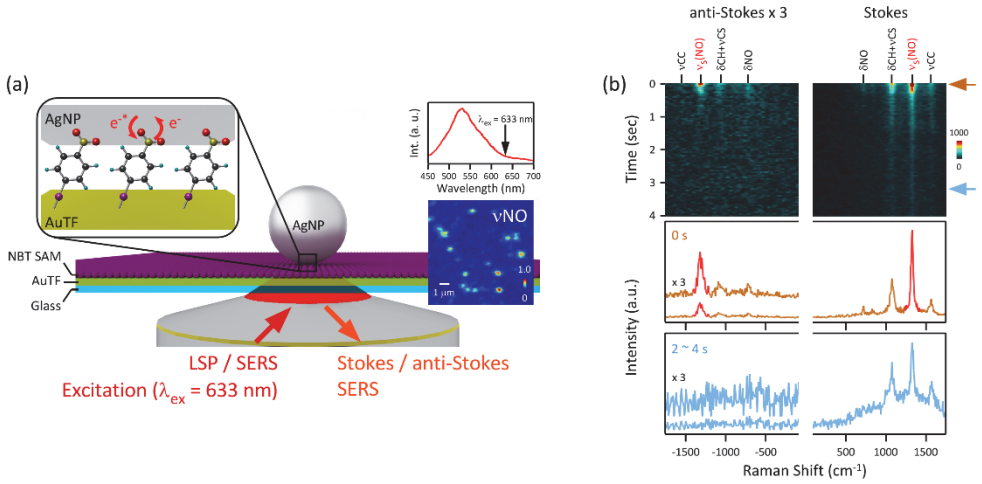

Fig. 21. Experimental scheme and SERS analysis of vibrational pumping. (a) The structure of AgNP−NBT−AuTF junction. The insets are magnified gap−junction structure with scheme of inelastic scattering of plasmon−induced electrons, dark−field spectrum of the junction and SERS image of ν_S(NO). He−Ne laser with wavelength of 633 nm which resonates with BDP mode of the junction is used for LSP and SERS excitation (b) Time−resolved SERS spectra of AgNP−NBT−AuTF junction (top−panel) and their cross section spectra sampled from initial stage of photo−reduction (t = 0 s, brown) and after the completion of it (t= 2~4 s, sky−blue). Anti−Stokes side is magnified 10 times in time−resolved spectra to show peaks clearly. The red mark peaks in middle panel are anti−Stokes and Stokes peak of ν_S(NO).

(thickness of 10 nm). A focused laser beam at λ_{ex} = 633 nm, resonating with the bonding dipolar plasmon (BDP) mode of the junction (see inset scattering spectrum in Fig. 21a), locally drives the reduction of NBT to yield ABT. The same laser also excites the SERS of the NBT and product, and a spectrometer records the Stokes (S) and anti-Stokes (aS) components of SERS spectra in real-time. As shown in SERS confocal image (inset of Fig. 21a), such structures exhibit strong field enhancement (enhancement factor of ~10^{7} [11]) leading to the enhanced Raman signals (bright spots in the image) primarily at the AgNP / NBT / AuTF junction sites.

Fig. 21b displays a representative time-resolved Stokes and anti-Stokes SERS spectrum (top panel) obtained from a AgNP-NBT-AuTF junction recorded during the reaction, and two SERS spectra (bottom panel) sampled at t = 0 seconds (brown), and during t = 2 - 4 seconds (sky blue). Initial Stokes spectrum shows four major peaks of NBT of NO_2 bending (δNO, 739 cm^{-1}), aromatic C-H bending coupled to C-S stretching (δCH+νCS, 1082 cm^{-1}), symmetric N-O stretching of NO_2 (ν_s(NO), 1329 cm^{-1}, and aromatic C-C stretching (νCC,1579 cm^{-1}). Gradually disappearing ν_s(NO) intensity corresponds to the conversion of NBT to ABT. In the early stage of the reaction, corresponding anti-Stokes spectrum shows intense ν_S(NO) peak (t = 0 sec, see also bottom panel of Fig. 21b)

and gradually decays. In this stage, the anti−Stokes of ν_S(NO) is stronger than that corresponding to thermal equilibrium and such hyperthermal anti−Stokes disappear after the completion of reduction (t = 2− 4 sec, see also bottom panel of Fig. 21b).

Fig. 22a displays the plots of the anti−Stokes / Stokes intensity ratios for each peak ($\rho_i = I_{aS,i}/I_{S,i}$, where $I_{aS,i}$ and $I_{S,i}$ are anti−Stokes and Stokes peak of i' th vibrational mode) plotted as a function of vibrational frequency (ν_i), sampled from initial and final stage of the trajectory shown in Fig. 21b. Also shown as a comparisons (gray curves) are the theoretical ρ_i s for a fully thermalized NBT at room temperature (T = 310 K) and T = 735 K:[14, 100]

$$\rho_i = A \cdot \left(\frac{\nu_0 + \nu_i}{\nu_0 - \nu_i}\right)^3 \cdot exp\left(-\frac{h\nu_i}{k_B T}\right) \cdots\cdots (4)$$

, where ν_0, ν_i, and k_B are the laser excitation frequency, vibrational frequency of the molecule and Boltzmann constant. The A factor (for this particular graph, I set A = 7.7) is a correction factor for a possible wavelength dependent spectrometer response and asymmetric plasmon resonance bias at each junction.[14, 101] The A is determined assuming that the temperatures of vibrational modes are thermalized to room temperature after completion of photo−

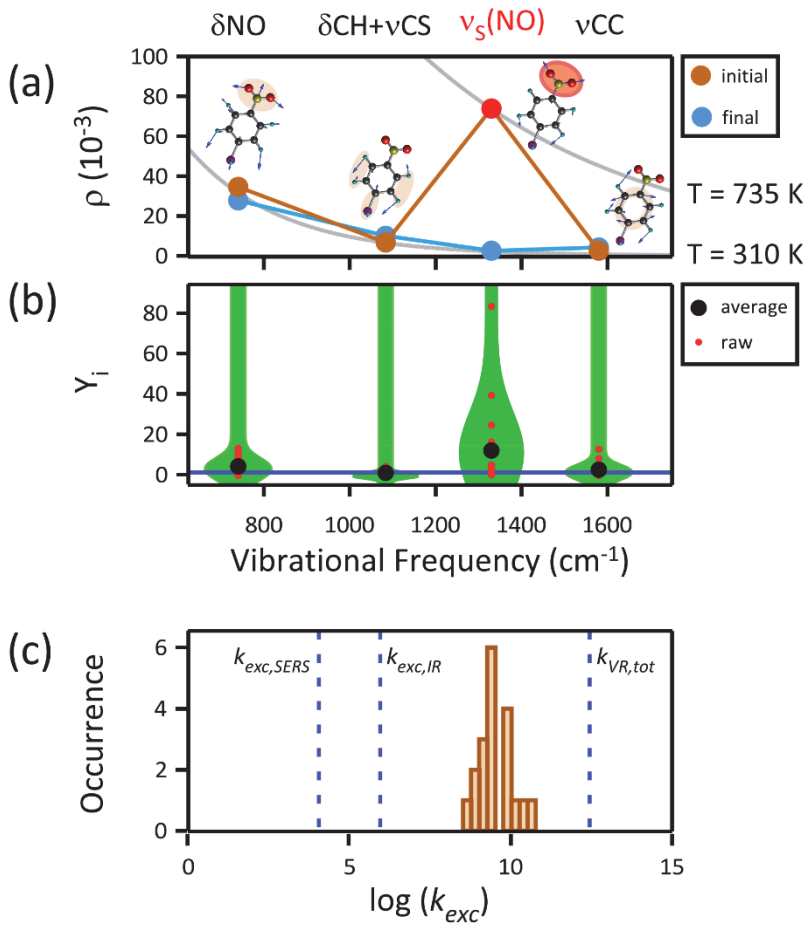

Fig. 22. The degree of vibrational pumping (a) The ρ_i values of Raman-active modes plotted as a function of vibrational frequency after the correction of biases such as plasmonic asymmetry. Brown circles and red circle for ν_S(NO) are ρ_is obtained from SERS spectrum of t = 0 s in Fig. 20b. Sky-blue circles are ρ_is obtained from SERS spectrum of t = 2 – 4 s in Fig. 21b. Gray curves represent Boltzmann distribution of 735 K and 310 K. The insets are the vibrational motion of Raman-active modes and colored shades are localized position of each vibrational mode. (b) Y_i values which is ratio between $\rho_i\,(initial)$ and $\rho_i\,(final)$. The blue line is Y_i = 0 which is excitation which means the absence of nonthermal pumping at the initial stage of photo reduction. Green violin plot is laid gaussian curve which represented by averaged Y_i and its standard deviation. (c) Excitation rate (k_{exc}) obtained from Y_i of ν_S(NO).

reduction. The final state ρ_i monotonically decrease as a function of frequency, and can be satisfactorily fitted to the eqn. 4 with a near room temperature (gray curve corresponding to T = 310 K), indicating that the molecules are fully thermalized. On the other hand, the initial state ρ_i does not monotonically decrease nor can be fitted to a thermalized distribution at a single temperature. Most striking deviation arises from ρ_i for ν_S(NO), with an effective temperature of 735 K, whereas the three other modes remain thermalized at T = 310 K.

I observe a wide junction-to-junction variation in SERS signal intensities and ρ_i, which arises from the variations in local field intensities and plasmon resonance spectra of the AgNP-AuTF junction[14, 79]. However, this highly nonthermal vibrational population for ν_S(NO) is consistently observed in most (> 90 %) of the junctions I have examined. To further examine possible systematic errors in the measurement (possibly by the asymmetry factor, A), I have evaluated the ratios of ρ_i (initial) and ρ_i (final) obtained from the same trajectory:

$$Y_i = \frac{\rho_i(initial)}{\rho_i(final)} - 1 = \frac{n_{initial,i} - n_{final,i}}{n_{final,i}}$$

This quantity describes the enhanced excited state vibrational

population for each mode as compared with that of fully thermalized final state. This ratiometric quantity also removes possible systematic error induced by resonance bias (A factor), and thermal contribution to the vibrationally excited state. Fig. 22b shows the scatter plot of Y_i accumulated from 19 different SERS trajectories. In the figure, red circles are Y_is evaluated from SERS trajectories and black circles are average of Y_is of each vibrational mode. The plot not only shows significant vibrational pumping of ν_S(NO) mode during the reaction, but it also shows large junction-to-junction variation on the degree of vibrational excitation. As I show below, this variation in ν_S(NO) mostly arises from the variation in local field intensity for each junction.

Fig. 23a shows the correlation plots of (I_S (νCC), I_{aS} (ν_S(NO))) and (I_S (νCC), I_{aS}(δCH)) obtained from 19 different junction positions excited with 3 different laser powers. Here, the I_S (νCC) serves as a measure of local field intensity ($|E_{loc}|^2$) at each junction. Both correlations show clear quadratic dependences on $|E_{loc}|^2$ even though the increasing rate of anti-Stokes for ν_S(NO) exceeds far from that for δCH. This clearly indicates that plasmon driven one photon in pumping result in vibrational excitation, and the observed variation Y(ν_S(NO)) excitation mostly arises from junction-to-junction

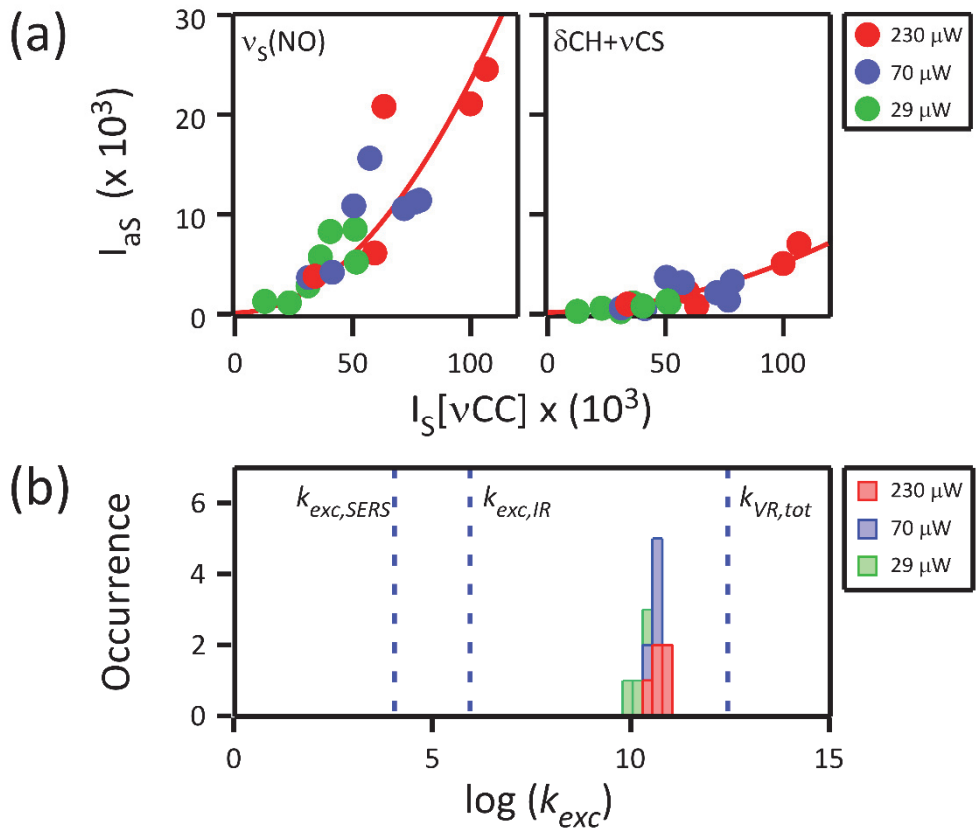

Fig. 23. (a) Local field dependence of anti-Stokes of ν_S(NO) and δCH. Both modes show quadratic local field dependence. The anti-Stokes intensity of ν_S(NO) shows faster increase rate than that of δCH. (b) Excitation rate (k_{exc}) obtained from local field dependence of ν_S(NO)

variation in intensity.

Based on the Y_i values and local field dependence of $I_{aS}(\nu_S(NO))$, I estimated how fast pumping may occur via electron scattering process. From my definition of Y_i, first, I inferred k_{exc} of $\nu_S(NO)$ using as below.

$$Y_i = \frac{\tau_{VR}\sigma_{exc}I_L/\hbar\omega_L + \exp(-hc\tilde{\nu}_i/k_BT)}{\exp(-hc\tilde{\nu}_i/k_BT)} - 1 = \frac{k_{exc}/k_{VR}}{\exp(-hc\tilde{\nu}_i/k_BT)}$$

$$k_{exc} = k_{VR}Y_i\exp(-hc\tilde{\nu}_i/k_BT) \cdots\cdots (5)$$

, where τ_{VR}, σ_{exc}, I_L are lifetime of vibraionally excited $\nu_S(NO)$, excitation cross section and photon flux. I used 2.86×10^{11} s^{-1} for k_{VR} of $\nu_S(NO)$ of NBT following Frontiera et al.[4] Assuming the temperature as 300 K, k_{exc} reaches to 10^{10} ~ 10^{12} s^{-1} which is comparable to k_{VR} (see Fig. 22c). Also, eqn. 5 reveals that the k_{exc} inferred from Y_i is lower boundary of the rate because the k_{exc} is proportional to temperature. That is, k_{exc} may exceed the 10^{10} s^{-1} if the sample is heated to the temperature above room temperature. Second, the value of k_{exc} is inferred by the $|E_{loc}|^2$ dependence trajectory of I_{aS}. The dependence is described by equation below.

$$I_{aS} = A \cdot \tau_{VR}\sigma_{exc,i}{I_L}^2/hc\tilde{\nu}_i + A \cdot \exp(-hc\tilde{\nu}_i/k_BT) \cdot I_L \cdots\cdots (6)$$

, where A is bias mainly risen from plasmon asymmetry. The eqn. 6 is simplified substituting the $A \cdot \tau_{VR}\sigma_{exc,i}/hc\tilde{\nu}_i$ and $A \cdot \exp(-hc\tilde{\nu}_i/k_BT)$ as C_1 and C_2 respectively. The simplified equation is described below.

$$I_{aS} = C_1 {I_L}^2 + C_2 I_L$$

k_{exc} is extracted from the ratio between C_1 and C_2

$$\frac{C_1 I_L}{C_2} = \frac{\tau_{VR}\sigma_i I_L/hc\tilde{\nu}_i}{\exp(-hc\tilde{\nu}_i/k_BT)} = \frac{k_{exc}/k_{VR}}{\exp(-hc\tilde{\nu}_i/k_BT)}$$

$$k_{exc} = k_{VR}\exp(-hc\tilde{\nu}_i/k_BT)\frac{C_1 I_L}{C_2}$$

k_{exc} extracted from the $|E_{loc}|^2$ dependence of $I_{aS}(\nu_S(NO))$ is closed to that obtained from Y_i (see Fig. 23b).

Another notable observation (Fig. 24) for ν_s(NO) mode is that Stokes trajectories of ν_s(NO) show both the non-reactive (near-constant or extremely slow variation) as well as the reactive (decaying) components, whereas the corresponding anti-Stokes trajectories show only the reactive components. As shown by Choi et al., ν_S(NO) Stokes peak contains contributions from anion radical of NBT ($NBT^{\cdot -}$) as well as neutral NBT.[102] In particular, nearly all of the neutral NBT molecules are converted to NBT^- within a few

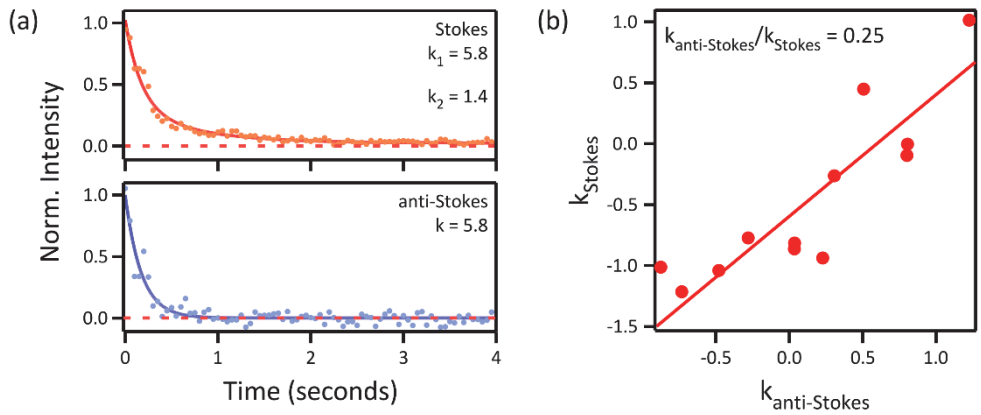

Fig. 24. Time trajectory analysis of anti-Stokes and Stokes SERS of ν_S(NO). (a) The time trajectory of Stokes (top panel, brown circles) and anti-Stokes (bottom panel, sky-blue circles). The anti-Stokes and Stokes trajectories are fitted to double exponential (brown sold line) and single exponential function (sky-blue solid line) respectively. The one of time constant ($k_{anti-Stokes}$) is coincide with that of anti-Stokes. There is marginal offset of Stokes trajectory at the t > 2, on the other hand, anti-Stokes trajectory converges to intensity of zero (t > 0.7). (b) Correlation between time constant of Stokes trajectory which is not coincide with that of anti-Stokes and time constant of anti-Stokes trajectory. The time constant of Stokes increases linearly respect to that of anti-Stokes with slope of 0.25. The slope represent the ratio between $k_{anti-Stokes}$ and k_{Stokes} which is similar to that of NBT and NBT^-.

seconds. As such, I argue that initial anti-Stokes and Stokes ν_S(NO) peak mostly represent neutral NBT. Whereas, the final state mostly represent the spectrum of NBT^-. The Stokes ν_S(NO) which is composed of reactive and non-reactive component is fitted to double exponential function. The ratio between the rate constants of Stokes ν_S(NO) is around 4:1, which coincides with the ratio of the decay constants for the NBT and NBT^-, and the rate constant of anti-Stoke ν_S(NO) corresponds to larger one of Stokes (see Fig. 24 b).[102] In this regard, this shows that only the neutral NBT is vibrationally excited component and contributes to super intense anti-Stokes. Additionally, this temporal difference, together with the quadratic $|E_{loc}|^2$-dependence of Y(ν_S(NO)), preclude the possibility that the observed anomaly in anti-Stokes ν_s(NO) peak may originate from systematic measurement errors which are time-invariant.

Finally, I observed wavelength dependence of the pumping rate of ν_S(NO) (Fig. 25a) and mode selectivity of Y_i at various excitation wavelength (Fig. 25b). For this measurement, CW pump laser with various wavelengths (λ_{pump} = 473, 532, 633 nm) and CW probe laser (λ_{probe} = 633 nm) are used to induce LSP excitation and SERS measurement. For 532 nm and 633 nm excitations which are closed to resonance of BDP mode, averaged Y_i and the variation of it show mode selectivity to ν_S(NO) (see Fig. 25c, d). On the other hand, any

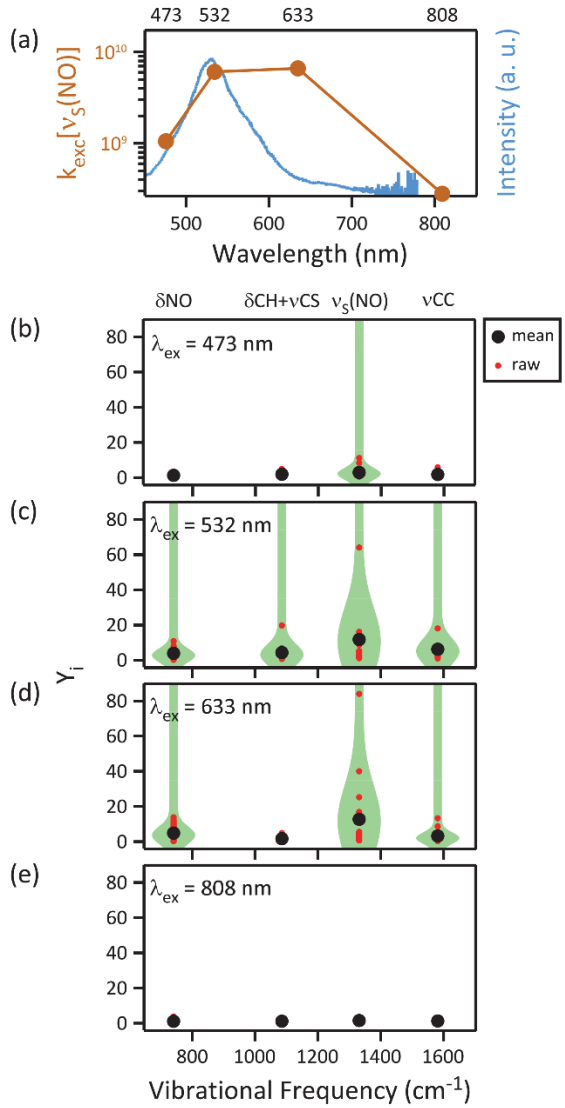

Fig. 25. Wavelength dependence of Y_i of each mode and pumping rate of ν_S(NO) ($k_{exc}(\nu_S(NO))$). (a) Dark-field spectrum obtained from AgNP-NBT-AuTF junction (sky-blue) and the action spectrum of $k_{exc}(\nu_S(NO))$ obtained from averaged Y(ν_S(NO)). The wavelength dependence of k_{exc} are plotted in logarithmic scale (b-e) The action spectra of Y_i obtained from various λ_{pump} of 473, 532, 633, 808 nm. Red circles are Y_i values obtained by SERS measurements and the black circles are averaged Y_i from red circles. Green violin plot is laid gaussian curve which represents the average and standard deviation of Y_i.

noticeable vibrational pumping is not shown under excitation wavelength of 473 and 808 nm. Additionally, the wavelength dependence of $k_{exc}(\nu_S(NO))$ is calculated from the averaged $Y(\nu_S(NO))$ obtained from various excitation wavelengths (see eqn. 5). The action spectra of $k_{exc}(\nu_S(NO))$ and the dark-field spectrum obtained from a AgNP-NBT- AuTF junction are shown in Fig. 25a. I found that $k_{exc}(\nu_S(NO))$ approximately follows the BDP resonance curve, and it does not show any $\nu_S(NO)$ excitation for λ_{pump} larger than 750 nm.

4.5. Modelling vibrational pumping by inelastic resonant electron scattering

4.5.1. The possibility of picocavity SERS

To maintain the nonthermally excited population in steady state, the excitation rate should be comparable to that of VR whose rate is 10^{12} s^{-1}.[15] This rate cannot be achieved through a SERS pumping with a usual gap field as described in chapter 4.1. As recently demonstrated (also in chapter 3), angstrom-sized electromagnetic hotspots (picocavity) on metallic surfaces can offer exceptionally enhanced Raman transition rates sufficient to compete with k_{VR}, leading to unusually intense anti-Stokes SERS peaks.[59, 103-104] Although the

experimental settings are similar, the anti-Stokes signals I observe have distinctly different features: First, while the picocavity SERS signals show temporally stochastic step structures, my data shows fairly reproducible anti-Stokes trajectories that are temporally correlated with the course of photo-reaction. Second, the picocavity SERS spectra show a wide junction-to-junction variation in selection rule, and the selected peaks often show dipole-forbidden transitions. However, my spectra show exclusive excitation of dipole-allowed Raman transition of ν_S(NO)-peak. Third, the picocavity SERS is observed irrespective of molecular structures, showing that the effect is purely electromagnetic in origin. Finally, the emergence of anti-Stokes peaks of picocavity SERS is accompanied by the corresponding Stokes Raman peaks, showing that it is the Raman scattering process that is causing the pumping. In my case, (1) I do not see any sign of extra enhancement in Stokes peak of ν_S(NO) indicating that the excitation is unrelated to the Raman scattering process and (2) mode selective anti-Stokes excitation is observed only for a specific molecule such as NBT. As a comparison, I have carried out analogous measurements on various para-substituted aromatic thiols, including 4-methylbenzenethiol (MBT), 4-mercaptobenzonitrile (MBN), and 4-mercaptobenzoic acid (MBA). If the vibrational pumping of ν_S(NO) is occurred by

picocavity (Fig. 27), all para-substituted aromatic thiols should undergo similar pumping of vibrational mode localized to substituent group. Unlike to NBT, however, SERS spectra of molecules do not show such highly reproducible vibrational pumping. The time-resolved SERS spectra of AgNP-MBN-AuTF is shown in Fig. 26 as a representative of the para-substituted aromatic thiols. As mentioned above, there is no noticeable vibrational pumping in the trajectory. On the other hand, the simulated picocavity SERS spectra with various relative picocavity positions to MBN show single νCN peak as shown in Fig. 28 These indicates that the pumping is closely related to the nature of the molecules, not to the properties of metals.

4.5.2. Vibrational pumping by inelastic resonant electron scattering

I have reasons to believe that this unusual pumping arises from resonant scattering of electrons and NBT, where the electrons are either the oscillating electrons of plasmons (including the electrons tunneling through the gap) or hot electrons generated by the decay of plasmons. First, the unusual vibrational pumping is temporally correlated with the kinetics of plasmon-assisted reduction (i. e., metal-molecule charge transfer) of NBT[11], suggesting that the vibrational pumping and the reaction may have the common origin. scattering resonance[105-106] with electron beams at the kinetic energy

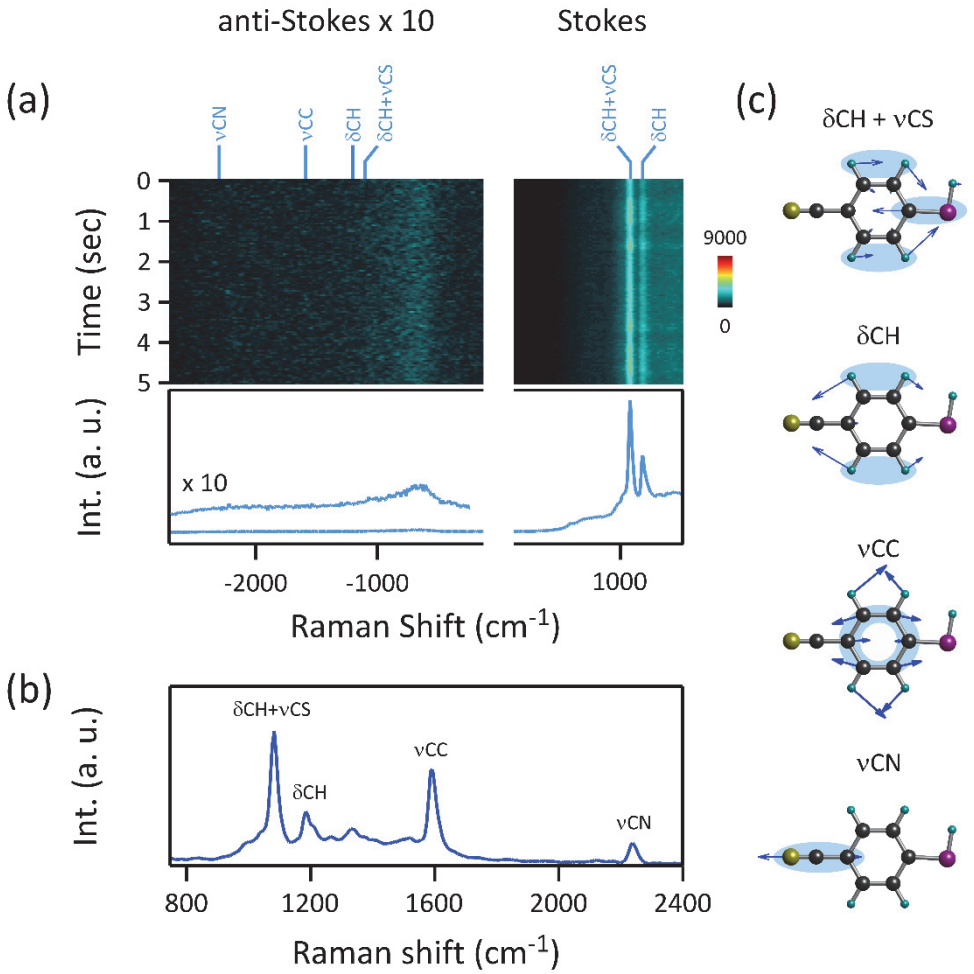

Fig. 26. SERS spectrum of AgNP−MBN−AuTF junction. (a) Time−resolved SERS spectra of AgNP−MBN−AuTF junction of anti−Stokes side and averaged spectrum obtained from the trajectory. The anti−Stokes side is magnified 10 times. Only stationary components are shown in Stokes side and there is no noticeable peak on anti−Stokes side. (b) The Stokes SERS of AgNP−MBN−AuTF as a comparison. (c) The vibrational motion of Raman−active mode of MBN, Only νCN mode is localized to para−substituted group.

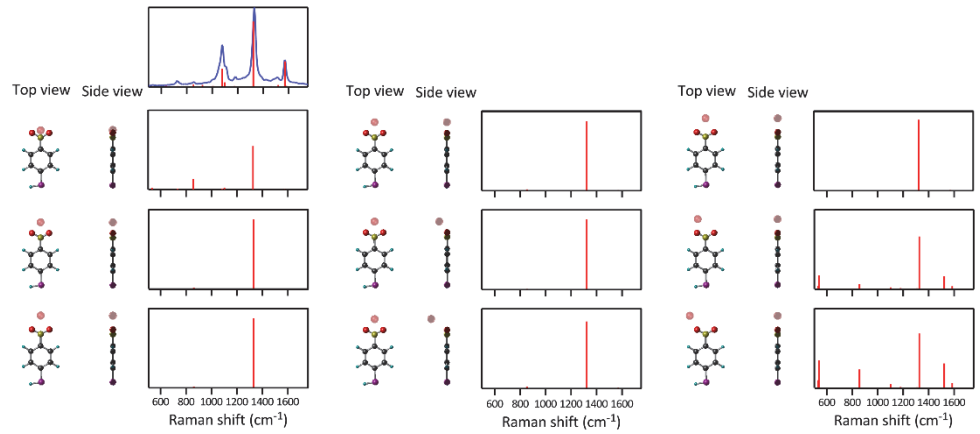

Fig. 27. The simulated picocavity SERS spectra and the relative position of picocavity (red sphere) to NBT. As a comparison, top panel of left column shows SERS spectrum obtained at AgNP−NBT−AuTF junction (blue) and simulated spectrum by DFT. Except for middle and bottom spectra in right column, single ν_S(NO) peak picocavity SERS spectra are reproduced.

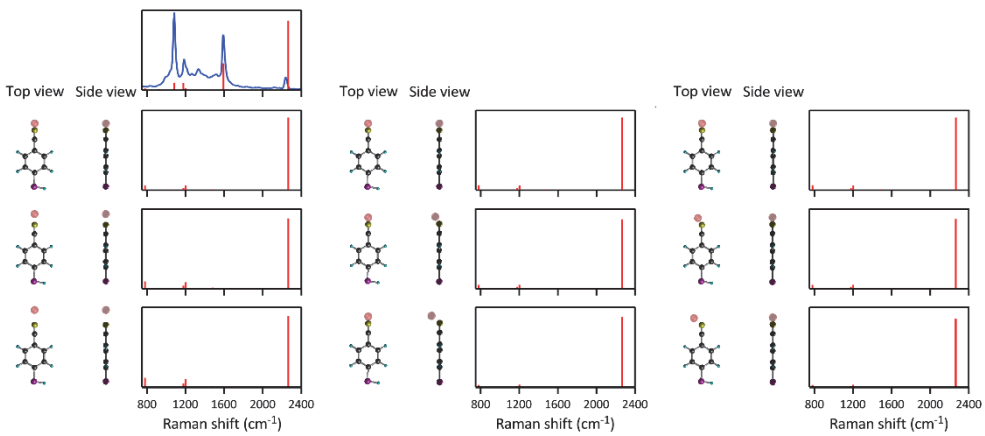

Fig. 28. The simulated picocavity SERS spectra and the relative position of picocavity (red sphere) to the representative para−substituted aromatic thiol MBN. As a comparison, top panel of left column shows SERS spectrum obtained at AgNP−MBN−AuTF junction (blue) and simulated spectrum by DFT. All of the simulated SERS spectra with picocavity located near the νCN group show single νCN peak spectrum.

Secondly, gas phase nitrobenzene (NB) shows pronounced electron of ~2 eV, which is mediated by the anionic state.[107] Such resonant electron scattering of polyatomic molecule, in general, is accompanied by mode selective vibrational excitation. Fig. 29a shows the classical cartoon of my resonant scattering model. The highly energetic electrons which are generated by dephasing of LSP (as described in chapter 1. 6) are ejected from the metallic surface. Vibrationally ground state, neutral NBT receives these electrons to generate NBT^- with bond lengths different from those of neutrals, and the detachment of the electron regenerates neutral but vibrationally hot NBT. Quantum mechanically, the process does not occur sequentially. Rather, these steps occur simultaneously as a single step event (resonant inelastic scattering).[108] It is possible that either direct charge transfer which excites NBT with mono-energetic electrons (scattering via blue arrows in Fig 29b) or indirect charge transfer which excites NBT with electrons whose energy spans from 0 to 0 + $h\nu$ (scattering via red arrow in Fig. 29b) may result in this resonant inelastic scattering.[15] Once again, the charge transfer mechanisms are discussed in chapter 4.5.3. Also, the energy of π^* orbital of NBT^- laid lower than that of π' orbital of NBT (corresponding to HOMO of NBT).[107] As a result, it is expected that the scattering occurs via resonance between π' of NBT and π_2^* of

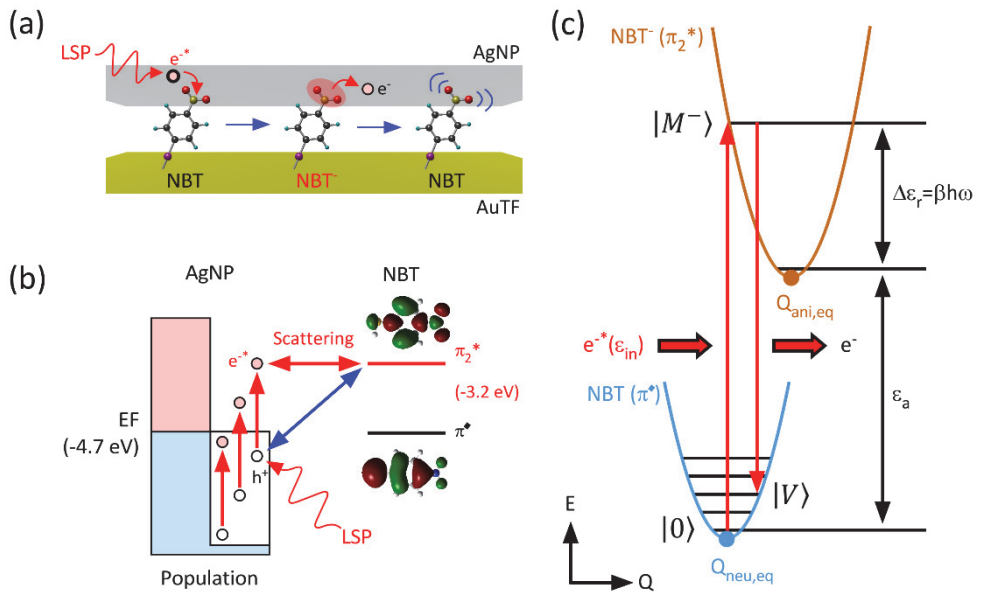

Fig. 29. Vibrational excitation of NBT by inelastic resonant scattering of PIE. (a) The scheme of resonant inelastic electron scattering. The energy of LSP is injected to an electron inside a metal (for indirect charge transfer mechanism) or at metal–molecule interface (for direct charge transfer mechanism). The electron is subsequently transferred to NBT (for indirect charge transfer mechanism) and returns to metal leaving NBT vibrationally excited. This processes occurs at once. (b) Energy transition of PIE and charge transfer process of it. The energy distribution of electrons in metal are shown in left and those of NBT and its molecular orbitals (MOs) are shown in right. For indirect charge transfer process, PIEs are excited inside NP altering band from thermal equilibrium (sky–blue) to nonthermal rectangle (pink) and subsequently scatters with π_2^* (red arrow). For direct charge transfer process, PIE is directly generated at metal–molecule interface and returns to metal (blue arrow). The generation and return of electron occur at once. (c) Energy transition of NBT during the inelastic scattering. The potential curves is the energy of NBT (or NBT^-) aligned in normal mode coordinate (Q_i). The colored circles are normal mode coordinates in equilibrium of NBT (sky–blue) and NBT^- (brown). The red arrow is energy transition during the scattering.

NBT^- (corresponding to LUMO+1 of NBT^-).

Within the Born–Oppenheimer approximation, the probability for resonant inelastic electron–molecule scattering leading to vibrational excitation ($0 \rightarrow V$, where V is the vibrational quantum number of neutral molecule) can be factored into electronic and nuclear (vibrational) parts as follows (see also Fig. 29c)[108–110]

$$p_{tot}(\epsilon_{in}, 0 \rightarrow V) = p_{el}(\epsilon_{in}, \Delta\epsilon) \cdot \left| \sum_{M^-}^{\infty} \frac{\langle V|M^-\rangle\langle M^-|0\rangle}{\epsilon_{in} - \epsilon_{el}^0 - \epsilon_{vib}(M^-) + i\Gamma/2} \right|^2$$

$$= p_{el}(\epsilon_{in}, \Delta\epsilon) \cdot p_{nu}(\epsilon_{in}, \Delta\epsilon)$$

, where $\Delta\epsilon$ is energy difference between initial state and final state, $p_{el}(\epsilon_{in}, \Delta\epsilon)$ is the purely electronic scattering probability for an incident electron with an energy of ϵ_{in} and a scattered electron with an energy of $\epsilon_{in} - \Delta\epsilon$, ϵ_{el}^0 is the energy difference between the neutral and anionic molecules in their vibrational ground states. The $\epsilon_{vib}(M^-)$ and Γ are the vibrational energy of the anionic state with vibrational state M^-, and lifetime broadening of the anion state, respectively. The $\langle V|M^-\rangle$ and $\langle M^-|0\rangle$ are the multi–dimensional Franck–Condon (FC) integral between total vibrational wave functions of anionic ($|M^-\rangle$) and neutral molecules ($|M^-\rangle$ and $|0\rangle$).

Even though $p_{el}(\epsilon_{in}, \Delta\epsilon)$ may affect to mode selectivity of vibrational excitation, I could not evaluate it. To model the mode specificity in vibrational excitation, I evaluate the nuclear part of the transition probability for vibrational excitation of a particular normal mode (v_i), $p_{nu}(\epsilon_{in}, \Delta\epsilon)$ only, using the harmonic oscillator (HO) approximation of normal mode vibration:

$$P_{nu}(\epsilon_{in}, 0 \rightarrow v_i) \cong \left| \sum_{v_i^-=0}^{\infty} \frac{\langle v_i | v_i^- \rangle \langle v_i^- | 0_i \rangle}{\epsilon_{in} - \epsilon_{el}^0 - \epsilon_{vib}(v_i^-) + i\Gamma/2} \right|^2 \cdots\cdots (7)$$

where $|v_i\rangle$ and $|0_i\rangle$ are excited and ground HO vibrational wave functions of neutral molecule along the i'th normal mode coordinate (Q_i) of neutral molecule. Corresponding wave function for anionic species is represented as $|v_i^-\rangle$. The factor $\langle v_i | v_i^- \rangle \langle v_i^- | 0_i \rangle$ mainly determines the mode specificity in vibrational excitation. Assuming the curvatures of NBT and NBT^- are identical to each other, the eqn. 7 can be modulated as eqn. 8 below (displaced harmonic oscillator model, DHO).[108]

$$P_{nu}(\epsilon_{in}, 0 \rightarrow v_i) \cong e^{-2\beta} \frac{\beta^{v_i}}{v_i!} \left| \sum_{v_i^-=0}^{\infty} \frac{A_{v_i^-, v_i}}{\epsilon_{in} - \epsilon_{el}^0 - \epsilon_{vib}(v_i^-) + i\Gamma/2} \right|^2 \cdots\cdots (8)$$

, where

$$A_{m,n} = (-1)^{n-m} L_m^{n-m}(\beta) \quad (n \geq m)$$

$$= (\beta)^{m-n}(n!/m!) L_m^{m-n}(\beta) \quad (m \geq n)$$

$$L_n^{\alpha}(\beta) = \sum_{j=0}^{n} (-1)^j \binom{n+\alpha}{n-j} \beta^j / j!$$

$$\beta_i = \frac{k \Delta Q_{eq,i}^2}{2\mu_i \hbar \omega_v}$$

The p_{nu} (for $v_i \geq 1$) can be non-zero when FC integral has non-zero off-diagonal elements. The magnitude of FC integral described above is related to β which is directly correlated to the displacement of potential curves of NBT^- with respect to that of NBT along the corresponding normal mode coordinate (gap between equilibrium normal coordinates in neutral (($Q_{i,eq}$(n)) and anionic states ($Q_{i,eq}$ (a))). The large value of Franck-Condon integral can be achieved by large β value.

CASSCF quantum chemistry calculations for π' of NBT and π_2^* of NBT^- which participate to inelastic scattering (see Fig. 29b) are performed to obtain harmonic potential energy curves (see method). The anionic form of nitrobenzene (NB^-) and nitrobenzenethiol (NBT^-) in π_2^* state possesses a dominant $\pi^*(NO_2)$-character.[102, 111] Therefore, the geometry (bond length and angle) of NO_2-group in NBT is significantly altered upon addition of an electron (for example,

N−O bond length increases from 1.19 Å to 1.23 Å (+3.8 %)). Whereas, the geometry of aromatic ring in NBT does not show noticeable change upon addition of an electron (for example, C=C bond length slightly decreases from 1.39 Å to 1.38 Å (−1 %)). Such change is reflected as significantly displaced potential energy curves of NBT^- with respect to those of NBT along ν_S(NO) and δNO coordinates (see Fig. 30b−e showing potential curves of Raman−active modes of NBT and NBT^-) and the largest displacement of potential curves for ν_S(NO) yields the largest Franck−Condon factor of ν_S(NO).

The evaluated excitation probabilities (p_{nu}s) with ϵ_{in} ranged from 0 to 4 eV are shown in Fig. 30b−e. For NBT adsorbed on metallic surface, the relative energy of molecular orbitals (MOs) to metal (especially for charged species) cannot be evaluated easily by experiment or calculation.[112] Because of this difficulty, the energy gap between Fermi level of metal (E_F) and π_2^* of NBT^- is arbitrarily assumed to 1.5 eV. The p_{nu}s of each vibrational mode show drastic increase at 1.5 eV. These reveal that the energy of electron should be accessible to MO of NBT and the all vibrational modes may be excited in some degree. For vibrational modes localized to NO_2 group, as mentioned above, p_{nu} is larger than those of vibrational modes localized to ring and ν_S(NO) shows the largest p_{nu} as I observe by

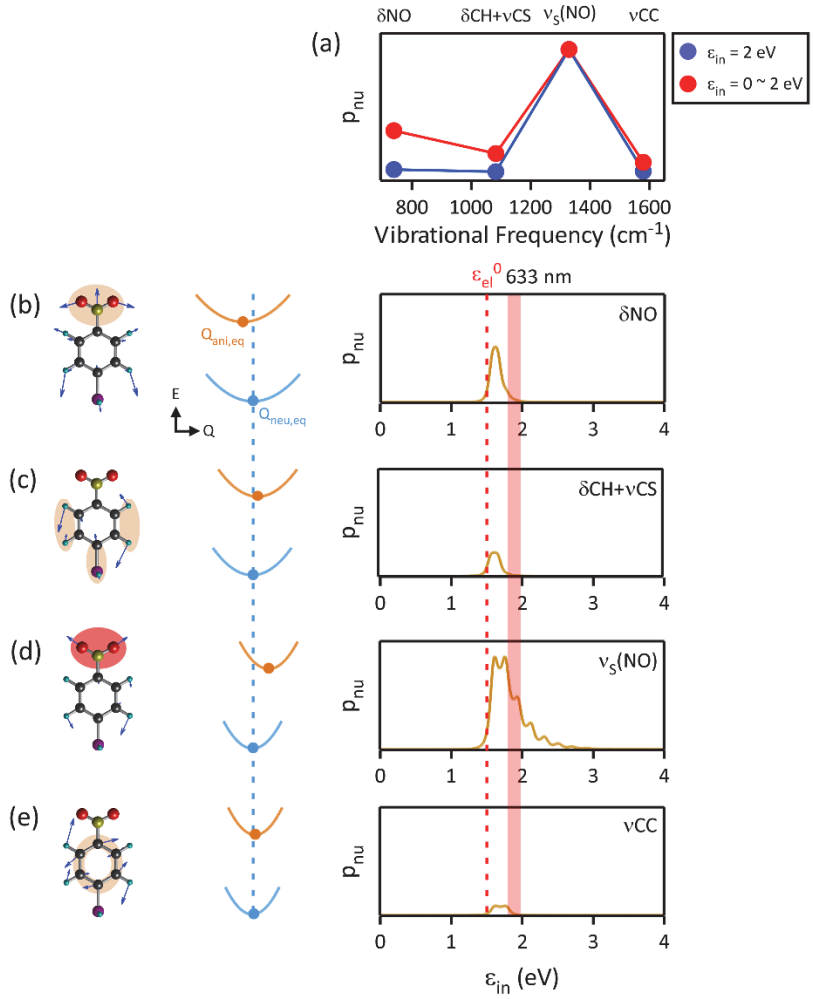

Fig. 30. The calculated potential curves of Raman-active modes and corresponding p_{nu}s. (a) The action spectra of p_{nu}. Blue circles are calculated with mono-energetic excitation of 2 eV assuming exciting medium as a directly transferred hot electron or tunneling electrons. Red circles are calculated with excitation energy spans from 0 to 0 + h_ν assuming exciting medium as an indirectly transferred hot electron. (b-e) The motions of Raman-active modes and corresponding potential curves of NBT (sky-blue) and NBT^- (brown) and p_{nu} with excitation energy from 0 to 4 eV. The brown shades with vibrational motions are regions where vibrational modes are localized. Sky-blue dotted line in left middle column is position of $Q_{eq,neu}$ as a reference. Red dotted line is ϵ^0_{elec} and red shade is the energy of 633 nm photon.

SERS experiment. As I mentioned at chapter 4.5.2., the incident electronic kinetic energy (ϵ_{in}) may be mono-energetic for tunneling electrons in plasmon oscillation and the energetic electron generated by chemical interface damping (CID, $\epsilon_{in} = h\nu$).[15, 113] On the other hand, the incident of electronic kinetic energy may be span an energy range 0 ~ 0 + $h\nu$ eV for fully dephased hot electrons in metal.[15]

The action spectra in Fig. 30a represent calculated p_{nu}s with mono-energetic excitation (red circles) and that with excitation energy spans from 0 to 0 + $h\nu$ (blue circles). The ν_S(NO)-selectivity in the action spectra implies that it is possible that the pumping may be induced by both tunneling plasmon electron and hot-electron by any charge transfer mechanisms. However, currently, I cannot differentiate which is the dominant pumping medium.

4.6. Further discussion

4.6.1. Is the number of electrons participating to scattering enough to achieve sufficient k_{exc} ?

In order to achieve the k_{exc} of 10^{10} s^{-1}, assuming that the pumping is mediated by hot-electrons, the rate of the hot-electrons generation should exceed or be comparable to the k_{exc}.[16] I estimated the rate of hot-electron generation which participates to scattering based on the work of Sykes and his co-workers.[114]

First, I estimated hot-electron generation rate at my plasmonic gap structure. For AgNP (diameter of 185 nm)-Al_2O_3 spacer (thickness of 8 nm) – AuTF junction (thickness of 50 nm) structure which is similar to my SERS platform, the calculated generation rate of hot-electrons all over the metallic surface is about 1.5×10^{17} s^{-1} with laser power of 2.5×10^{8} W cm^{-2}.[114] Considering the laser power density of 1 MW cm^{-2}, I estimate the hot-electron generation rate as 6×10^{14} s^{-1} and this rate far exceeds that of k_{exc} of 10^{10} s^{-1}.

Second, based on the hot-electron generation rate calculated above, I estimated the scattering rate between the electrons and NBTs. I assumed that all generated hot electrons participate to scattering with NBT (with exciting scattering cross section of 10^{-16} cm^2 [106]) within the SERS hot-spot whose area is ~10 nm^2 [11] by strong field enhancement.[115] Following the assumption, the scattering rate was estimated to 4.0×10^{11} s^{-1}. This scattering rate far exceed k_{exc} of 10^{10} s^{-1} and this rate is meaningful in the view that it possibly exceed the k_{exc}.

4.6.2. Why vibrational modes pumped by scattering ?

I modelled inelastic resonant electron scattering as a vibrational pumping process. Whereas, Christopher and his co-workers suggested that gas phase oxygen molecule adjacent to plasmonic

nanostructure undergo attachment / detachment process of hot-electron which occurs in two-step and this process lead to vibrational pumping.[98] In this process, similar to fluorescence, single electron is attached to the molecules generating vibraionally excited anion and subsequent relaxation to vibrational ground of anion is followed.[15] In a few ns, the electron detachment of the anion in vibrational ground state occurs resulting neutral molecule in vibrationally excited state. This neutral molecule relaxed to ground state once again. For gas phase molecules, the long lifetime of vibrationally excited state (τ_{rel} ~ 10 μs) may lead to the unusual chemical reaction which cannot be induced by thermal heating.[3] For an adsorbate molecules on metallic surface, however, lifetime of vibrationally excited state for both neutral and anion are significantly shorter than that of vibrational ground state ($\tau_{rel,v\geq1}$ is 0.1 % of $\tau_{rel,v=0}$). If the process Christopher suggested induces vibrational pumping of NBT, I am not able to observe the vibrationally excited NBT by SERS because of the rapid relaxation.[15] In this point of view, it is reasonable to believe that the strong anti-Stokes SERS is induced via electron scattering process.

4.6.3. Mode selectivity of scattering between electron and non-π_2^* orbital

Based on the model calculation, I further studied that which mode shows selectivity when electron scatters with MO, not π_2^*. Fig. 31a and d show scheme of electron scattering with π'^* (HOMO of NBT^-) and π^* (HOMO−1 of NBT^-) respectively. I set the gap between energy of E_F and those of MOs participating to scattering for 1.5 eV which is coincide with π_2^* case. Fig 30b and e show the p_{nu}s which correspond to schemes in Fig 30a and d calculated with ϵ_{in} of 0 ~ 4 eV. Whether I assume the electrons are directly transferred or indirectly, electron scattering with π^* which is localized to NO_2 group leads to ν_S(NO)−selective excitation similarly to scattering with π_2^*(see Fig. 31f). On the other hand, the scattering with π'^* shows mode selectivity to δCH for indirect charge transfer. This mode is not localized to nitro group. Similar to scattering with π_2^*, the bond length of NO is considerably increased from 1.19 Å to 1.26 Å upon addition of an electron to π^* orbital (+ 6.14 %). On the other hand, bond length of C=C in aromatic ring decreases from 1.39 Å to 1.37 Å (−1.3 %). For scattering with π'^*, however, bond length of NO remains in 1.19 Å and that of C=C increases from 1.39 Å to 1.44 Å (+3.8 %). Based on these calculations, once again, I can infer the ν_S(NO)−selectivity is strongly correlated to geometry alteration during scattering process. Furthermore, it is expected that the vibrational pumping of the modes which are localized to out of nitro group may be achieved

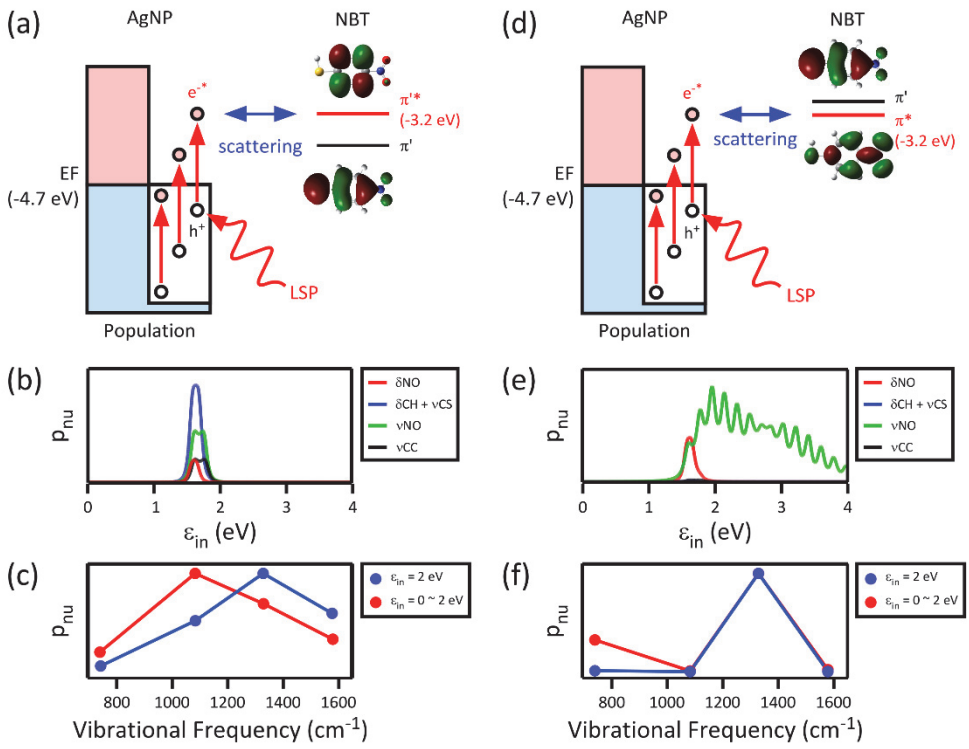

Fig. 31. p_{nu}s of electron scattering with MOs of NBT which is accessible (π'^{*} and π^{*}). The calculations are conducted for Raman-active mode only (a-c) p_{nu} of scattering between electrons and π'^{*}. (a) The scheme of inelastic scattering between electron and π'^{*}. (b) p_{nu}s calculated with ϵ_{in} of 0 ~ 4 eV. (c) The integrated p_{nu}s sampled from ϵ_{in} = 2 eV (blue circles) and ϵ_{in} span from 0 ~ 2 eV (red circles). (d-f) p_{nu}s of scattering between electrons and π^{*}. (d) The scheme of inelastic scattering between electron and π^{*}. (e) p_{nu}s calculated with ϵ_{in} of 0 ~ 4 eV. (f) The integrated p_{nu}s sampled from ϵ_{in} = 2 eV (blue circles) and ϵ_{in} span from 0 ~ 2 eV (red circles).

by tuning the excitation wavelength or applying external electric bias.

4.6.4. Vibrational pumping of Raman inactive modes

I also investigated the possibility of vibrational pumping of Raman inactive modes. Fig. 32 shows the p_{nu}s of all vibrational modes of NBT including Raman inactive modes. Fig. 32a−c respectively show the p_{nu} values obtained from the calculation of scattering between electrons and π^*, π'^*, π_2^* orbitals by direct charge transfer. Assuming that electrons are indirectly transferred, also, p_{nu}s are shown in Fig 32d−f. For the cases of scattering with π^* and π_2^*, excitation probability of ν_S(NO) is the largest even if it is compared with those of Raman inactive modes. For the cases of scattering with π'^*, however, not only ν_S(NO)−selectivity are not shown but also p_{nu} of νSH mode exceeds the those of other modes. As I mentioned previous chapter, these calculations suggest that various vibrational modes may be efficiently pumped through the scattering between electron and π'^* orbital by tuning wavelength of laser or applying the external bias even though this pumping cannot be observed by SERS.

4.6.5. Vibrational pumping of product molecule, DMAB

Also, I observed vibrational pumping of reaction product dimercaptoazobenzene (DMAB) which is formed by the dimerization

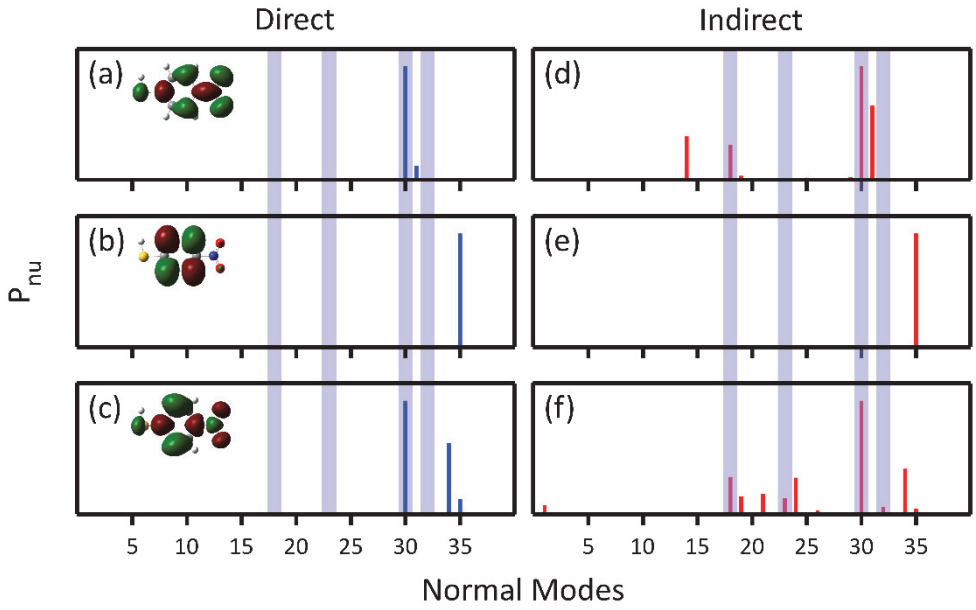

Fig. 32. p_{nu}s of all vibrational modes. (a−c) p_{nu}s with the assumption that electrons are directly transferred to π^*, π'^* and π_2^* respectively. (d−f) p_{nu}s with the assumption that electrons are indirectly transferred to π^*, π'^* and π_2^* respectively. The colored shades are positions of Raman−active modes.

of either NBT or ABT. Fig. 33 show that time-resolved spectra of AgNP-NBT-AuTF, AgNP-ABT-AuTF and AgNP-DMAB-AuTF as a comparison. In the spectra of NBT and ABT (Fig. 33a, b), the intense peaks of DMAB immerge on both anti-Stokes side and Stokes side during the reaction (for example, t = 0.85 ~ 1 s for NBT and t = 1.92 ~ 2.16 s for ABT). In the points of view that (1) anti-Stokes intensity of DMAB shows stepwise alteration, (2) the peaks are immerged simultaneously on Stokes and anti-Stokes side, this pumping may seem similar to picocavity SERS. However, SERS spectra which appeared by the photo-reaction (1) contain only Raman-active modes, (2) cannot be reproduced by picocavity calculation easily (see Fig. 34 and 35) and (3) show high reproducibility. These features are considerably different from those of picocavity SERS. However, as shown in Fig. 33c, such pumping is not observed from SERS of AgNP-DMAB-AuTF junction with excitation of He-Ne laser (λ_{ex} = 633 nm). I estimate that the pumping may arise from whether (1) vibrational energy transfer from vibrationally excited adjacent NBT or ABT (see Fig. 36a) or (2) current induced by DMAB generated at narrow gap which could *bridge* two metallic surfaces (see Fig. 36b). To compare the pumping efficiency of these molecules, I calculated p_{nu}s of ABT and DMAB and compared each other. The p_{nu}s are calculated by potential curves

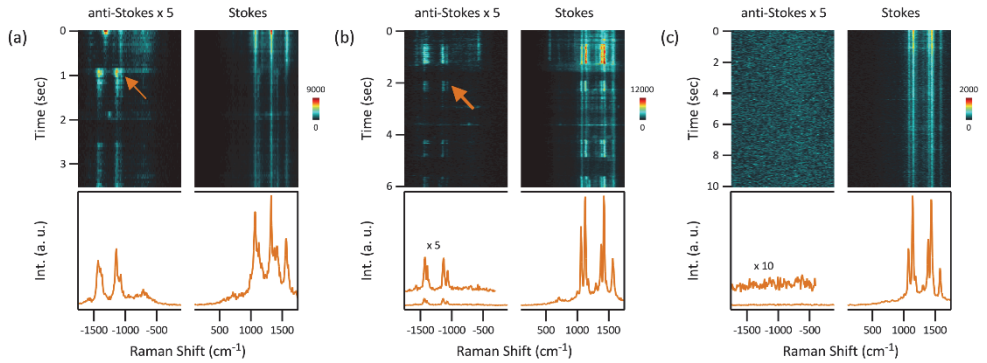

Fig. 33. SERS spectrum of AgNP−NBT−AuTF, AgNP−ABT−AuTF junction and AgNP−DMAB−AuTF junction. (a) Time−resolved SERS spectra of AgNP−NBT−AuTF junction and the cross section spectrum obtained from t = 0.85 ~ 1 s (marked with brown arrow). (b) Time−resolved SERS spectra of AgNP−ABT−AuTF junction and the cross section spectrum obtained from t = 1.92 ~ 2.16 s (marked with brown arrow). The anti−Stokes side is magnified 5 times. (b) Time−resolved SERS spectra of AgNP−DMAB−AuTF junction, the averaged spectrum and vibrational motion of DMAB. The anti−Stokes side is magnified 10 times.

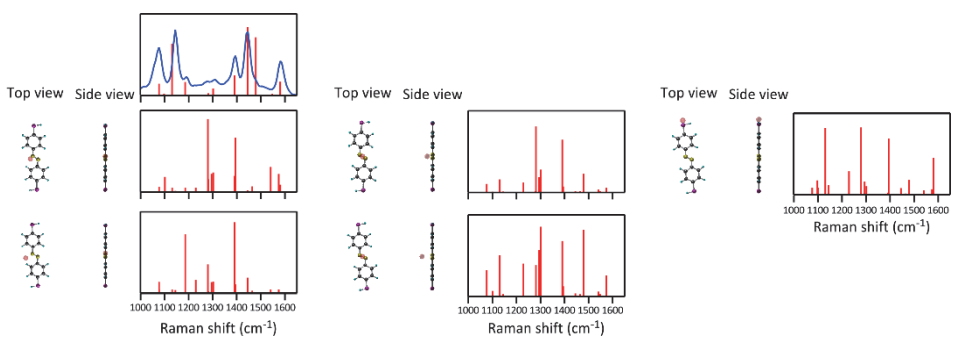

Fig. 34. The simulated picocavity SERS spectra and the relative position of picocavity (red sphere) to the DMAB. As a comparison, top panel of left column shows SERS spectrum obtained at AgNP−DMAB−AuTF junction (blue) and simulated spectra by DFT. Whether the position of picocavity is near the metallic surface or near the N=N group, no calculated spectrum seems similar to that of SERS spectrum of product of photo−reaction.

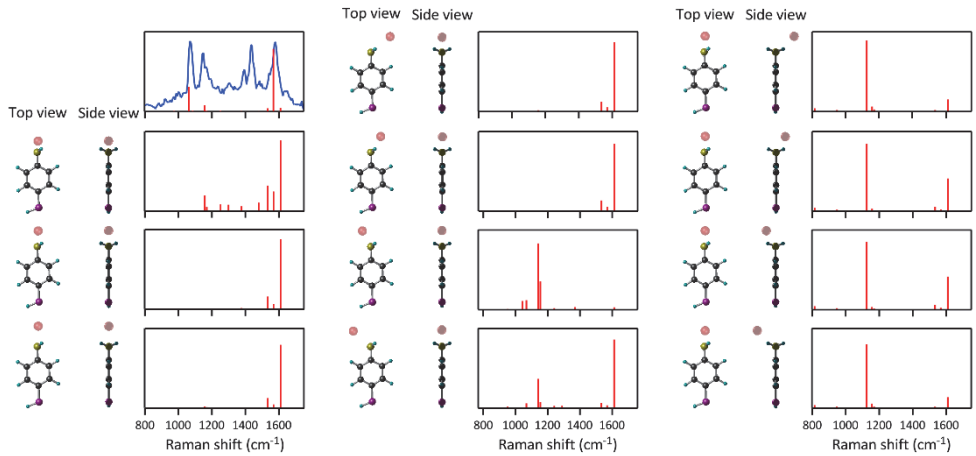

Fig. 35. The simulated picocavity SERS spectra and the relative position of picocavity (red sphere) to the ABT. As a comparison, top panel of left column shows SERS spectrum obtained at AgNP−ABT−AuTF junction (blue) and simulated spectra by DFT. No calculated spectrum seems similar to that of SERS spectrum of product of photo−reaction.

of molecules (ABT and DMAB) and the curves are obtained by DFT calculation (Gaussian09 package,[63] basis set of 6−311G+ for ABT and 6−31G+(d,p)). The calculated results are shown in Fig. 37. The colored sticks in middle panels show p_{nu}s of direct charge transfer model and those in bottom panels show p_{nu}s of indirect charge transfer model. For comparison between molecules, p_{nu}s of NBT, ABT and DMAB are normalized by those of νCC. p_{nu}s ABT are expected to be smaller than that of ν_S(NO) of NBT (colored circles in Fig. 37b,c). This p_{nu}s value could lead to vibrational pumping. However, it cannot assure that efficient vibrational pumping may be induced by energy transfer from excited molecule. On the other hand, some p_{nu}s of DMAB are comparable to that of ν_S(NO). Also, especially for indirect charge transfer case, the calculated action spectrum of p_{nu} resembles SERS spectrum of DMAB. Following this calculation, the electron scattering itself may cause the vibrational pumping of DMAB. This hypothesis may be possible, however, the contact status of DMAB and current flowing through the *bridge* molecule should be confirmed. Unfortunately, I cannot be sure the contact status of DMAB molecules with our experimental setup at this time. Further SERS studies equipped with the tool which can confirm the contact status such as STM or break junction[116−119] are needed to reveal the origin of this vibrational pumping.

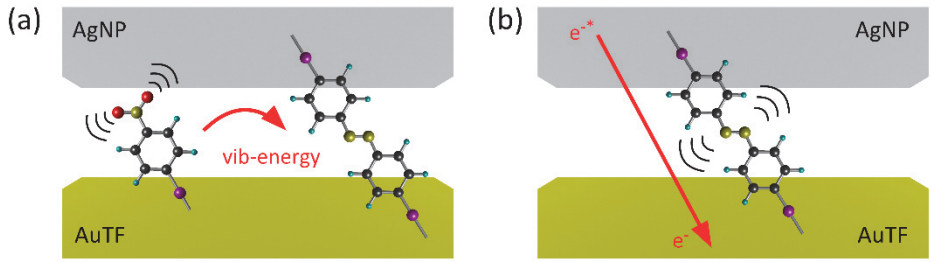

Fig. 36. Scheme of estimated pumping mechanisms of DMAB. (a) Once vibrationally excited NBT by PIE, transfers vibratinoal energy to DMAB molecule in proximity (b) Current through the DMAB molecule bridging both metallic surface transfers vibrational energy to the molecule.

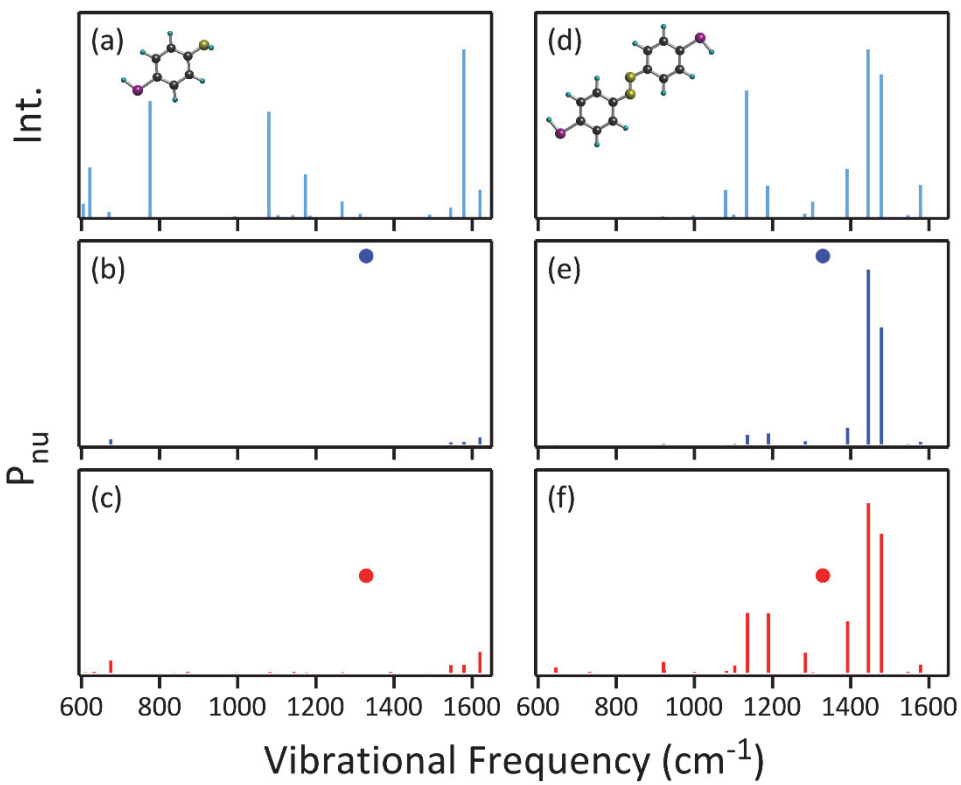

Fig. 37. p_{nu} of ABT and DMAB. (a,d) Calculated Raman spectra of ABT and DMAB as comparison. (b) p_{nu} of ABT calculated with mono-energetic excitation (blue stick, ϵ_{in} = 2 eV) and the p_{nu} of ν_S(NO) of NBT as comparison (ϵ_{in} = 2 eV, blue circle). (c) p_{nu} of ABT calculated with ϵ_{in}

span from 0 eV to 2 eV (red stick) and the p_{nu} of ν_S(NO) of NBT as comparison (ϵ_{in} = 0 ~ 2 eV, red circle). (e) p_{nu} of DMAB calculated with mono-energetic excitation (blue stick, ϵ_{in} = 2 eV) and the p_{nu} of ν_S(NO) of NBT as comparison (ϵ_{in} = 2 eV, blue circle). (f) p_{nu} of DMAB calculated with ϵ_{in} span from 0 eV to 2 eV (red stick) and the p_{nu} of ν_S(NO) of NBT as comparison (ϵ_{in} = 0 ~ 2 eV, red circle).

4.7. Conclusion

Recent reports regarding plasmon-assisted chemical reactions postulate that indirect transfer of hot electrons or CID may vibrationally excite electronically ground state molecule, promoting the chemical reaction. The issue is also related to the decay mechanism of localized surface plasmons. Traditionally, focus has not on how and where this energy is deposited. However, it has remained unchecked whether or not such excitation will be efficient enough to overcome the rapid vibrational relaxation and thus affect the subsequent (slow) bimolecular chemical reaction. My result provides a partial support on this postulate: Even with a CW laser excitation been primarily on the loss of energy by the adsorbed molecules, but with a moderate power, the plasmon-induced vibrational excitation, under a favorable condition, can overcome the vibrational relaxation and can affect the subsequent chemical reaction steps. In fact, it is possible that many of the unusual plasmon-assisted chemical reactivity may have been caused by the vibrationally hot reactants.

Whether or not the vibrational energy deposited on reactant molecule will be available for chemical reaction depends on the specific nature of the chemical reaction, and the energy transfer rate. Although I do not currently have any data to support such possibility, I do have data which can be translated that some of the deposited

energy on NBT can be transferred to the nearby molecules: I often observe vibrationally hot DMAB reaction product during the course of reaction. Fully saturated monolayer of pure DMAB under the same irradiation condition does not show any sign of vibrational excitation, showing that the vibrational energy deposited in NBT is readily available for inter-molecular energy transfer.

Meanwhile, the vibrational pumping of DMAB generated by photo-reaction may also be interpreted as a result of current which flow through the molecules *bridging* two metallic surface. Even though this hypothesis still awaits for confirmation, it suggests the possibility that (1) vibrational pumping may be controlled by current and (2) surface chemistry may also be controlled as a result of the pumping.

Even though I discussed that the origin of the accumulated vibrational energy of ν_S(NO) is part of PIE energy, it may be still too hard to discriminate the picocavity SERS and electron induced vibrational pumping clearly. In the point of view that (1) the orientation of molecule are aligned parallel to the gap axis with cucurbituril as a host[49, 120] and (2) the field confinement of picocavity is narrower than 5 Å[103-104], it may be possible to discriminate between these two processes by measuring SERS together with cucurbituril and shell-isolated nanoparticle[121]. In this molecular geometry, picocavity cannot confined the strong EM field near the

NO_2 group of NBT and reproduce single ν_S(NO) peak spectrum. If anti-Stokes SERS of ν_S(NO) may possibly be measured under any light illumination, thus, the pumping mechanism may be regarded as a result of electron scattering.

To conclude, I have observed unusual mode specific vibrational excitation of nitrobenzenethiol during the plasmon-assisted chemical reaction. The spectro-temporal features of the excitation cannot be explained by any of the photo-thermal, purely optical pumping, or picocavity excitation mechanisms. Instead, they could be explained by the resonant inelastic scattering of electrons. The result demonstrates that the rate of electron-induced-activation of molecules can be large enough to overcome rapid vibrational relaxation of molecules on metals, resulting in significant non-statistical population of vibrationally excited molecules at the time scale of ~1 second. The result overall shows a new possibility to vibrationally controlling the chemistry of metal-adsorbed molecule, which have been regarded by many an impossible goal.

Reference

1. Crim, F. F., Chemical dynamics of vibrationally excited molecules: Controlling reactions in gases and on surfaces. *Proc. Natl. Acad. Sci. U. S. A.* 2008, *105* (35), 12654.

2. Zare, R. N., Laser Control of Chemical Reactions. *Science* 1998, *279* (5358), 1875.

3. Blackman, V., Vibrational relaxation in oxygen and nitrogen. *J. Fluid. Mech.* 1956, *1* (1), 61-85.

4. Keller, E. L.; Frontiera, R. R., Ultrafast Nanoscale Raman Thermometry Proves Heating Is Not a Primary Mechanism for Plasmon-Driven Photocatalysis. *ACS Nano* 2018, *12* (6), 5848-5855.

5. Halas, N. J.; Lal, S.; Chang, W.-S.; Link, S.; Nordlander, P., Plasmons in Strongly Coupled Metallic Nanostructures. *Chem. Rev.* 2011, *111* (6), 3913-3961.

6. Schlücker, S., Surface-Enhanced Raman Spectroscopy: Concepts and Chemical Applications. *Angew. Chem. Int. Ed.* 2014, *53* (19), 4756-4795.

7. Xu, H.; Aizpurua, J.; Käll, M.; Apell, P., Electromagnetic contributions to single-molecule sensitivity in surface-enhanced Raman scattering. *Phy. Rev. E* 2000, *62* (3), 4318-4324.

8. Barrow, S. J.; Rossouw, D.; Funston, A. M.; Botton, G. A.; Mulvaney, P., Mapping Bright and Dark Modes in Gold Nanoparticle Chains using Electron Energy Loss Spectroscopy. *Nano Lett.* 2014, *14* (7), 3799−3808.

9. Liu, M.; Lee, T.−W.; Gray, S. K.; Guyot−Sionnest, P.; Pelton, M., Excitation of Dark Plasmons in Metal Nanoparticles by a Localized Emitter. *Phys. Rev. Lett.* 2009, *102* (10), 107401.

10. Zhu, W.; Crozier, K. B., Quantum mechanical limit to plasmonic enhancement as observed by surface−enhanced Raman scattering. *Nat. Commun.* 2014, *5* (1), 5228.

11. Choi, H.−K.; Park, W.−H.; Park, C.−G.; Shin, H.−H.; Lee, K. S.; Kim, Z. H., Metal−Catalyzed Chemical Reaction of Single Molecules Directly Probed by Vibrational Spectroscopy. *J. Am. Chem. Soc.* 2016, *138* (13), 4673−4684.

12. Le Ru, E. C.; Etchegoin, P. G., Principles of Surface−Enhanced Raman Spectroscopy and related plasmonic effects. *Elsevier: Amsterdam, 2009*.

13. Blackie, E. J.; Le Ru, E. C.; Etchegoin, P. G., Single−Molecule Surface−Enhanced Raman Spectroscopy of Nonresonant Molecules. *J. Am. Chem. Soc.* 2009, *131* (40), 14466−14472.

14. Pozzi, E. A.; Zrimsek, A. B.; Lethiec, C. M.; Schatz, G. C.; Hersam, M. C.; Van Duyne, R. P., Evaluating Single−Molecule Stokes

and Anti-Stokes SERS for Nanoscale Thermometry. *J. Phys. Chem. C* 2015, *119* (36), 21116-21124.

15. Linic, S.; Aslam, U.; Boerigter, C.; Morabito, M., Photochemical transformations on plasmonic metal nanoparticles. *Nat. Mater.* 2015, *14* (6), 567-576.

16. Brongersma, M. L.; Halas, N. J.; Nordlander, P., Plasmon-induced hot carrier science and technology. *Nat. Nanotechnol.* 2015, *10* (1), 25-34.

17. Willets, K. A.; Wilson, A. J.; Sundaresan, V.; Joshi, P. B., Super-Resolution Imaging and Plasmonics. *Chem. Rev.* 2017, *117* (11), 7538-7582.

18. Burda, C.; Chen, X.; Narayanan, R.; El-Sayed, M. A., Chemistry and Properties of Nanocrystals of Different Shapes. *Chem. Rev.* 2005, *105* (4), 1025-1102.

19. Evanoff Jr, D. D.; Chumanov, G., Synthesis and Optical Properties of Silver Nanoparticles and Arrays. *ChemPhysChem* 2005, *6* (7), 1221-1231.

20. Liu, M.; Pelton, M.; Guyot-Sionnest, P., Reduced damping of surface plasmons at low temperatures. *Phys. Rev. B* 2009, *79* (3), 035418.

21. Tas, G.; Maris, H. J., Electron diffusion in metals studied by picosecond ultrasonics. *Phys. Rev. B* 1994, *49* (21), 15046-15054.

22. Del Fatti, N.; Voisin, C.; Achermann, M.; Tzortzakis, S.; Christofilos, D.; Vallée, F., Nonequilibrium electron dynamics in noble metals. *Phys. Rev. B* 2000, *61* (24), 16956−16966.

23. Link, S.; El−Sayed, M. A., Spectral Properties and Relaxation Dynamics of Surface Plasmon Electronic Oscillations in Gold and Silver Nanodots and Nanorods. *J. Phys. Chem. B* 1999, *103* (40), 8410−8426.

24. Fann, W. S.; Storz, R.; Tom, H. W. K.; Bokor, J., Electron thermalization in gold. *Phys. Rev. B* 1992, *46* (20), 13592−13595.

25. Sun, C. K.; Vallée, F.; Acioli, L. H.; Ippen, E. P.; Fujimoto, J. G., Femtosecond−tunable measurement of electron thermalization in gold. *Phys. Rev. B* 1994, *50* (20), 15337−15348.

26. Zhang, Y.; He, S.; Guo, W.; Hu, Y.; Huang, J.; Mulcahy, J. R.; Wei, W. D., Surface−Plasmon−Driven Hot Electron Photochemistry. *Chem. Rev.* 2018, *118* (6), 2927−2954.

27. Watanabe, K.; Menzel, D.; Nilius, N.; Freund, H.−J., Photochemistry on Metal Nanoparticles. *Chem. Rev.* 2006, *106* (10), 4301−4320.

28. Manjavacas, A.; Liu, J. G.; Kulkarni, V.; Nordlander, P., Plasmon−Induced Hot Carriers in Metallic Nanoparticles. *ACS Nano* 2014, *8* (8), 7630−7638.

29. Bauer, C.; Abid, J.−P.; Girault, H. H., Hot Adsorbate−Induced

Retardation of the Internal Thermalization of Nonequilibrium Electrons in Adsorbate-Covered Metal Nanoparticles. *J. Phys. Chem. B* 2006, *110* (10), 4519-4523.

30. Bauer, C.; Abid, J.-P.; Fermin, D.; Girault, H. H., Ultrafast chemical interface scattering as an additional decay channel for nascent nonthermal electrons in small metal nanoparticles. *J. Chem. Phys.* 2004, *120* (19), 9302-9315.

31. Boerigter, C.; Aslam, U.; Linic, S., Mechanism of Charge Transfer from Plasmonic Nanostructures to Chemically Attached Materials. *ACS Nano* 2016, *10* (6), 6108-6115.

32. Boerigter, C.; Campana, R.; Morabito, M.; Linic, S., Evidence and implications of direct charge excitation as the dominant mechanism in plasmon-mediated photocatalysis. *Nat. Commun.* 2016, *7* (1), 10545.

33. Marimuthu, A.; Zhang, J.; Linic, S., Tuning Selectivity in Propylene Epoxidation by Plasmon Mediated Photo-Switching of Cu Oxidation State. *Science* 2013, *339* (6127), 1590.

34. Moskovits, M., Surface-enhanced spectroscopy. *Rev. Mod. Phys.* 1985, *57* (3), 783-826.

35. Stiles, P. L.; Dieringer, J. A.; Shah, N. C.; Van Duyne, R. P., Surface-Enhanced Raman Spectroscopy. *Annu. Rev. Anal. Chem.* 2008, *1* (1), 601-626.

36. Zrimsek, A. B.; Chiang, N.; Mattei, M.; Zaleski, S.; McAnally, M. O.; Chapman, C. T.; Henry, A.-I.; Schatz, G. C.; Van Duyne, R. P., Single-Molecule Chemistry with Surface- and Tip-Enhanced Raman Spectroscopy. *Chem. Rev.* 2017, *117* (11), 7583-7613.

37. Moskovits, M., Persistent misconceptions regarding SERS. *Phys. Chem. Chem. Phys.* 2013, *15* (15), 5301-5311.

38. Kneipp, K.; Wang, Y.; Kneipp, H.; Perelman, L. T.; Itzkan, I.; Dasari, R. R.; Feld, M. S., Single Molecule Detection Using Surface-Enhanced Raman Scattering (SERS). *Phys. Rev. Lett.* 1997, *78* (9), 1667-1670.

39. Le Ru, E. C.; Meyer, M.; Etchegoin, P. G., Proof of Single-Molecule Sensitivity in Surface Enhanced Raman Scattering (SERS) by Means of a Two-Analyte Technique. *J. Phys. Chem. B* 2006, *110* (4), 1944-1948.

40. Xu, H.; Bjerneld, E. J.; Käll, M.; Börjesson, L., Spectroscopy of Single Hemoglobin Molecules by Surface Enhanced Raman Scattering. *Phys. Rev. Lett.* 1999, *83* (21), 4357-4360.

41. Dieringer, J. A.; Lettan, R. B.; Scheidt, K. A.; Van Duyne, R. P., A Frequency Domain Existence Proof of Single-Molecule Surface-Enhanced Raman Spectroscopy. *J. Am. Chem. Soc.* 2007, *129* (51), 16249-16256.

42. Ward, D. R.; Halas, N. J.; Ciszek, J. W.; Tour, J. M.; Wu, Y.;

Nordlander, P.; Natelson, D., Simultaneous Measurements of Electronic Conduction and Raman Response in Molecular Junctions. *Nano Lett.* 2008, *8* (3), 919.

43. Haran, G., Single-Molecule Raman Spectroscopy: A Probe of Surface Dynamics and Plasmonic Fields. *Acc. Chem. Res.* 2010, *43* (8), 1135-1143.

44. Le Ru, E. C.; Etchegoin, P. G., Single-Molecule Surface-Enhanced Raman Spectroscopy. *Annu. Rev. Phys. Chem.* 2012, *63* (1), 65-87.

45. Mirsaleh-Kohan, N.; Iberi, V.; Simmons, P. D.; Bigelow, N. W.; Vaschillo, A.; Rowland, M. M.; Best, M. D.; Pennycook, S. J.; Masiello, D. J.; Guiton, B. S.; Camden, J. P., Single-Molecule Surface-Enhanced Raman Scattering: Can STEM/EELS Image Electromagnetic Hot Spots? *J. Phys. Chem. Lett.* 2012, *3* (16), 2303-2309.

46. Kitahama, Y.; Araki, D.; Yamamoto, Y. S.; Itoh, T.; Ozaki, Y., Different behaviour of molecules in dark SERS state on colloidal Ag nanoparticles estimated by truncated power law analysis of blinking SERS. *Phys. Chem. Chem. Phys.* 2015, *17* (33), 21204-21210.

47. Zhang, Z.; Deckert-Gaudig, T.; Singh, P.; Deckert, V., Single molecule level plasmonic catalysis - a dilution study of p-nitrothiophenol on gold dimers. *Chem. Commun.* 2015, *51* (15),

3069−3072.

48. Banik, M.; El−Khoury, P. Z.; Nag, A.; Rodriguez−Perez, A.; Guarrottxena, N.; Bazan, G. C.; Apkarian, V. A., Surface−Enhanced Raman Trajectories on a Nano−Dumbbell: Transition from Field to Charge Transfer Plasmons as the Spheres Fuse. *ACS Nano* 2012, *6* (11), 10343−10354.

49. Taylor, R. W.; Coulston, R. J.; Biedermann, F.; Mahajan, S.; Baumberg, J. J.; Scherman, O. A., In Situ SERS Monitoring of Photochemistry within a Nanojunction Reactor. *Nano Lett.* 2013, *13* (12), 5985−5990.

50. Milojevich, C. B.; Mandrell, B. K.; Turley, H. K.; Iberi, V.; Best, M. D.; Camden, J. P., Surface−Enhanced Hyper−Raman Scattering from Single Molecules. *J. Phys. Chem. Lett.* 2013, *4* (20), 3420−3423.

51. Trautmann, S.; Aizpurua, J.; Götz, I.; Undisz, A.; Dellith, J.; Schneidewind, H.; Rettenmayr, M.; Deckert, V., A classical description of subnanometer resolution by atomic features in metallic structures. *Nanoscale* 2017, *9* (1), 391−401.

52. Liu, P.; Chulhai, D. V.; Jensen, L., Single−Molecule Imaging Using Atomistic Near−Field Tip−Enhanced Raman Spectroscopy. *ACS Nano* 2017, *11* (5), 5094−5102.

53. Barbry, M.; Koval, P.; Marchesin, F.; Esteban, R.; Borisov, A.

G.; Aizpurua, J.; Sánchez-Portal, D., Atomistic Near-Field Nanoplasmonics: Reaching Atomic-Scale Resolution in Nanooptics. *Nano Lett.* 2015, *15* (5), 3410-3419.

54. Zhang, P.; Feist, J.; Rubio, A.; García-González, P.; García-Vidal, F. J., Ab initio nanoplasmonics: The impact of atomic structure. *Phys. Rev. B* 2014, *90* (16), 161407.

55. Zhang, R.; Zhang, Y.; Dong, Z. C.; Jiang, S.; Zhang, C.; Chen, L. G.; Zhang, L.; Liao, Y.; Aizpurua, J.; Luo, Y.; Yang, J. L.; Hou, J. G., Chemical mapping of a single molecule by plasmon-enhanced Raman scattering. *Nature* 2013, *498* (7452), 82-86.

56. Jiang, S.; Zhang, Y.; Zhang, R.; Hu, C.; Liao, M.; Luo, Y.; Yang, J.; Dong, Z.; Hou, J. G., Distinguishing adjacent molecules on a surface using plasmon-enhanced Raman scattering. *Nat. Nanotechnol.* 2015, *10* (10), 865-869.

57. Chiang, N.; Chen, X.; Goubert, G.; Chulhai, D. V.; Chen, X.; Pozzi, E. A.; Jiang, N.; Hersam, M. C.; Seideman, T.; Jensen, L.; Van Duyne, R. P., Conformational Contrast of Surface-Mediated Molecular Switches Yields Ångstrom-Scale Spatial Resolution in Ultrahigh Vacuum Tip-Enhanced Raman Spectroscopy. *Nano Lett.* 2016, *16* (12), 7774-7778.

58. Latorre, F.; Kupfer, S.; Bocklitz, T.; Kinzel, D.; Trautmann, S.; Gräfe, S.; Deckert, V., Spatial resolution of tip-enhanced Raman

spectroscopy – DFT assessment of the chemical effect. *Nanoscale* 2016, *8* (19), 10229–10239.

59. Benz, F.; Schmidt, M. K.; Dreismann, A.; Chikkaraddy, R.; Zhang, Y.; Demetriadou, A.; Carnegie, C.; Ohadi, H.; de Nijs, B.; Esteban, R.; Aizpurua, J.; Baumberg, J. J., Single-molecule optomechanics in "picocavities". *Science* 2016, *354* (6313), 726.

60. Duan, S.; Tian, G.; Luo, Y., Visualization of Vibrational Modes in Real Space by Tip-Enhanced Non-Resonant Raman Spectroscopy. *Angew. Chem. Int. Ed.* 2016, *55* (3), 1041-1045.

61. Dhawan, A.; Norton, S. J.; Gerhold, M. D.; Vo-Dinh, T., Comparison of FDTD numerical computations and analytical multipole expansion method for plasmonics-active nanosphere dimers. *Opt. Express* 2009, *17* (12), 9688-9703.

62. Palik, E. D., *Handbook of Optical Constants of Solids., Academic Press: San Diego* 1998.

63. Frisch, M. J.; Trucks, G. W.; Schlegel, H. B.; Scuseria, G. E.; Robb, M. A.; Cheeseman, J. R.; Scalmani, G.; Barone, V.; Mennucci, B.; Petersson, G. A.; Nakatsuji, H.; Caricato, M.; Li, X.; Hratchian, H. P.; Izmaylov, A. F.; Bloino, J.; Zheng, G.; Sonnenberg, J. L.; Hada, M.; Ehara, M.; Toyota, K.; Fukuda, R.; Hasegawa, J.; Ishida, M.; Nakajima, T.; Honda, Y.; Kitao, O.; Nakai, H.; Vreven, T.; Montgomery Jr., J. A.; Peralta, J. E.; Ogliaro, F.; Bearpark, M. J.; Heyd, J.; Brothers, E. N.;

Kudin, K. N.; Staroverov, V. N.; Kobayashi, R.; Normand, J.; Raghavachari, K.; Rendell, A. P.; Burant, J. C.; Iyengar, S. S.; Tomasi, J.; Cossi, M.; Rega, N.; Millam, N. J.; Klene, M.; Knox, J. E.; Cross, J. B.; Bakken, V.; Adamo, C.; Jaramillo, J.; Gomperts, R.; Stratmann, R. E.; Yazyev, O.; Austin, A. J.; Cammi, R.; Pomelli, C.; Ochterski, J. W.; Martin, R. L.; Morokuma, K.; Zakrzewski, V. G.; Voth, G. A.; Salvador, P.; Dannenberg, J. J.; Dapprich, S.; Daniels, A. D.; Farkas, Ö.; Foresman, J. B.; Ortiz, J. V.; Cioslowski, J.; Fox, D. J., *Rev. B01 ed.; Gaussian, Inc.: Willingford, CT, Gaussian 09.* 2009.

64. Zhao, L.-B.; Zhang, M.; Huang, Y.-F.; Williams, C. T.; Wu, D.-Y.; Ren, B.; Tian, Z.-Q., Theoretical Study of Plasmon-Enhanced Surface Catalytic Coupling Reactions of Aromatic Amines and Nitro Compounds. *J. Phys. Chem. Lett.* 2014, *5* (7), 1259-1266.

65. Hay, P. J.; Wadt, W. R., Ab initio effective core potentials for molecular calculations. Potentials for the transition metal atoms Sc to Hg. *J. Chem. Phys.* 1985, *82* (1), 270-283.

66. Benz, F.; Tserkezis, C.; Herrmann, L. O.; de Nijs, B.; Sanders, A.; Sigle, D. O.; Pukenas, L.; Evans, S. D.; Aizpurua, J.; Baumberg, J. J., Nanooptics of Molecular-Shunted Plasmonic Nanojunctions. *Nano Lett.* 2015, *15* (1), 669-674.

67. Park, W.-H.; Kim, Z. H., Charge Transfer Enhancement in the SERS of a Single Molecule. *Nano Lett.* 2010, *10* (10), 4040-4048.

68. Matei, D. G.; Muzik, H.; Gölzhäuser, A.; Turchanin, A., Structural Investigation of 1,1'−Biphenyl−4−thiol Self−Assembled Monolayers on Au(111) by Scanning Tunneling Microscopy and Low−Energy Electron Diffraction. *Langmuir* 2012, *28* (39), 13905−13911.

69. http://www.cc.gov/niosh/npg/npgd0239.html.

70. Moskovits, M.; DiLella, D. P., Intense quadrupole transitions in the spectra of molecules near metal surfaces. *J. Chem. Phys.* 1982, *77* (4), 1655−1660.

71. Ayars, E. J.; Hallen, H. D.; Jahncke, C. L., Electric Field Gradient Effects in Raman Spectroscopy. *Phys. Rev. Lett.* 2000, *85* (19), 4180−4183.

72. Takase, M.; Ajiki, H.; Mizumoto, Y.; Komeda, K.; Nara, M.; Nabika, H.; Yasuda, S.; Ishihara, H.; Murakoshi, K., Selection−rule breakdown in plasmon−induced electronic excitation of an isolated single−walled carbon nanotube. *Nat. Photonics* 2013, *7* (7), 550−554.

73. Chulhai, D. V.; Jensen, L., Determining Molecular Orientation With Surface−Enhanced Raman Scattering Using Inhomogenous Electric Fields. *J. Phys. Chem. C* 2013, *117* (38), 19622−19631.

74. Meng, L.; Yang, Z.; Chen, J.; Sun, M., Effect of Electric Field Gradient on Sub−nanometer Spatial Resolution of Tip−enhanced Raman Spectroscopy. *Sci. Rep.* 2015, *5* (1), 9240.

75. Lombardi, J. R.; Birke, R. L., A Unified View of Surface-Enhanced Raman Scattering. *Acc. Chem. Res.* 2009, *42* (6), 734-742.

76. Campion, A.; Kambhampati, P., Surface-enhanced Raman scattering. *Chem. Soc. Rev.* 1998, *27* (4), 241-250.

77. Sawai, B. T.; Nabika, H.; Murakoshi, K., Anti-Stokes/Stokes ratio of surface-enhanced Raman scattering spectra observed at a metal nano-gap arrayed on a solid surface. *Can. J. Anal. Sci. Spectrosc.* 2007, *52* (3), 142.

78. Maher, R. C.; Hou, J.; Cohen, L. F.; Le Ru, E. C.; Hadfield, J. M.; Harvey, J. E.; Etchegoin, P. G.; Liu, F. M.; Green, M.; Brown, R. J. C.; Milton, M. J. T., Resonance contributions to anti-Stokes/Stokes ratios under surface enhanced Raman scattering conditions. *J. Chem. Phys.* 2005, *123* (8), 084702.

79. Lombardi, A.; Demetriadou, A.; Weller, L.; Andrae, P.; Benz, F.; Chikkaraddy, R.; Aizpurua, J.; Baumberg, J. J., Anomalous Spectral Shift of Near- and Far-Field Plasmonic Resonances in Nanogaps. *ACS Photonics* 2016, *3* (3), 471-477.

80. Harris, A. L.; Rothberg, L.; Dubois, L. H.; Levinos, N. J.; Dhar, L., Molecular vibrational energy relaxation at a metal surface: Methyl thiolate on Ag(111). *Phys. Rev. Lett.* 1990, *64* (17), 2086-2089.

81. Maher, R. C.; Galloway, C. M.; Le Ru, E. C.; Cohen, L. F.; Etchegoin, P. G., Vibrational pumping in surface enhanced Raman

scattering (SERS). *Chem. Soc. Rev.* 2008, *37* (5), 965−979.

82. Yao, Z.; Zhang, R.; Dong, Z.; Aizpurua, J., Unpublished.

83. Craig, D. P.; Thirunamachandran, T., *Molecular Quantum Electrodynamics* 1984, *Dover Publications: New York*.

84. Iwasa, T.; Takenaka, M.; Taketsugu, T., Generalized theoretical method for the interaction between arbitrary nonuniform electric field and molecular vibrations: Toward near−field infrared spectroscopy and microscopy. *J. Chem. Phys.* 2016, *144* (12), 124116.

85. Huheey, J. E.; Keiter, E. A.; Keiter, R. L., *Inorganic Chemistry: Principles of Structure and Reactivity*. 1997.

86. Zuloaga, J.; Prodan, E.; Nordlander, P., Quantum Description of the Plasmon Resonances of a Nanoparticle Dimer. *Nano Lett.* 2009, *9* (2), 887−891.

87. Manjavacas, A.; García de Abajo, F. J.; Nordlander, P., Quantum Plexcitonics: Strongly Interacting Plasmons and Excitons. *Nano Lett.* 2011, *11* (6), 2318−2323.

88. El−Khoury, P. Z.; Hu, D.; Apkarian, V. A.; Hess, W. P., Raman Scattering at Plasmonic Junctions Shorted by Conductive Molecular Bridges. *Nano Lett.* 2013, *13* (4), 1858−1861.

89. Banik, M.; Apkarian, V. A.; Park, T. H.; Galperin, M., Raman Staircase in Charge Transfer SERS at the Junction of Fusing

Nanospheres. *J. Phys. Chem. Lett.* 2013, *4* (1), 88−92.

90. El−Khoury, P. Z.; Hess, W. P., Vibronic Raman Scattering at the Quantum Limit of Plasmons. *Nano Lett.* 2014, *14* (7), 4114−4118.

91. Chen, X.; Moore, J. E.; Zekarias, M.; Jensen, L., Atomistic electrodynamics simulations of bare and ligand−coated nanoparticles in the quantum size regime. *Nat. Commun.* 2015, *6* (1), 8921.

92. Hyunyoung, Y. K.; Daisik, S. K., Selection rule engineering of forbidden transitions of a hydrogen atom near a nanogap. *Nanophotonics* 2018, *7* (1), 229−236.

93. Beckerle, J. D.; Casassa, M. P.; Cavanagh, R. R.; Heilweil, E. J.; Stephenson, J. C., Ultrafast infrared response of adsorbates on metal surfaces: Vibrational lifetime of CO/Pt(111). *Phys. Rev. Lett.* 1990, *64* (17), 2090−2093.

94. Beckerle, J. D.; Cavanagh, R. R.; Casassa, M. P.; Heilweil, E. J.; Stephenson, J. C., Subpicosecond transient infrared spectroscopy of adsorbates. Vibrational dynamics of CO/Pt(111). *J. Chem. Phys.* 1991, *95* (7), 5403−5418.

95. Morin, M.; Levinos, N. J.; Harris, A. L., Vibrational energy transfer of CO/Cu(100): Nonadiabatic vibration/electron coupling. *J. Chem. Phys.* 1992, *96* (5), 3950−3956.

96. Shirhatti, P. R.; Rahinov, I.; Golibrzuch, K.; Werdecker, J. r.; Geweke, J.; Altsch¡¤ffel, J.; Kumar, S.; Auerbach, D. J.; Bartels, C.;

Wodtke, A. M., Observation of the adsorption and desorption of vibrationally excited molecules on a metal surface. *Nat. Chem.* 2018, *10* (6), 592−598.

97. Gadzuk, J. W., Vibrational excitation in molecule−surface collisions due to temporary negative molecular ion formation. *J. Chem. Phys.* 1983, *79* (12), 6341−6348.

98. Christopher, P.; Xin, H.; Linic, S., Visible−light−enhanced catalytic oxidation reactions on plasmonic silver nanostructures. *Nat. Chem.* 2011, *3* (6), 467−472.

99. Christopher, P.; Xin, H.; Marimuthu, A.; Linic, S., Singular characteristics and unique chemical bond activation mechanisms of photocatalytic reactions on plasmonic nanostructures. *Nat. Mater.* 2012, *11* (12), 1044−1050.

100. Crampton, K. T.; Fast, A.; Potma, E. O.; Apkarian, V. A., Junction Plasmon Driven Population Inversion of Molecular Vibrations: A Picosecond Surface−Enhanced Raman Spectroscopy Study. *Nano Lett.* 2018, *18* (9), 5791−5796.

101. dos Santos, D. P.; Temperini, M. L. A.; Brolo, A. G., Mapping the Energy Distribution of SERRS Hot Spots from Anti−Stokes to Stokes Intensity Ratios. *J. Am. Chem. Soc.* 2012, *134* (32), 13492−13500.

102. Choi, H.−K.; Lee, K. S.; Shin, H.−H.; Kim, Z. H., Identification

of the First Elementary Step in the Photocatalytic Reduction of Nitrobenzenethiols on a Metallic Surface. *J. Phys. Chem. Lett.* 2016, *7* (20), 4099−4104.

103. Carnegie, C.; Griffiths, J.; de Nijs, B.; Readman, C.; Chikkaraddy, R.; Deacon, W. M.; Zhang, Y.; Szabó, I.; Rosta, E.; Aizpurua, J.; Baumberg, J. J., Room−Temperature Optical Picocavities below 1 nm^3 Accessing Single−Atom Geometries. *J. Phys. Chem. Lett.* 2018, *9* (24), 7146−7151.

104. Shin, H.−H.; Yeon, G. J.; Choi, H.−K.; Park, S.−M.; Lee, K. S.; Kim, Z. H., Frequency−Domain Proof of the Existence of Atomic−Scale SERS Hot−Spots. *Nano Lett.* 2018, *18* (1), 262−271.

105. Palmer, R. E.; Rous, P. J., Resonances in electron scattering by molecules on surfaces. *Rev. Mod. Phys.* 1992, *64* (2), 383−440.

106. Álvarez, L.; Costa, F.; Lozano, A. I.; Oller, J. C.; Muñoz, A.; Blanco, F.; Limão−Vieira, P.; White, R. D.; Brunger, M. J.; García, G., Electron scattering cross sections from nitrobenzene in the energy range 0.4–1000 eV: the role of dipole interactions in measurements and calculations. *Phys. Chem. Chem. Phys.* 2020, *22* (24), 13505−13515.

107. Maioli, L. S.; Bettega, M. H. F., Elastic electron scattering from nitrobenzene. *J. Chem. Phys.* 2017, *147* (16), 164305.

108. Gadzuk, J. W., Inelastic resonance scattering, tunneling, and

desorption. *Phys. Rev. B* 1991, *44* (24), 13466-13477.

109. Gadzuk, J. W., Resonance-Assisted Hot Electron Femtochemistry at Surfaces. *Phys. Rev. Lett.* 1996, *76* (22), 4234-4237.

110. Domcke, W.; Cederbaum, L. S., Vibration-induced narrowing of electron scattering resonances near threshold. *J. Phys. B* 1980, *13* (14), 2829-2838.

111. Mewes, J.-M.; Jovanović, V.; Marian, C. M.; Dreuw, A., On the molecular mechanism of non-radiative decay of nitrobenzene and the unforeseen challenges this simple molecule holds for electronic structure theory. *Phys. Chem. Chem. Phys.* 2014, *16* (24), 12393-12406.

112. Braun, S.; Salaneck, W. R.; Fahlman, M., Energy-Level Alignment at Organic/Metal and Organic/Organic Interfaces. *Adv. Mater.* 2009, *21* (14-15), 1450-1472.

113. Shin, H.-H.; Koo, J.-J.; Lee, K. S.; Kim, Z. H., Chemical reactions driven by plasmon-induced hot carriers. *Appl. Mater. Today* 2019, *16*, 112-119.

114. Sykes, M. E.; Stewart, J. W.; Akselrod, G. M.; Kong, X.-T.; Wang, Z.; Gosztola, D. J.; Martinson, A. B. F.; Rosenmann, D.; Mikkelsen, M. H.; Govorov, A. O.; Wiederrecht, G. P., Enhanced generation and anisotropic Coulomb scattering of hot electrons in an

ultra-broadband plasmonic nanopatch metasurface. *Nat. Commun.* 2017, *8* (1), 986.

115. Cortés, E.; Xie, W.; Cambiasso, J.; Jermyn, A. S.; Sundararaman, R.; Narang, P.; Schlücker, S.; Maier, S. A., Plasmonic hot electron transport drives nano-localized chemistry. *Nat. Commun.* 2017, *8* (1), 14880.

116. Reed, M. A.; Zhou, C.; Muller, C. J.; Burgin, T. P.; Tour, J. M., Conductance of a Molecular Junction. *Science* 1997, *278* (5336), 252.

117. Tian, J.-H.; Liu, B.; Li; Yang, Z.-L.; Ren, B.; Wu, S.-T.; Tao; Tian, Z.-Q., Study of Molecular Junctions with a Combined Surface-Enhanced Raman and Mechanically Controllable Break Junction Method. *J. Am. Chem. Soc.* 2006, *128* (46), 14748-14749.

118. Zhang, W.; Yeo, B. S.; Schmid, T.; Zenobi, R., Single Molecule Tip-Enhanced Raman Spectroscopy with Silver Tips. *J. Phys. Chem. C* 2007, *111* (4), 1733-1738.

119. Xu, B.; Tao, N. J., Measurement of Single-Molecule Resistance by Repeated Formation of Molecular Junctions. *Science* 2003, *301* (5637), 1221.

120. Chikkaraddy, R.; de Nijs, B.; Benz, F.; Barrow, S. J.; Scherman, O. A.; Rosta, E.; Demetriadou, A.; Fox, P.; Hess, O.; Baumberg, J. J., Single-molecule strong coupling at room temperature in plasmonic nanocavities. *Nature* 2016, *535* (7610), 127-130.

121. Li, J. F.; Huang, Y. F.; Ding, Y.; Yang, Z. L.; Li, S. B.; Zhou, X. S.; Fan, F. R.; Zhang, W.; Zhou, Z. Y.; Wu, D. Y.; Ren, B.; Wang, Z. L.; Tian, Z. Q., Shell-isolated nanoparticle-enhanced Raman spectroscopy. *Nature* 2010, *464* (7287), 392-395.

국문초록

표면증강라만법 (SERS)을 사용하여 매우 효과적인 표면흡착분자의 진동모드펌핑이 연구되었다. 입사되는 빛은 나노구조체에 존재하는 전자들의 집단 진동인 국소플라스몬 (LSP)을 발생시키며, LSP는 금속주변에 전자기장을 증폭시킨다. 금속들 사이 간극에서 극대화되는 LSP는 SERS를 발생시킬 뿐 아니라 근처 분자의 진동모드 또한 펌핑시킨다. 본 학위논문은 두 개의 진동모드 펌핑 메커니즘에 집중한다. 첫 번째는 picocavity라 불리는 금속표면의 잔 구조체 근처에 생성되는 강력한 전자기장에 의한 것이고, 두 번째는 LSP에 의해서 발생되는 높은 에너지의 전자의 비탄성 공명 산란에 의한 것이다. 이 효율적인 펌핑 메커니즘들은 금속표면에서 발생하는 빠른 진동에너지 이완 (VR)를 극복하여 상당수의 분자들을 진동 여기 된 정상상태로 만든다.

Picocavity는 그 생성되는 기원이 무엇인지 불분명하지만, 간극플라스몬이 금속표면에 존재하는 단원자 돌출부와 같은 미세 구조체를 간헐적으로 자극하여 발생하는 것으로 의심된다. Picocavity 근처에서 아주 좁게 국지화 되어있는 전자기장은 (1) 매우 강력한 장 감쇄 (field-gradient)를 유발하여 이에 따른 인접한 분자의 라만 선택성 변형과 (2) 추가적인 SERS의 증폭을 야기시킨다. 추가적인 SERS 증폭은 변형된 라만선택성을 만족시키는 진동모드를 펌핑시키며, 이에 따라 Stokes와 anti-Stokes 양쪽에서 강한 피크가 동시에 발생하게 된다. 본 학위논문에서는 picocavity의 존재여부를 스펙트럼의 개형을 분석함으로써 증명

한다. 은 나노입자 (지름 : 80 nm), 금 박막 (두께 : 10 nm) 사이에 끼인 4,4'-biphenyldithiol (BPDT)의 SERS를 anti-Stokes, Stoke 양쪽에서 동시에 측정되었다. 여러 스펙트럼에서 picocavity의 특징들이 발견되었으며 더 나아가 이전 보고와는 다르게 단 하나의 피크만이 Stokes, anti-Stokes 양쪽에서 발생되었다. picocavity 모델링을 통해 BPDT의 각 진동모드들의 라만 반응성 (Raman-activity)이 다시 부여되었고, 실험으로 얻은 스펙트럼들이 재현되었다. 이 모델은 전자기장이 picocavity의 중심으로부터 방사형으로 퍼지며 가우스 함수의 형태로 감쇄되도록 설정되었다. 모델계산을 통해, 특정한 스펙트럼을 나타내는 고유한 picocavity의 위치가 결정 되었으며 실험을 통해 얻은 많은 스펙트럼들이 성공적으로 재현되었다. 또한 계산들은 통해, 단일 피크 스펙트럼을 재현하기 위한 picocavity 크기의 하한선은 3.5 Å이며 여러 피크를 보이는 스펙트럼들은 picocavity의 크기가 1 nm가 되어도 재현 가능하였다. 이러한 결과들은 picocavity가 존재할 가능성을 강력하게 뒷받침한다. 더욱이 많은 단일 피크 스펙트럼들은 선택적인 진동모드 여기를 통해 표면화학반응을 조절할 수 있다는 가능성을 강력하게 뒷받침 한다. 하지만 아직까지 이합체, 나노입자/박막 구조체와 같은 고전적인 플라스몬 간극 구조체에서는 이러한 picocavity의 생성여부와 위치를 인위적으로 조절할 수 없다

공명라만산란과 비슷하게, 분자에 비어있는 오비탈에 접근할 수 있는 에너지를 갖는 전자 또한 비탄성 공명산란을 통해 분자로 에너지를 전달할 수 있다. 전달된 에너지는 프랭크-콘돈 인자 (Franck-Condon

factor)가 큰 특정한 진동모드에 축적된다. 본 학위논문에서는 금속표면에서 발생되는 전자를 매개로 한 진동모드 펌핑이 제시된다. 은 나노입자 / 금박막 사이에 끼인 4-nitrobenzenethiol (NBT)분자의 Stokes와 anti-Stokes SERS가 동시에 측정되었다. NBT는 간극 내에서 빛 조사에 의해 광환원반응을 일으키는데, 이 반응의 초기에 다른 진동모드들과는 다르게 NO_2 그룹에 국지화된 ν_S(NO)의 강한 anti-Stokes가 유발되는 것이 관찰되었다. 또한 picocavity의 경우와 마찬가지로 ν_S(NO)의 anti-Stokes는 이차의 광량 의존성 (quadratic power-dependence)을 보였다. 이러한 이차의 광량 의존성은 진동 여기된 ν_S(NO)가 비열적으로 펌핑 되었음을 의미한다. 하지만 picocavity와는 다르게, ν_S(NO)의 펌핑은 (1) 무작위로 깜빡이는 특징을 보이지 않으며, (2) 라만 선택성의 변화를 보이지 않는다. 또한 무엇보다도 (3) 상당한 진동모드 선택성과 재현성을 보인다. 이러한 펌핑을 설명하기 위해서, 프랭크-콘돈 적분에 의존하는 전자의 비탄성 공명산란을 모델링이 적용되었으며 이를 통해 ν_S(NO) 선택성을 재현되었다. ν_S(NO)의 펌핑이 플라스몬과 연관된 현상임을 보이기 위해, ν_S(NO) anti-Stokes의 파장 의존성이 측정해 되었다. Anti-Stokes는 473, 532, 633, 808 나노미터의 레이져로 측정되었으며, 암시야 스펙트럼과 비교되었을 상당한 유사성을 보였다. 추가적으로 NBT의 광환원을 통해 생성된 dimercaptoazobenzene의 anti-Stokes가 강하게 유발되는 것이 관찰되었다. Anti-Stokes에서 관찰되는 피크들은 전자산란모델로 재현되는 것들과 일치하였다. 한편 NBT와 비슷한 구조를 갖는 4-mercaptobenzonitrile과 같은 분자는 anti-

Stokes에 어떠한 피크도 강하게 유발되지 않았으며, 전자 산란모델도 특정한 진동모드의 펌핑 효율을 나타내지 않았다. 이 데이터들은 LSP에 의해서 여기 된 전자가 특정 분자, 진동모드로 에너지를 전달한다는 것을 강하게 뒷받침한다.